Separation and Purification Technology 227 (2019) 115730

Contents lists available at ScienceDirect

Separation and Purification Technology

journal homepage: www.elsevier.com/locate/seppur

Highlighting non-idealities in C_2H_4/CO_2 mixture adsorption in 5A zeolite

Ilona van Zandvoort[a], Jan Kees van der Waal[a], Erik-Jan Ras[a], Robbert de Graaf[a], Rajamani Krishna[b,*]

[a] Avantium Chemicals B.V., Zekeringstraat 29, 1014 BV Amsterdam, the Netherlands
[b] Van't Hoff Institute for Molecular Sciences, University of Amsterdam, Science Park 904, 1098 XH Amsterdam, the Netherlands

ARTICLE INFO

Keywords:
Selectivity reversal
Non-ideal mixture adsorption
Biomass gasification
Ethylene recovery
Transient breakthrough

ABSTRACT

Gasification of biomass at relatively low temperatures (770–880 °C) yields producer gas mixtures containing H_2, CO and CO_2, along with CH_4, C_2H_6, and C_2H_4. It is of economic importance to recover C_2H_4 by selective adsorption using cation-exchanged zeolites such as LTA-5A. However, calculations of mixture adsorption equilibrium for LTA-5A using the Ideal Adsorbed Solution Theory (IAST) predict that the mixture adsorption equilibrium is selective to CO_2, and recovery of C_2H_4 is not feasible. In sharp contrast to IAST predictions, transient breakthrough experiments with $H_2/CH_4/C_2H_6/CO/CO_2/C_2H_4$ feed mixtures of different compositions show that selective recovery of C_2H_4 from the producer gas is feasible provided the C_2H_4/CO_2 molar ratio in the feed mixture is below unity; for C_2H_4/CO_2 molar ratios exceeding unity, the selectivity is in favor of CO_2. The selectivity reversal phenomena signifies strong non-idealities in mixture adsorption. Such non-idealities can be quantified using the Real Adsorbed Solution Theory (RAST). This article underscores the need for performing transient breakthrough experiments with realistic producer gas mixtures for process modelling and development purposes.

1. Introduction

Biomass derived fuels are often considered as replacement for fossil fuel to contribute to the energy transition to renewable energy sources. Syngas is a product from biomass gasification, containing H_2, CO and CO_2, which can be further used for the production of synthetic natural gas (SNG or bio-methane). Medium temperature gasification is performed at relatively low temperatures (770–880 °C) and the resulting producer gas contains significant amounts of alkanes, alkenes and aromatics. These products are valuable base chemicals and can be produced in significant amounts; for example, up to 16% C_2H_4 can be present based on energy content [1]. Recovery of C_2H_4 by selective adsorption can contribute significantly to the economic viability of biomass to SNG via medium temperature gasification.

LTA-5A zeolite is a potent and commonly used adsorbent for selective adsorption of C_2H_4 from gaseous mixtures containing one or more of the following constituents: H_2, N_2, CO, CH_4, and C_2H_6 [2–10]. The selectivity in favor of C_2H_4 is caused by electrostatic interactions between the π-orbitals of C_2H_4 with the extra-framework cations (Na^+, and Ca^{++}) of LTA-5A. LTA-5A zeolite is also used in pressure swing adsorption (PSA) technologies for H_2 purification from gaseous mixtures containing N_2, Ar, CH_4, CO, and CO_2 [4–8,11–16]; the selectivity towards CO_2, which has a quadrupole moment, is also attributable to electrostatic interactions with the extra-framework cations. The adsorptive separation of effluent gases from oxidative coupling of methane also involves the selective recovery of C_2H_4 from $N_2/CH_4/C_2H_6/CO_2/C_2H_4$ mixtures using LTA-5A zeolite [17]. For recovery of C_2H_4 from gaseous mixtures that are typical of effluent gas streams from biomass gasification (typically containing CH_4, C_2H_6, CO, CO_2, C_2H_4, lower alkanes, and alkenes), the efficacy of LTA-5A as adsorbent is crucially dependent on the C_2H_4/CO_2 adsorption selectivity.

In the design and development of PSA technologies, the Ideal Adsorbed Solution Theory (IAST) of Myers and Prausnitz [18] is commonly used for estimation of mixture adsorption equilibrium. Briefly, the basic equation of IAST is the analogue of Raoult's law for vapor-liquid equilibrium, i.e.

$$p_i = P_i^0 x_i; \quad i = 1, 2, \ldots n \tag{1}$$

where x_i is the mole fraction in the adsorbed phase

$$x_i = \frac{q_i}{q_1 + q_2 + \ldots q_n} \tag{2}$$

and P_i^0 is the pressure for sorption of every component i, which yields the same spreading pressure, π for each of the pure components, as that

* Corresponding author.
E-mail address: r.krishna@contact.uva.nl (R. Krishna).

https://doi.org/10.1016/j.seppur.2019.115730
Received 20 May 2019; Received in revised form 20 June 2019; Accepted 23 June 2019
Available online 24 June 2019

Nomenclature

Latin alphabet

A	surface area per kg of framework, $m^2\ kg^{-1}$
C	constant used in Eq. (8), kg mol^{-1}
f	gas phase fugacity, Pa
n	number of species in the mixture, dimensionless
p_i	partial pressure of species i, Pa
p_t	total system pressure, Pa
P_i^0	sorption pressure, Pa
q_A	molar loading species A, mol kg^{-1}
$q_{i,sat}$	molar loading of species i at saturation, mol kg^{-1}
q_t	total molar loading of mixture, mol kg^{-1}
R	gas constant, 8.314 J mol^{-1} K^{-1}
S_{ads}	adsorption selectivity, dimensionless
T	absolute temperature, K
x_i	mole fraction of species i in adsorbed phase, dimensionless
y_i	mole fraction of species i in bulk fluid mixture, dimensionless

Greek letters

γ_i	activity coefficient of component i in adsorbed phase, dimensionless
Λ_{ij}	Wilson parameters, dimensionless
π	spreading pressure, N m^{-1}
ρ	framework density, kg m^{-3}

Subscripts

i,j	components in mixture
t	referring to total mixture

Superscripts

0	referring to pure component loading
excess	referring to excess parameter

for the mixture:

$$\frac{\pi A}{RT} = \int_0^{P_1^0} \frac{q_1^0(f)}{f} df = \int_0^{P_2^0} \frac{q_2^0(f)}{f} df = \int_0^{P_3^0} \frac{q_3^0(f)}{f} df = \ldots \quad (3)$$

where $q_i^0(f)$ is the *pure* component adsorption isotherm, and f is the gas phase fugacity. The units of $\frac{\pi A}{RT}$ are mol kg^{-1} and is referred to as the adsorption potential [19]. The adsorption potential can be determined by analytic integration of the unary isotherm data fits for each component.

A key assumption of the IAST is that the enthalpies and surface areas of the adsorbed molecules do not change upon mixing. If the total mixture loading is q_t, the surface area per mole of adsorbed mixture is $\frac{A}{q_t}$. Therefore, the assumption of no surface area change due to mixture adsorption translates as $\frac{A}{q_t} = \frac{Ax_1}{q_1^0(P_1^0)} + \frac{Ax_2}{q_2^0(P_2^0)} + \cdots \frac{Ax_n}{q_n^0(P_n^0)}$ in which $q_1^0(P_1^0)$, $q_2^0(P_2^0)$,... $q_n^0(P_n^0)$ are determined from the unary isotherm fits, using the sorption pressures for each component P_1^0, P_2^0, P_3^0,... The total mixture loading is q_t is calculated from

$$q_t = q_1 + q_2 \ldots + q_n = \frac{1}{\frac{x_1}{q_1^0(P_1^0)} + \frac{x_2}{q_2^0(P_2^0)} + \ldots + \frac{x_n}{q_n^0(P_n^0)}} \quad (4)$$

The entire set of Eqs. (1)–(4) need to be solved numerically to obtain the molar loadings, q_i of the individual components in the mixture.

The use of the IAST allows calculation of the adsorption selectivities, S_{ads}, defined by

$$S_{ads} = \frac{q_1/q_2}{y_1/y_2} \quad (5)$$

where q_1 and q_2 are the molar loadings of the components 1, and 2 in the adsorbed phase in equilibrium with a bulk gas phase mixture with mole fractions y_1 and y_2. For a binary $C_2H_4(1)/CO_2(2)$ mixture, the IAST calculations of the adsorption selectivity for a range of bulk phase mole fractions y_1 are presented in Fig. 1 for three different pressures p_t = 1, 6 and 11 bar and temperature T = 313 K; the unary isotherm data for C_2H_4, and CO_2 are taken from Mofarahi and Salehi [2], and Mofarahi and Gholipour [20]. At all three pressures, $S_{ads} < 1$, i.e. the adsorption selectivity is in favor of CO_2. The selectivity S_{ads} decreases further at a lower temperature, T = 293 K. From the IAST calculations in Fig. 1 we would conclude that selective adsorption of C_2H_4 from CO_2-bearing gas mixtures is not possible.

The primary objective of this communication is to demonstrate that the conclusions drawn from the IAST calculations, shown in Fig. 1 for C_2H_4/CO_2 mixture adsorption, may be misleading due to strong thermodynamic non-idealities. In order to demonstrate the shortcomings of IAST calculations, transient breakthrough experiments were performed for $N_2/Ar/H_2/CH_4/C_2H_6/CO/CO_2/C_2H_4$ feed mixtures of different compositions, with Ar as internal standard N_2 as balance gas, in tubes packed with LTA-5A zeolite, operating at 313 K and three different pressures p_t = 1, 6 and 11 bar. A total of 28 different campaigns of transient breakthrough experiments were performed in a Flowrence set-up, described in earlier work [10]; the experimental details are summarized in the Supplementary Material accompanying this publication.

2. Transient breakthrough experiments

Fig. 2 presents a representative set of transient breakthrough experiments for feed mixtures $N_2/Ar/H_2/CH_4/C_2H_6/CO/CO_2/C_2H_4$ of

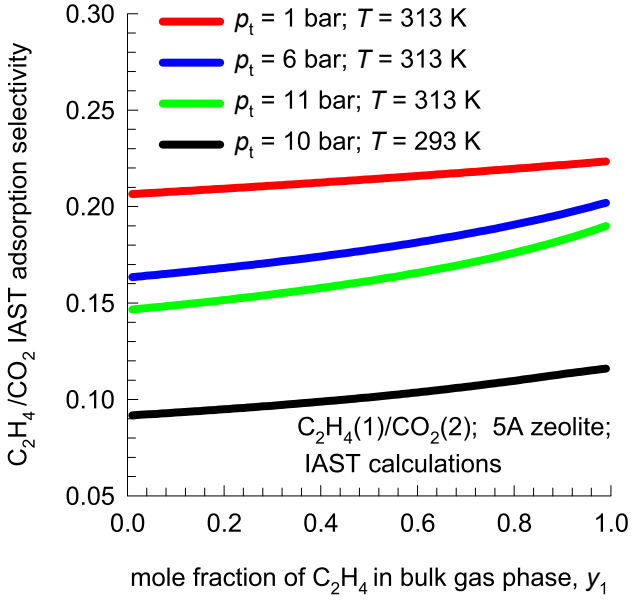

Fig. 1. IAST calculations for the adsorption selectivity for binary $C_2H_4(1)/CO_2(2)$ mixtures as a function of the bulk phase mole fraction of C_2H_4, y_1. The calculations are presented for three different pressures p_t = 1, 6 and 11 bar and temperature T = 313 K, and for p_t = 6 bar, T = 293 K. The unary isotherm data for C_2H_4, and CO_2 are from Mofarahi and Salehi [2], and Mofarahi and Gholipour [20]. See Supplementary Material for information on the unary isotherm fit parameters and details of IAST calculations.

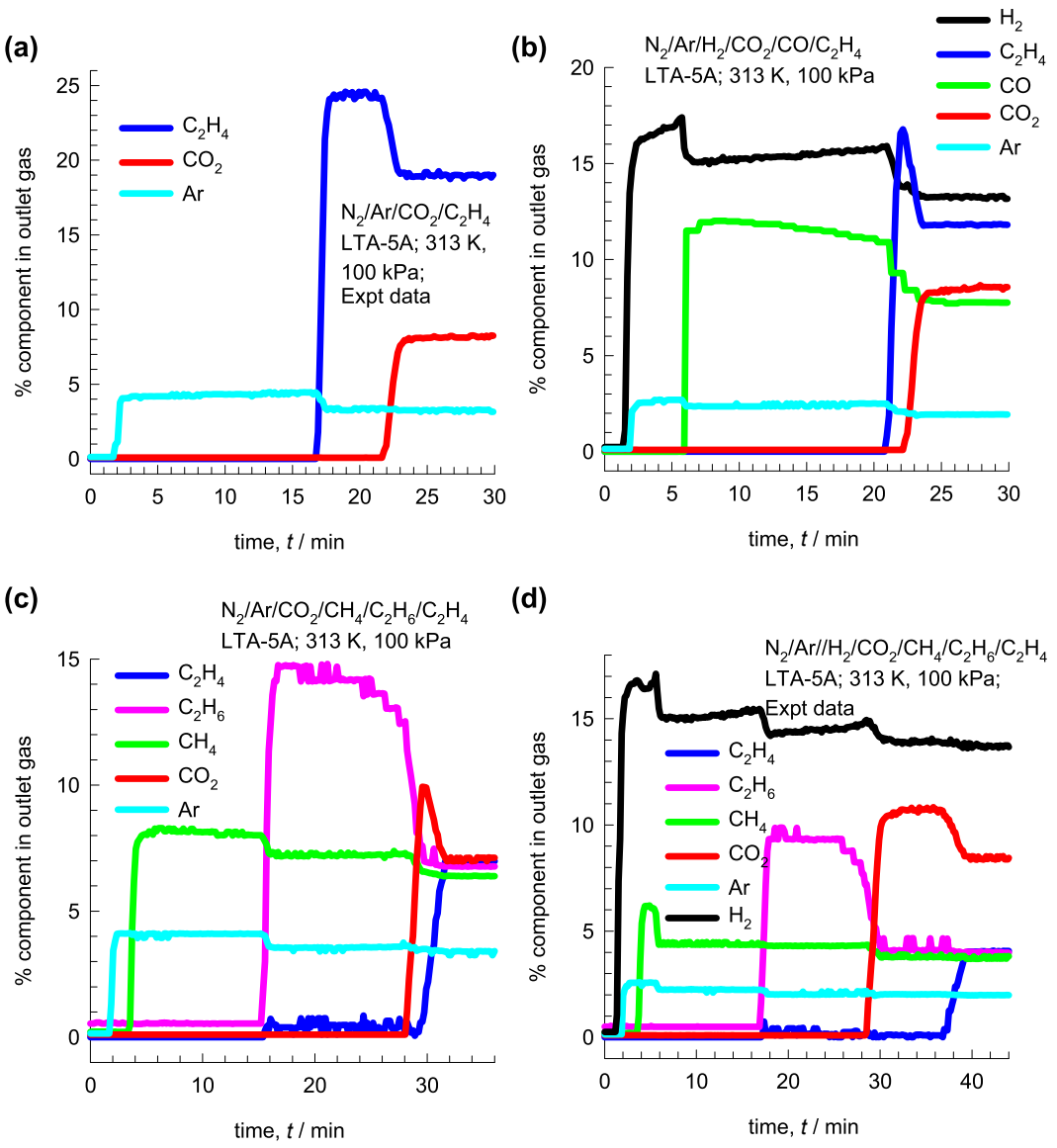

Fig. 2. Transient breakthrough experiments for feed mixtures of four different compositions: (a) 69.59/3.15/8.25/19.01 $N_2/Ar/CO_2/C_2H_4$, (b) 56.78/1.93/13.17/7.75/8.56/11.81 $N_2/Ar/H_2/CH_4/C_2H_6/CO/CO_2/C_2H_4$, (c) 69.28/3.39/6.37/6.76/7.24/6.97 $N_2/Ar/CH_4/C_2H_6/CO_2/C_2H_4$, and 63.91/1.98/13.74/3.82/3.98/8.51/4.06 $N_2/Ar/H_2/CH_4/C_2H_6/CO_2/C_2H_4$. The total pressure in all four experiments is 1 bar, and temperature T = 313 K; these correspond to Runs 7, 8, 9 and 10 of the total of 28 experimental campaigns. The % N_2 in the outlet gas in the four experiments can be determined by the taking the sum of the mole % = 100. Further experimental details are provided in the Supplementary Material.

four different compositions in a fixed bed tube packed with LTA-5A zeolite operating at a total pressure p_t = 1 bar, and T = 313 K. The C_2H_4/CO_2 mole ratio in the four feed mixtures are (a) 2.3, (b) 1.38, (c) 0.96, and (d) 0.48. For the two experiments (a, b) with C_2H_4/CO_2 mole ratios exceeding unity, the breakthrough times for CO_2 exceed that of C_2H_4; i.e. mixture adsorption is selective to CO_2. In both these cases, selective adsorption of C_2H_4 is not possible. However, for the experiments (c, d) with C_2H_4/CO_2 mole ratios lower than unity, the breakthrough times for C_2H_4 exceed that of CO_2; i.e. mixture adsorption is selective to C_2H_4. In both these cases, selective adsorption of C_2H_4 is feasible. The experiments in Fig. 2(c,d) indicate the failure of the IAST, that anticipates the selectivity to favor CO_2, irrespective of the feed composition (see Fig. 1).

To underscore the failure of the IAST to predict mixture adsorption, transient breakthrough simulations for the set of four experiments were carried out using the methodology described in detail in earlier works [6–8,21] ; details are provided in the Supplementary Material. The transient breakthrough simulations are shown in Fig. 3(a,b,c,d); these simulations use the IAST for calculation of mixture adsorption equilibrium. For all four feed mixtures, CO_2 is the last component to break through, i.e. the mixture adsorption is in favor of CO_2 irrespective of the feed composition, in line with the IAST calculations presented in Fig. 1.

The results presented in Fig. 2 (breakthrough experiments), and Fig. 3 (corresponding breakthrough simulations using IAST for calculation of mixture adsorption equilibrrium) are representative of each of the 28 experimental campaigns carried out with varying feed mixture compositions at three different total pressures p_t = 1, 6 and 11 bar; see Figs. S5–S32 of Supplementary Material.

3. Modelling non-idealities in C_2H_4/CO_2 mixture adsorption

The selectivity reversal phenomena witnessed in Fig. 2 are indicative of strong deviations from the IAST model. Strong non-idealities for adsorption of $C_2H_4(1)/CO_2(2)$ mixtures in LTA-5A zeolite were first underscored by Calleja et al.[22] Their experimental data, obtained at 293 K and total pressure of 10 bar have been redrawn for further

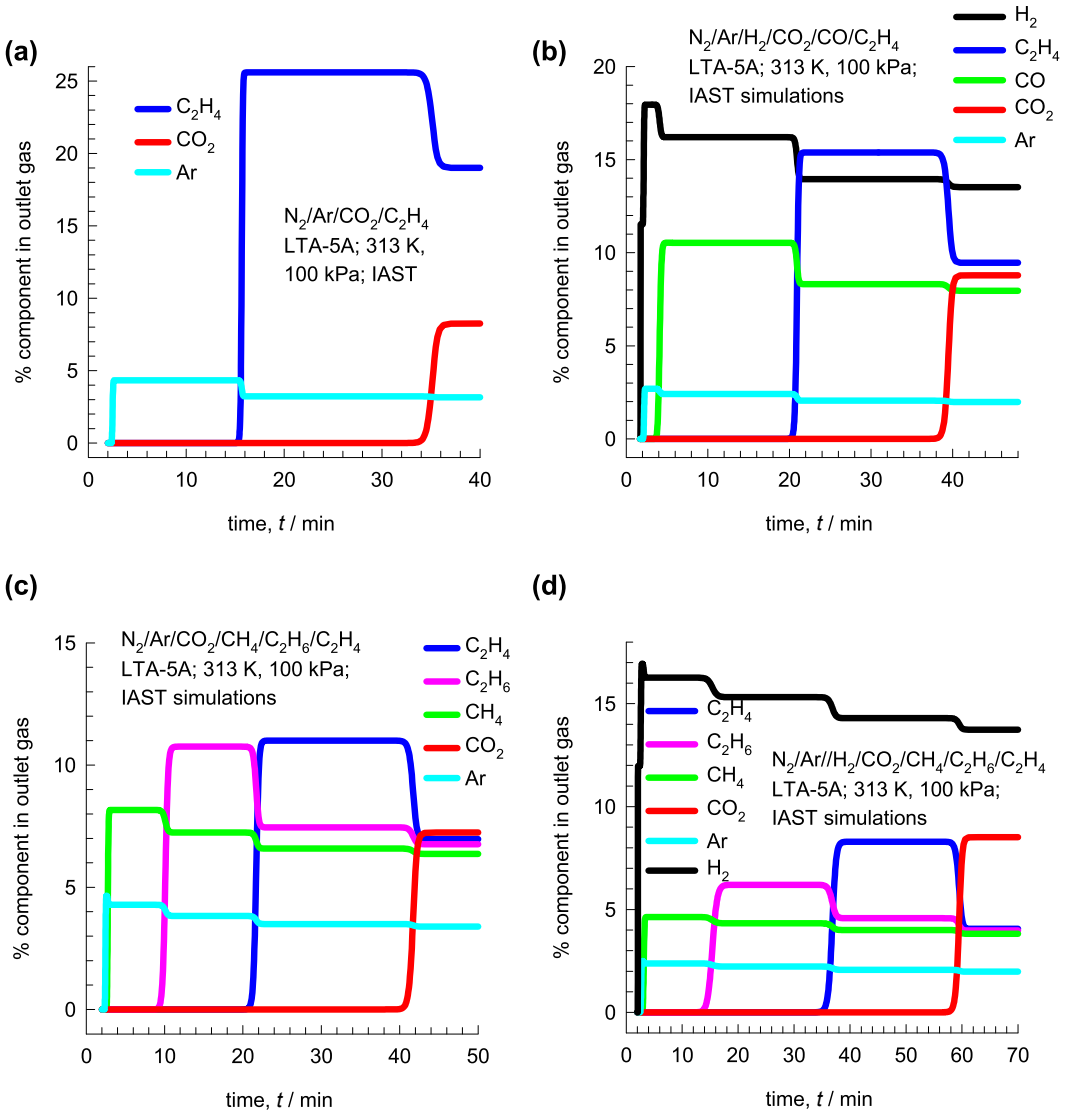

Fig. 3. Transient breakthrough simulations for the four sets of experimental data shown in Fig. 2. The methodology for transient breakthrough simulations, based on IAST estimations of mixture adsorption equilibrium, are provided in the Supplementary Material; see Figs. S34–S44.

analysis and discussion in Fig. 4(a). The Calleja et al.[22] data clearly demonstrate the phenomenon of azeotropic adsorption, $y_1 = x_1$; $y_2 = x_2$, and selectivity reversals.

To account for non-ideality effects in mixture adsorption, we introduce activity coefficients γ_i into Eq. (1) [18]

$$p_i = P_i^0 x_i \gamma_i \tag{6}$$

The implementation of the activity coefficients is termed as the Real Adsorbed Solution Theory (RAST). Following the approaches of Myers, Talu, and Sieperstein [19,23,24] the excess Gibbs free energy for binary mixture adsorption is modeled as follows

$$\frac{G^{excess}}{RT} = x_1 \ln(\gamma_1) + x_2 \ln(\gamma_2) \tag{7}$$

The Wilson model for activity coefficients are given for binary mixtures by

$$\begin{aligned}\ln(\gamma_1) &= \left(1 - \ln(x_1\Lambda_{11} + x_2\Lambda_{12}) - \frac{x_1\Lambda_{11}}{x_1\Lambda_{11}+x_2\Lambda_{12}} - \frac{x_2\Lambda_{21}}{x_2+x_1\Lambda_{21}}\right)\left(1 - \exp\left(-C\frac{\pi A}{RT}\right)\right)\\ \ln(\gamma_2) &= \left(1 - \ln(x_1\Lambda_{21} + x_2\Lambda_{22}) - \frac{x_1\Lambda_{12}}{x_1\Lambda_{11}+x_2\Lambda_{12}} - \frac{x_2\Lambda_{22}}{x_1\Lambda_{21}+x_2\Lambda_{22}}\right)\left(1 - \exp\left(-C\frac{\pi A}{RT}\right)\right)\end{aligned} \tag{8}$$

In Eq. (8), $\Lambda_{11} \equiv 1$; $\Lambda_{22} \equiv 1$, and C is a constant with the units kg mol^{-1}. The introduction of $\left(1 - \exp\left(-C\frac{\pi A}{RT}\right)\right)$ imparts the correct limiting behaviors $\gamma_i \to 1$; $\frac{\pi A}{RT} \to 0$ for the activity coefficients in the Henry regime, $p_t \to 0$; $\frac{\pi A}{RT} \to 0$. As pore saturation conditions are approached, this correction factor tends to unity $\left(1 - \exp\left(-C\frac{\pi A}{RT}\right)\right) \to 1$. The choice of $\Lambda_{12} = \Lambda_{21} = 1$ in Eq. (8), yields unity values for the activity coefficients reduces to the IAST.

The excess reciprocal loading for the mixture can be defined as

$$\left(\frac{1}{q_t}\right)^{excess} = \frac{1}{q_t} - \left(\frac{x_1}{q_1^0(P_1^0)} + \frac{x_2}{q_2^0(P_2^0)}\right) \tag{9}$$

The excess reciprocal loading for the mixture can be related to the partial derivative of the Gibbs free energy with respect to the

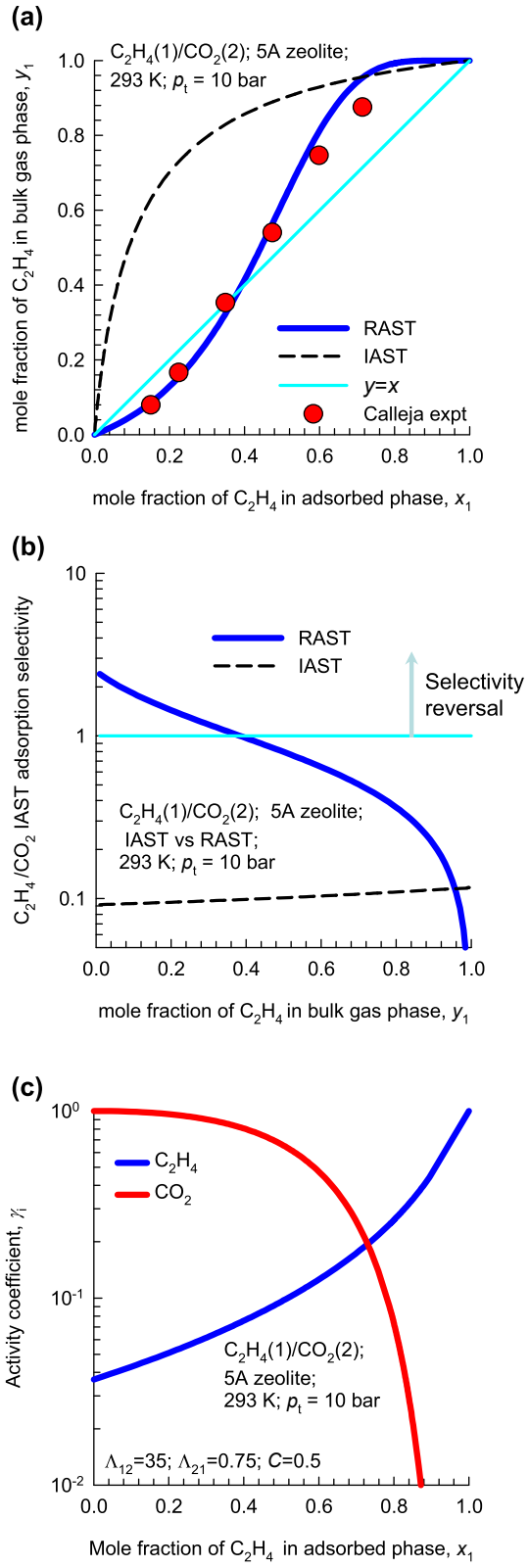

Fig. 4. (a) Experimental data, obtained at 293 K and total pressure, p_t = 10 bar, for adsorption of $C_2H_4(1)/CO_2(2)$ mixtures in LTA-5A zeolite; the mole fraction of C_2H_4 in the bulk gas phase mixture is plotted as a function of the adsorbed phase mole fraction of C_2H_4. The data are redrawn from Fig. 3 of Calleja et al. [22] Also indicated at the IAST and RAST calculations of mixture adsorption equilibrium. (b) Comparison of the IAST and RAST calculations for adsorption selectivity at 293 K, and p_t = 10 bar. (c) Activity coefficients of C_2H_4, and CO_2 as a function of the adsorbed phase mole fraction of C_2H_4.

adsorption potential at constant composition

$$\left(\frac{1}{q_t}\right)^{excess} = \frac{\partial\left(\frac{G^{excess}}{RT}\right)}{\partial\left(\frac{\pi A}{RT}\right)}\Bigg|_{T,x} = [-x_1\ln(x_1 + x_2\Lambda_{12}) - x_2\ln(x_2 + x_1\Lambda_{21})]C\exp\left(-C\frac{\pi A}{RT}\right) \tag{10}$$

For calculation of the total mixture loading we need to replace Eq. (4) by

$$q_t \equiv q_1 + q_2 = \frac{1}{\frac{x_1}{q_1^0(P_1^0)} + \frac{x_2}{q_2^0(P_2^0)} + [-x_1\ln(x_1 + x_2\Lambda_{12}) - x_2\ln(x_2 + x_1\Lambda_{21})]C\exp\left(-C\frac{\pi A}{RT}\right)} \tag{11}$$

The Calleja et al. [22] data are well represented by the choice of the Wilson parameters $\Lambda_{12} = 35$; $\Lambda_{21} \equiv 0.75$; $C = 0.5$; see Fig. 4(a). Fig. 4(b) compares the IAST and RAST calculations of the $C_2H_4(1)/CO_2(2)$ adsorption selectivity; selectivity reversals at $y_1 < 0.4$ are evident. Fig. 4(c) presents a plot of the activity coefficients of C_2H_4, and CO_2 as a function of the adsorbed phase mole fraction of C_2H_4. The infinite dilution activity coefficients reduce by one to three orders of magnitude below unity, signaling strong thermodynamic non-idealities most likely caused by congregation of guest molecules around the extra-framework cations [9,16].

Drawing inspiration from the foregoing analysis of Calleja et al. [22] data, we analyzed the entire set of 28 experimental campaigns on transient breakthrough experiments to determine the adsorbed phase mole fractions of C_2H_4 and CO_2 using the shock-wave model for fixed-bed adsorbers developed in earlier work [7,8]; see Supplementary Material for calculation details. The x_1 vs y_1 plot, treating the mixture adsorption as a pseudo-binary $C_2H_4(1)/CO_2(2)$ mixture are shown in Fig. 5. The treatment of the feed mixtures as a pseudo-binary $C_2H_4(1)/CO_2(2)$ mixture is justified because these two components are significantly more strongly adsorbed than N_2, Ar, H_2, CH_4, C_2H_6, and CO; therefore the adsorption of C_2H_4, and CO_2 may be assumed to be practically independent of the presence of their partner species in the feed mixtures. The entire data set at three different pressures p_t = 1, 6 and 11 bar and 313 K are well described by the RAST model with the fitted Wilson parameters: $\Lambda_{12} = 25$; $\Lambda_{21} = 1$; $C = 1$. For $y_1 < 0.5$,

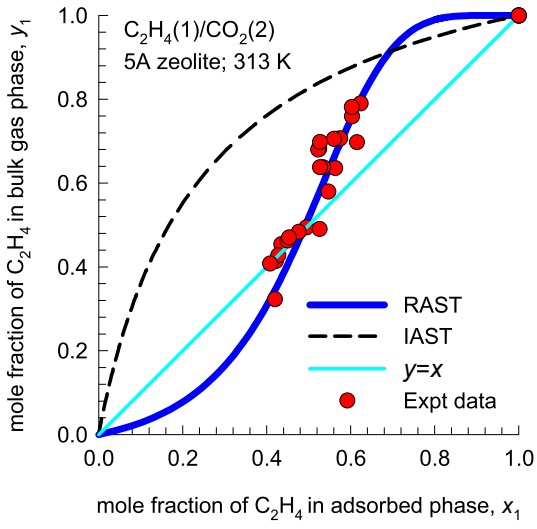

Fig. 5. Experimental data, obtained at 313 K and total pressure of 1 bar, 6 bar, and 11 bar, for adsorption of pseudo-binary $C_2H_4(1)/CO_2(2)$ mixtures in LTA-5A zeolite; the mole fraction of C_2H_4 in the bulk gas phase mixture is plotted as a function of the adsorbed phase mole fraction of C_2H_4. The plotted data are based on the 28 experimental campaigns on transient experimental breakthrough, determined using of the shock-wave model. Further details are provided in the Supplementary material.

the selectivity is in favor of C_2H_4. This implies that for selective adsorption of C_2H_4 from CO_2-bearing mixtures is feasible provided the C_2H_4/CO_2 ratio in the feed mixture is lower than unity.

Simulations of the transient breakthrough experiments in Fig. 2 using the RAST description of mixture adsorption equilibrium are presented in Fig. 6. The introduction of Wilson coefficients to describe the non-idealities for the C_2H_4/CO_2 pair of guest molecules is able to capture the selectivity reversal phenomena, as observed in the set of four experiments.

Further experimental evidence of selectivity reversals in favor of C_2H_4 for feed mixtures with C_2H_4/CO_2 lower than unity are provided in the experiments reported by García et al. [17]. For breakthroughs of CH_4/N_2, C_2H_6/N_2, C_2H_4/N_2, and CO_2/N_2 mixtures in a fixed bed packed with LTA-5A zeolite, the hierarchy of breakthrough times is $CH_4 < C_2H_6 < C_2H_4 < CO_2$, reflecting the stronger adsorption strength of CO_2 compared to C_2H_4; see Fig. 7(a). However, for breakthroughs of 20/80 C_2H_4/CO_2 and 40/4/49/7 $CH_4/C_2H_6/CO_2/C_2H_4$ mixtures, selectivity reversals are observed and CO_2 breaks through earlier than C_2H_4; see Fig. 7(b, c, d). Breakthrough simulations using the RAST model with the fitted Wilson parameters: $\Lambda_{12} = 15$; $\Lambda_{21} = 1$; $C = 1$ are shown by the continuous solid lines in Fig. 7; the RAST simulations are able to capture, quantitatively, the selectivity reversal in favor of C_2H_4 as observed in the experiments.

4. Conclusions

Transient breakthrough experiments with $H_2/CH_4/C_2H_6/CO/CO_2/C_2H_4$ feed mixtures in fixed beds packed with LTA-5A zeolite were carried out to investigate the feasibility of recovery of C_2H_4. Analysis of a set of 28 experimental breakthrough campaigns revealed that when C_2H_4/CO_2 ratios in the feed mixture are greater than unity, the CO_2 is selectively adsorbed and C_2H_4 recovery is infeasible. However, when C_2H_4/CO_2 ratios in the feed mixture are lower than unity, C_2H_4 is selectively adsorbed and recovery of C_2H_4 is feasible. Use of the IAST for prediction of mixture adsorption equilibrium does not anticipate the observed selectivity reversals, and are indicative of strong non-idealities in mixture adsorption. Use of the RAST, with Wilson equation for activity coefficients provides a quantitative description of selectivity reversals. The overall conclusion to emerge from this study is that thermodynamic non-idealities are the primary enablers for selective recovery of C_2H_4 from producer gas. Our investigation also underscores the need to perform transient breakthrough experiments with representative producer gas mixtures.

Further research is necessary to establish the precise reasons for manifestation of thermodynamic non-idealities in C_2H_4/CO_2 mixture adsorption.

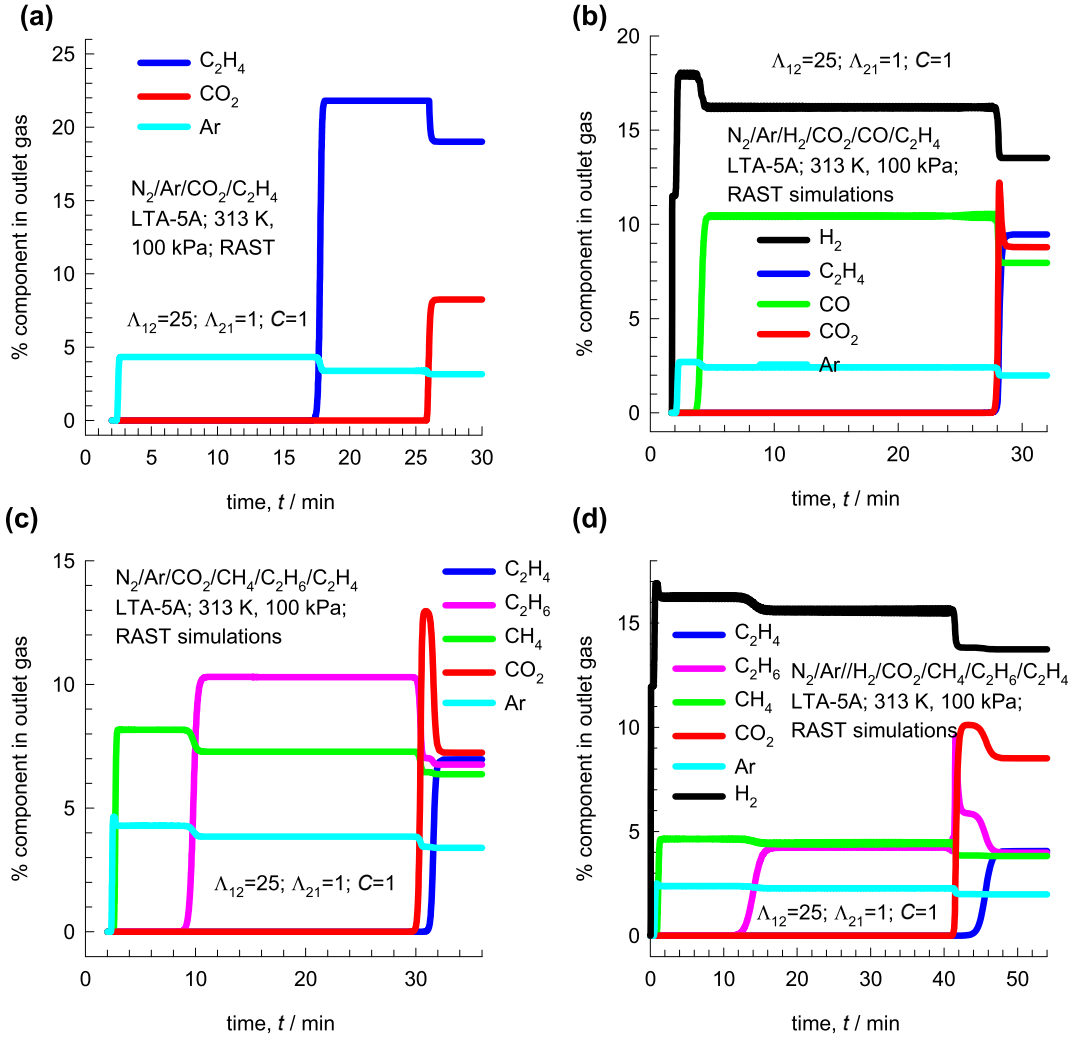

Fig. 6. Transient breakthrough simulations for the four sets of experimental data shown in Fig. 2. In these breakthrough simulations, the RAST model is used to describe mixture adsorption equilibria. The Wilson parameters $\Lambda_{12} = 25$; $\Lambda_{21} = 1$; $C = 1$ are used to describe the non-idealities for the C_2H_4/CO_2 pair; all other pairs of guest molecules are assumed to behave ideally. Further details are provided in the Supplementary material; see Figs. S34–S44.

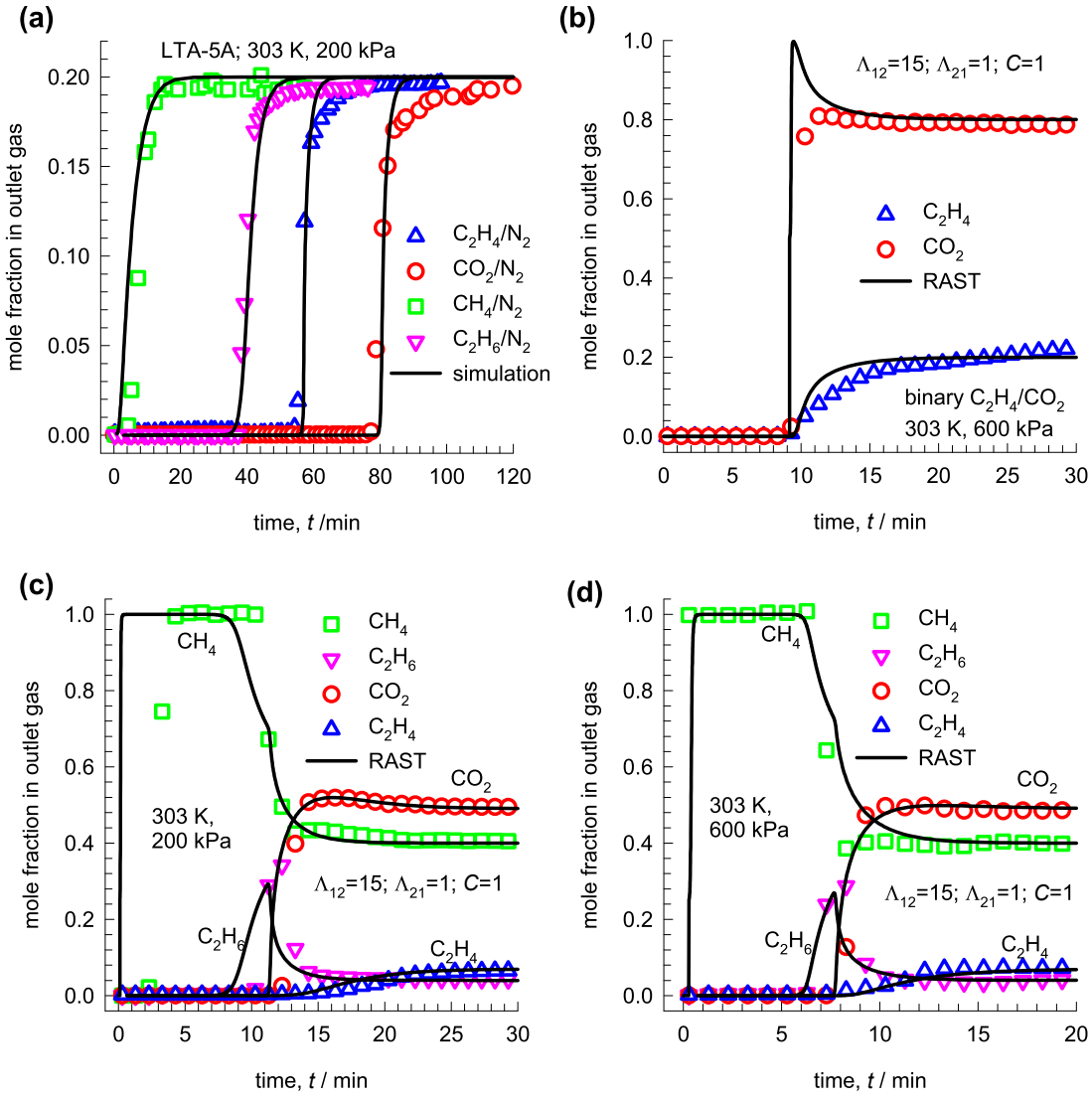

Fig. 7. (a, b, c, d) Experimental data (indicated by symbols) of García et al. [17]. for breakthroughs of a variety of mixtures in a fixed bed packed with LTA-5A zeolite operating at 303 K. (a) Breakthrough of CH_4/N_2, C_2H_6/N_2, C_2H_4/N_2, and CO_2/N_2 mixtures at p_t = 2 bar. (b) Breakthrough of 20/80 C_2H_4/CO_2 mixtures at p_t = 6 bar. (c) Breakthrough of 40/4/49/7 $CH_4/C_2H_6/CO_2/C_2H_4$ mixtures at p_t = 2 bar. (d) Breakthrough of 40/4/49/7 $CH_4/C_2H_6/CO_2/C_2H_4$ mixtures at p_t = 6 bar. The continuous solid lines in (a, b, c, d) represent breakthrough simulations in which the RAST model is used to describe mixture adsorption equilibria. The Wilson parameters $\Lambda_{12} = 15$; $\Lambda_{21} = 1$; $C = 1$ are used to describe the non-idealities for the C_2H_4/CO_2 pair; all other pairs of guest molecules are assumed to behave ideally. Further details are provided in the Supplementary material.

Acknowledgement

Professor Álvaro Orjuela, Universidad Nacional de Colombia, graciously provided Excel data files with the experimental data on transient breakthroughs that are compared in Fig. 7 with RAST breakthrough simulations.

Appendix A. Supplementary material

Supplementary data to this article can be found online at https://doi.org/10.1016/j.seppur.2019.115730.

References

[1] C.M. Van der Meijden, Development of the MILENA Gasification Technology for the Production of Bio-SNG, Ph.D. Thesis, Ph.D. Dissertation Eindhovent University of Technology, Eindhoven, 2010.
[2] M. Mofarahi, S.M. Salehi, Pure and binary adsorption isotherms of ethylene and ethane on zeolite 5A, Adsorption 19 (2013) 101–110.
[3] S. Pakseresht, M. Kazemeini, M.M. Akbarnejad, Equilibrium isotherms for CO, CO_2, CH_4 and C_2H_4 on the 5A molecular sieve by a simple volumetric apparatus, Sep. Purif. Technol. 28 (2002) 53–60.
[4] S. Sircar, T.C. Golden, Purification of hydrogen by pressure swing adsorption, Separ. Sci. Technol. 35 (2000) 667–687.
[5] S. Sircar, A.L. Myers, Gas separation by zeolites, Chapter 22, in: S.M. Auerbach, K.A. Carrado, P.K. Dutta (Eds.), Handbook of Zeolite Science and Technology, Marcel Dekker, New York, 2003, pp. 1063–1104.
[6] R. Krishna, Methodologies for evaluation of metal-organic frameworks in separation applications, RSC Adv. 5 (2015) 52269–52295.
[7] R. Krishna, Screening metal-organic frameworks for mixture separations in fixed-bed adsorbers using a combined selectivity/capacity metric, RSC Adv. 7 (2017) 35724–35737, https://doi.org/10.1039/C7RA07363A.
[8] R. Krishna, Methodologies for screening and selection of crystalline microporous materials in mixture separations, Sep. Purif. Technol. 194 (2018) 281–300, https://doi.org/10.1016/j.seppur.2017.11.056.
[9] R. Krishna, J.M. van Baten, R. Baur, Highlighting the origins and consequences of thermodynamic nonidealities in mixture separations using zeolites and metal-organic frameworks, Micropor. Mesopor. Mater. 267 (2018) 274–292, https://doi.org/10.1016/j.micromeso.2018.03.013.
[10] I. van Zandvoort, G.P.M. van Klink, E. de Jong, J.C. van der Waal, Selectivity and stability of zeolites [Ca]A and [Ag]A towards ethylene adsorption and desorption from complex gas mixtures, Micropor. Mesopor. Mat. 263 (2018) 142–149.
[11] M. Luberti, D. Friedrich, S. Brandani, H. Ahn, Design of a H_2 PSA for cogeneration of ultrapure hydrogen and power at an advanced integrated gasification combined cycle with pre-combustion capture, Adsorption 20 (2014) 511–524, https://doi.

org/10.1007/s10450-013-9598-0.
[12] H. Wu, K. Yao, Y. Zhu, B. Li, Z. Shi, R. Krishna, J. Li, Cu-TDPAT, an *rht*-type dual-functional metal-organic framework offering significant potential for use in H_2 and natural gas purification processes operating at high pressures, J. Phys. Chem. C 116 (2012) 16609–16618.
[13] R. Krishna, Highlighting the influence of thermodynamic coupling on kinetic separations with microporous crystalline materials, ACS Omega 4 (2019) 3409–3419, https://doi.org/10.1021/acsomega.8b03480.
[14] Z.R. Herm, R. Krishna, J.R. Long, CO_2/CH_4, CH_4/H_2 and $CO_2/CH_4/H_2$ separations at high pressures using Mg_2(dobdc), Micropor. Mesopor. Mater. 151 (2012) 481–487.
[15] Z.R. Herm, J.A. Swisher, B. Smit, R. Krishna, J.R. Long, Metal-organic frameworks as adsorbents for hydrogen purification and pre-combustion carbon dioxide capture, J. Am. Chem. Soc. 133 (2011) 5664–5667.
[16] R. Krishna, J.M. Van Baten, Investigating the non-idealities in adsorption of CO_2-bearing mixtures in cation-exchanged zeolites, Sep. Purif. Technol. 206 (2018) 208–217, https://doi.org/10.1016/j.seppur.2018.06.009.
[17] L. García, Y.A. Poveda, G. Rodríguez, E. Esche, H.R. Godini, G. Wozny, J.-U. Repke, A. Orjuela, Adsorption separation of oxidative coupling of methane effluent gases. Miniplant scale experiments and modeling, J. Nat. Gas Sci. Eng. 61 (2019) 106–118, https://doi.org/10.1016/j.jngse.2018.11.007.
[18] A.L. Myers, J.M. Prausnitz, Thermodynamics of mixed-gas adsorption, AIChE J. 11 (1) (1965) 121–127, https://doi.org/10.1002/(ISSN)1547-590510.1002/aic.v11:110.1002/aic.690110125.
[19] Flor R. Siperstein, Alan L. Myers, Mixed-gas adsorption, AIChE J. 47 (5) (2001) 1141–1159, https://doi.org/10.1002/(ISSN)1547-590510.1002/aic.v47:510.1002/aic.690470520.
[20] M. Mofarahi, F. Gholipour, Gas adsorption separation of CO_2/CH_4 system using zeolite 5A, Micropor. Mesopor. Mater. 200 (2014) 47–54.
[21] R. Krishna, The Maxwell-Stefan description of mixture diffusion in nanoporous crystalline materials, Micropor. Mesopor. Mater. 185 (2014) 30–50.
[22] G. Calleja, J. Pau, P. Pérez, J.A. Calles, Binary and ternary adsorption equilibria at high pressure on molecular sieves, in: L. M.D. (Ed.), Fundamentls of Adsorption FOA, vol. 356, The Kluwer International Series in Engineering and Computer Science, Boston, Massachusetts, 1996, pp. 147–154, , https://doi.org/10.1007/978-1-4613-1375-5_17.
[23] Orhan Talu, Alan L. Myers, Rigorous thermodynamic treatment of gas adsorption, AIChE J. 34 (11) (1988) 1887–1893, https://doi.org/10.1002/(ISSN)1547-590510.1002/aic.v34:1110.1002/aic.690341114.
[24] O. Talu, I. Zwiebel, Multicomponent adsorption equilibria of nonideal mixtures, AIChE J. 32 (1986) 1263–1276.

Highlighting Non-Idealities in C_2H_4/CO_2 Mixture Adsorption in 5A Zeolite

Ilona van Zandvoort, Jan Kees van der Waal,

Erik-Jan Ras, Robbert de Graaf

Avantium Chemicals B.V.

Zekeringstraat 29

1014 BV Amsterdam, The Netherlands

and

Rajamani Krishna*

Van 't Hoff Institute for Molecular Sciences

University of Amsterdam

Science Park 904

1098 XH Amsterdam, The Netherlands

email: r.krishna@contact.uva.nl

Table of Contents

1 Preamble

This Supporting Information accompanying the article *Highlighting Non-Idealities in C_2H_4/CO_2 Mixture Adsorption in 5A Zeolite* provides:

(a) Structural information on LTA-5A zeolite

(b) Brief summary of the IAST and RAST for calculation of mixture adsorption equilibrium

(c) Methodology used for transient breakthroughs in fixed bed adsorbers

(d) Unary isotherm data for guest molecules in LTA-5A zeolite

(e) Details of experimental breakthroughs, 28 campaigns at different operating pressures, 1 bar, 6 bar, and 11 bar.

(f) Detailed comparisons of experimental breakthroughs with transient breakthrough simulations

For ease of reading, the Supplementary Material is written as a stand-alone document.

2 Structural properties of LTA-5A zeolite

The crystallographic data are available on the zeolite atlas website of the International Zeolite Association (IZA).[1, 2] LTA-5A consist of cages of 743 $Å^3$ volume, separated by 4.11 Å × 4.47 Å 8-ring windows; the pore landscapes and structural details are provided in Figure S1 and Figure S2.

Per unit cell, LTA-5A has 96 Si, 96 Al, 32 Na^+, 32 Ca^{++} with Si/Al=1.

2.1 List of Figures for Structural properties of LTA-5A zeolite

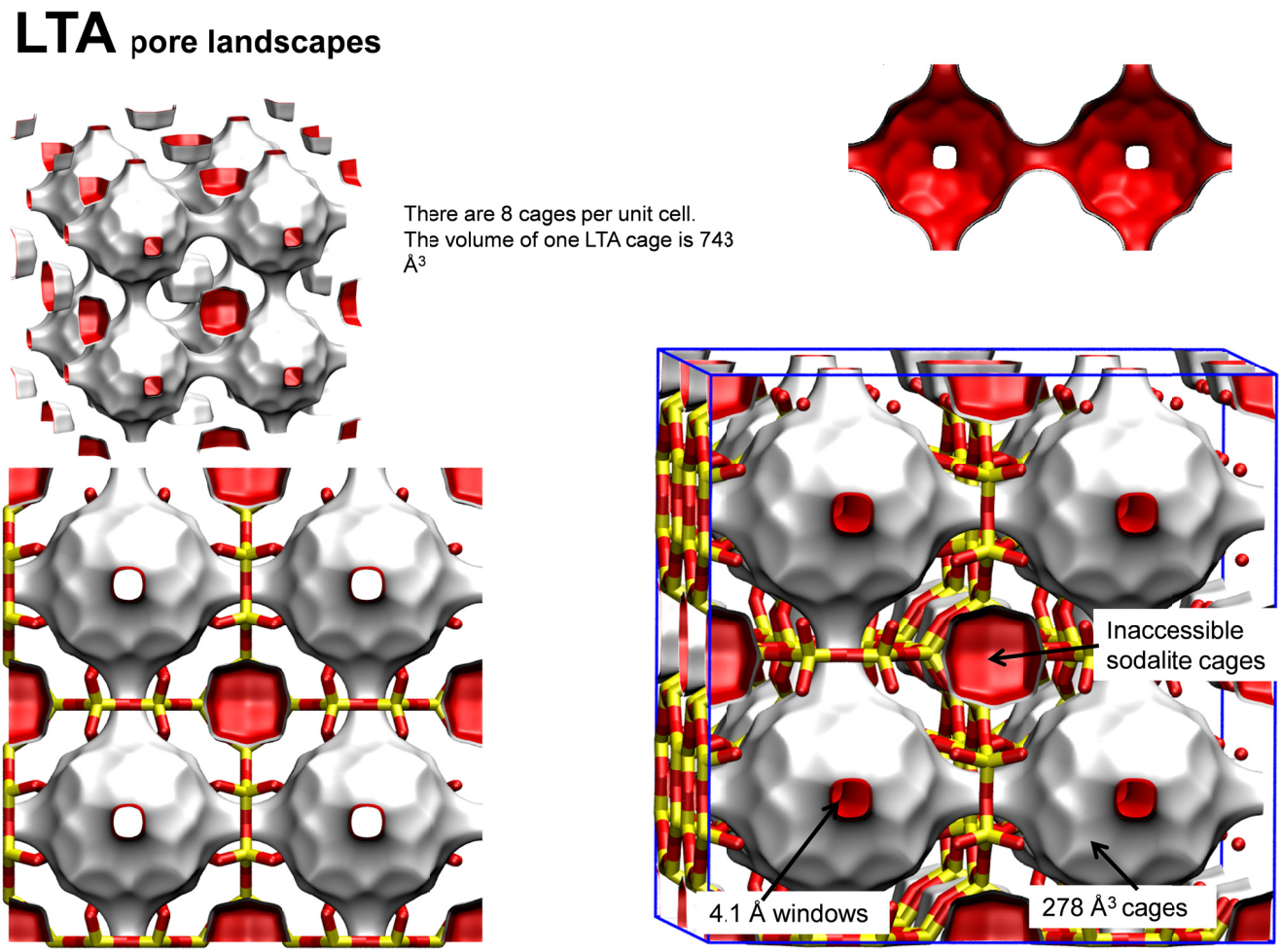

Figure S1. Pore landscape of LTA zeolite.

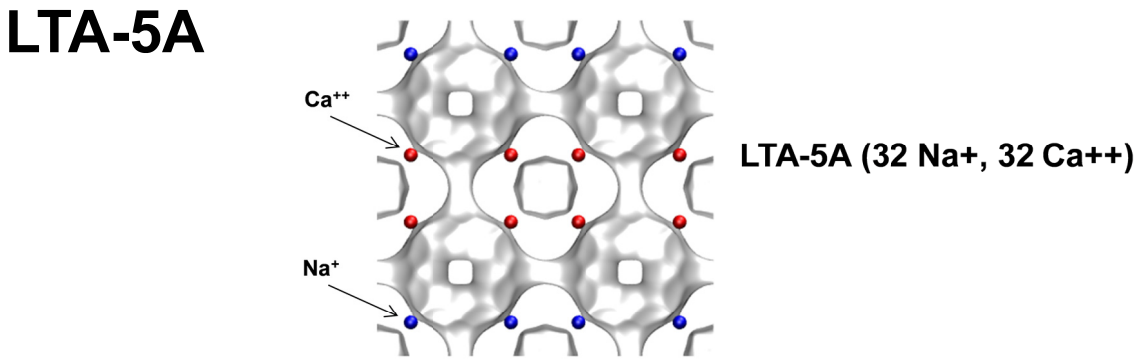

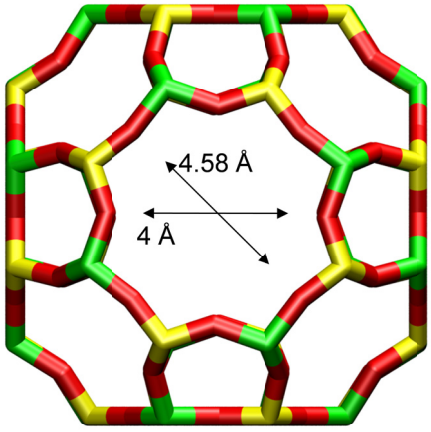

LTA-5A

The window dimension calculated using the van der Waals diameter of framework atoms = 2.7 Å is indicated above by the arrow.

	LTA-5A
a /Å	24.555
b /Å	24.555
c /Å	24.555
Cell volume / Å^3	14805.39
conversion factor for [molec/uc] to [mol per kg Framework]	0.0744
conversion factor for [molec/uc] to [kmol/m^3]	0.2955
ρ [kg/m3] (with cations)	1508.376
MW unit cell [g/mol framework+cations)]	13448.48
ϕ, fractional pore volume	0.380
open space / Å^3/uc	5620.4
Pore volume / cm^3/g	0.252
Surface area /m^2/g	
DeLaunay diameter /Å	4.00

Figure S2. Structural details for LTA-5A zeolite.

3 The Ideal Adsorbed Solution Theory (IAST)

3.1 Brief outline of theory

Within microporous crystalline materials, the guest molecules exist in the adsorbed phase. The Gibbs adsorption equation[3] in differential form is

$$Ad\pi = \sum_{i=1}^{n} q_i d\mu_i \tag{S1}$$

The quantity A is the surface area per kg of framework, with units of m^2 per kg of the framework of the crystalline material; q_i is the molar loading of component i in the adsorbed phase with units moles per kg of framework; μ_i is the molar chemical potential of component i. The spreading pressure π has the same units as surface tension, i.e. N m^{-1}.

The chemical potential of any component in the adsorbed phase, μ_i, equals that in the bulk fluid phase. If the partial fugacities in the bulk fluid phase are f_i, we have

$$d\mu_i = RTd\ln f_i \tag{S2}$$

where R is the gas constant (= 8.314 J mol^{-1} K^{-1}).

Briefly, the basic equation of Ideal Adsorbed Solution Theory (IAST) theory of Myers and Prausnitz[4] is the analogue of Raoult's law for vapor-liquid equilibrium, i.e.

$$f_i = P_i^0 x_i; \quad i = 1,2,..n \tag{S3}$$

where x_i is the mole fraction in the adsorbed phase

$$x_i = \frac{q_i}{q_1 + q_2 + ...q_n} \tag{S4}$$

and P_i^0 is the pressure for sorption of every component *i*, which yields the same spreading pressure, π for each of the pure components, as that for the mixture:

$$\frac{\pi A}{RT} = \int_0^{P_1^0} \frac{q_1^0(f)}{f} df = \int_0^{P_2^0} \frac{q_2^0(f)}{f} df = \int_0^{P_3^0} \frac{q_3^0(f)}{f} df = ... \tag{S5}$$

where $q_i^0(f)$ is the *pure* component adsorption isotherm. The units of $\frac{\pi A}{RT}$, also called the adsorption potential,[5] are mol kg^{-1}.

The unary isotherm may be described by say the 1-site Langmuir isotherm

$$q^0(f) = q_{sat} \frac{bf}{1+bf}; \quad \theta = \frac{bf}{1+bf} \tag{S6}$$

where we define the fractional *occupancy* of the adsorbate molecules, $\theta = q^0(f)/q_{sat}$. The superscript 0 is used to emphasize that $q^0(f)$ relates the *pure component* loading to the bulk fluid fugacity. More generally, the unary isotherms may need to be described by, say, the dual-site Langmuir model

$$q^0(f) = q_{A,sat} \frac{b_A f}{1+b_A f} + q_{B,sat} \frac{b_B f}{1+b_B} \tag{S7}$$

Each of the integrals in Equation (S5) can be evaluated analytically:

$$\begin{aligned} \int_{f=0}^{P_i^0} \frac{q^0(f)}{f} df &= q_{A,sat} \ln\left(1+b_A\left(P_i^0\right)\right) + q_{B,sat} \ln\left(1+b_B\left(P_i^0\right)\right) \\ \int_{f=0}^{P_i^0} \frac{q^0(f)}{f} df &= q_{A,sat} \ln\left(1+b_A\left(\frac{f_i}{x_i}\right)\right) + q_{B,sat} \ln\left(1+b_B\left(\frac{f_i}{x_i}\right)\right) \end{aligned} \tag{S8}$$

The right hand side of equation (S8) is a function of P_i^0. For multicomponent mixture adsorption, each of the equalities on the right hand side of Equation (S5) must be satisfied. These constraints may be solved using a suitable equation solver, to yield the set of values of P_1^0, P_2^0, P_3^0,.. P_n^0, all of which satisfy Equation (S5). The corresponding values of the integrals using these as upper limits of integration must yield the same value of $\frac{\pi A}{RT}$ for each component; this ensures that the obtained solution is the correct one.

The adsorbed phase mole fractions x_i are then determined from

$$x_i = \frac{f_i}{P_i^0}; \quad i = 1,2,...n \tag{S9}$$

A key assumption of the IAST is that the enthalpies and surface areas of the adsorbed molecules do not change upon mixing. If the total mixture loading is q_t, the area covered by the adsorbed mixture is $\frac{A}{q_t}$ with units of m^2 (mol mixture)$^{-1}$. Therefore, the assumption of no surface area change due to mixture adsorption translates as $\frac{A}{q_t} = \frac{Ax_1}{q_1^0\left(P_1^0\right)} + \frac{Ax_2}{q_2^0\left(P_2^0\right)} + \cdots \frac{Ax_n}{q_n^0\left(P_n^0\right)}$; the total mixture loading is q_t is calculated from

$$q_t = q_1 + q_2 ... + q_n = \frac{1}{\frac{x_1}{q_1^0(P_1^0)} + \frac{x_2}{q_2^0(P_2^0)} + ... + \frac{x_n}{q_n^0(P_n^0)}} \tag{S10}$$

in which $q_1^0(P_1^0)$, $q_2^0(P_2^0)$,… $q_n^0(P_n^0)$ are determined from the unary isotherm fits, using the sorption pressures for each component P_1^0, P_2^0, P_3^0,.. P_n^0 that are available from the solutions to equations Equations (S5), and (S8).

The entire set of equations (S3) to (S10) need to be solved numerically to obtain the loadings, q_i of the individual components in the mixture.

4 The Real Adsorbed Solution Theory (RAST)

To account for non-ideality effects in mixture adsorption, we introduce activity coefficients γ_i into Equation (S3) [4]

$$f_i = P_i^0 x_i \gamma_i \tag{S11}$$

Following the approaches of Myers, Talu, and Sieperstein[5-7] we model the excess Gibbs free energy for binary mixture adsorption as follows

$$\frac{G^{excess}}{RT} = x_1 \ln(\gamma_1) + x_2 \ln(\gamma_2) \tag{S12}$$

The Wilson model for activity coefficients are given for binary mixtures by

$$\begin{aligned}
\ln(\gamma_1) &= \left(1 - \ln(x_1\Lambda_{11} + x_2\Lambda_{12}) - \frac{x_1\Lambda_{11}}{x_1\Lambda_{11} + x_2\Lambda_{12}} - \frac{x_2\Lambda_{21}}{x_2 + x_1\Lambda_{21}}\right)\left(1 - \exp\left(-C\frac{\pi A}{RT}\right)\right) \\
\ln(\gamma_2) &= \left(1 - \ln(x_1\Lambda_{21} + x_2\Lambda_{22}) - \frac{x_1\Lambda_{12}}{x_1\Lambda_{11} + x_2\Lambda_{12}} - \frac{x_2\Lambda_{22}}{x_1\Lambda_{21} + x_2\Lambda_{22}}\right)\left(1 - \exp\left(-C\frac{\pi A}{RT}\right)\right)
\end{aligned} \tag{S13}$$

In Equation (S13), $\Lambda_{11} \equiv 1; \quad \Lambda_{22} \equiv 1$, and C is a constant with the units kg mol^{-1}. The introduction of $\left(1 - \exp\left(-C\frac{\pi A}{RT}\right)\right)$ imparts the correct limiting behaviors $\gamma_i \to 1; \quad \frac{\pi A}{RT} \to 0$ for the activity coefficients in the Henry regime, $f_t \to 0; \quad \frac{\pi A}{RT} \to 0$. As pore saturation conditions are approached, this correction factor tends to unity $\left(1 - \exp\left(-C\frac{\pi A}{RT}\right)\right) \to 1$. The choice of $\Lambda_{12} = \Lambda_{21} = 1$ in Equation (S13), yields unity values for the activity coefficients.

The excess reciprocal loading for the mixture can be defined as

$$\left(\frac{1}{q_t}\right)^{excess} = \frac{1}{q_t} - \left(\frac{x_1}{q_1^0(P_1^0)} + \frac{x_2}{q_2^0(P_2^0)}\right) \tag{S14}$$

The excess reciprocal loading for the mixture can be related to the partial derivative of the Gibbs free energy with respect to the adsorption potential at constant composition

$$\left(\frac{1}{q_t}\right)^{excess} = \left.\frac{\partial\left(\frac{G^{excess}}{RT}\right)}{\partial\left(\frac{\pi A}{RT}\right)}\right|_{T,x} = \left[-x_1\ln(x_1+x_2\Lambda_{12}) - x_2\ln\left(x_2+x_1\Lambda_{21}\right)\right]C\exp\left(-C\frac{\pi A}{RT}\right) \tag{S15}$$

For calculation of the total mixture loading we need to replace Equation (S10) by

$$q_t \equiv q_1 + q_2 = \frac{1}{\frac{x_1}{q_1^0(P_1^0)} + \frac{x_2}{q_2^0(P_2^0)} + \left[-x_1\ln(x_1+x_2\Lambda_{12}) - x_2\ln\left(x_2+x_1\Lambda_{21}\right)\right]C\exp\left(-C\frac{\pi A}{RT}\right)} \tag{S16}$$

The parameters Λ_{12}, Λ_{21}, and C can be fitted to match the experimental data on mixture adsorption. The implementation of the activity coefficients is termed as the Real Adsorbed Solution Theory (RAST).

5 Simulation methodology for transient breakthroughs

Fixed beds, packed with crystals of microporous materials, are commonly used for separation of mixtures (see schematic in Figure S3); such adsorbers are commonly operated in a transient mode, and the compositions of the gas phase, and component loadings within the crystals, vary with position and time. During the initial stages of the transience, the pores are loaded up gradually, and only towards the end of the adsorption cycle are conditions corresponding to pore saturation attained. Put another way, separations in fixed bed adsorbers are influenced by both the Henry regime of adsorption as well as the conditions corresponding to pore saturation. For a given separation task, transient breakthroughs provide more a realistic evaluation of the efficacy of a material, as they reflect the combined influence of adsorption selectivity, and adsorption capacity.[8, 9]

We describe below the simulation methodology used to perform transient breakthrough calculations that are presented in this work. This simulation methodology is the same as that used in our previous published works.[8-11]

Assuming plug flow of an *n*-component gas mixture through a fixed bed maintained under isothermal, isobaric, conditions, the molar concentrations in the gas phase at any position and instant of time are obtained by solving the following set of partial differential equations for each of the species *i* in the gas mixture.[12]

$$\frac{\partial c_i(t,z)}{\partial t}+\frac{\partial\left(v(t,z)c_i(t,z)\right)}{\partial z}+\frac{\left(1-\varepsilon\right)}{\varepsilon}\rho\frac{\partial \bar{q}_i(t,z)}{\partial t}=0;\quad i=1,2,...n \tag{S17}$$

In Equation (S17), t is the time, z is the distance along the adsorber, ρ is the framework density, ε is the bed voidage, v is the interstitial gas velocity, and $\bar{q}_i(t,z)$ is the *spatially averaged* molar loading within the crystallites of radius r_c, monitored at position z, and at time t. The time $t = 0$, corresponds to the time

at which the feed mixture is injected at the inlet to the fixed bed. Prior to injection of the feed, it is assumed that an inert, non-adsorbing, gas flows through the fixed bed.

At any time t, during the transient approach to thermodynamic equilibrium, the spatially averaged molar loading within the crystallite r_c is obtained by integration of the radial loading profile

$$\bar{q}_i(t) = \frac{3}{r_c^3}\int_0^{r_c} q_i(r,t) r^2 dr \tag{S18}$$

For transient unary uptake within a crystal at any position and time with the fixed bed, the radial distribution of molar loadings, q_i, within a spherical crystallite, of radius r_c, is obtained from a solution of a set of differential equations describing the uptake

$$\frac{\partial q_i(r,t)}{\partial t} = -\frac{1}{\rho}\frac{1}{r^2}\frac{\partial}{\partial r}\left(r^2 N_i\right) \tag{S19}$$

The molar flux N_i of component i may be described by the appropriate formulations of Maxwell-Stefan equations, discussed in the foregoing sections.

Summing Equation (S19) over all n species in the mixture allows calculation of the *total average* molar loading of the mixture within the crystallite

$$\bar{q}_t(t,z) = \sum_{i=1}^{n} \bar{q}_i(t,z) \tag{S20}$$

The *interstitial* gas velocity is related to the *superficial* gas velocity by

$$v = \frac{u}{\varepsilon} \tag{S21}$$

The adsorber bed is assumed to be initially free of adsorbates, i.e. we have the initial condition

$$t = 0; \quad q_i(0,z) = 0 \tag{S22}$$

Equation (S22) is relevant to the operation of the transient breakthrough experiments on a laboratory scale, but are not truly reflective of industrial operations.

At time, $t = 0$, the inlet to the adsorber, $z = 0$, is subjected to a step input of the n-component gas mixture and this step input is maintained till the end of the adsorption cycle when steady-state conditions are reached.

Simulation methodology for transient breakthroughs

$$t \geq 0; \quad p_i(0,t) = p_{i0}; \quad u(0,t) = u_0 \tag{S23}$$

where $u_0 = v_0 \varepsilon$ is the superficial gas velocity at the inlet to the adsorber.

If the value of $\frac{Đ_i}{r_c^2}$ is large enough to ensure that intra-crystalline gradients are absent and the entire crystallite particle can be considered to be in thermodynamic equilibrium with the surrounding bulk gas phase at that time *t*, and position *z* of the adsorber

$$\bar{q}_i(t,z) = q_i(t,z) \tag{S24}$$

The molar loadings at the *outer surface* of the crystallites, i.e. at $r = r_c$, are calculated on the basis of adsorption equilibrium with the bulk gas phase partial pressures p_i at that position *z* and time *t*. The adsorption equilibrium can be calculated on the basis of the IAST or RAST descriptions of mixture adsorption equilibrium, as appropriate.

For convenience, the set of equations describing the fixed bed adsorber are summarized in Figure S3. Typically, the adsorber length is divided into 100 – 200 slices. Combination of the discretized partial differential equations (PDEs) along with the algebraic IAST or RAST equilibrium model, results in a set of differential-algebraic equations (DAEs), which are solved using BESIRK.[13] BESIRK is a sparse matrix solver, based on the semi-implicit Runge-Kutta method originally developed by Michelsen,[14] and extended with the Bulirsch-Stoer extrapolation method.[15] Use of BESIRK improves the numerical solution efficiency in solving the set of DAEs. The evaluation of the sparse Jacobian required in the numerical algorithm is largely based on analytic expressions.[12] Further details of the numerical procedures used in this work, are provided by Krishna and co-workers;[12, 16-18] interested readers are referred to our website that contains the numerical details.[16]

5.1 List of Figures for Simulation methodology for transient breakthroughs

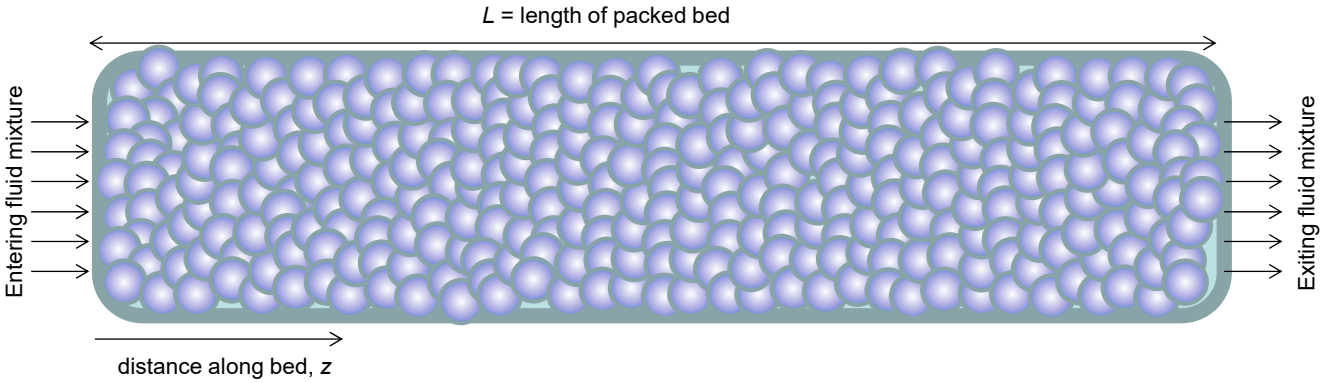

Figure S3. Schematic of a packed bed adsorber.

6 Fitting of unary isotherm data from literature sources

The unary isotherm data for C_2H_4 and C_2H_6 in LTA-5A zeolite as reported in Table 2 and Table 3 of Mofarahi and Salehi[19] at temperatures of 283 K, 303 K, and 323 K. were fitted with the dual-site Langmuir model

$$q = q_{A,sat}\frac{b_A p}{1+b_A p} + q_{B,sat}\frac{b_B p}{1+b_B p} \tag{S25}$$

with T-dependent parameters b_A, and b_B

$$b_A = b_{A0}\exp\left(\frac{E_A}{RT}\right); \quad b_B = b_{B0}\exp\left(\frac{E_B}{RT}\right) \tag{S26}$$

The fitted parameter values are presented in Table S1.

The unary isotherm data for CO_2 in LTA-5A zeolite as reported in Table A1 of Mofarahi and Gholipour[20] at temperatures of 273 K, 283 K, 303 K, 323 K, and 343 K were fitted with the dual-site Langmuir model; the parameter fits are presented in Table S2.

The unary isotherm data for CH_4 and N_2 in LTA-5A zeolite, as reported in Table 3 and Table 4 of Bakhtyari and Mofarahi[21] at temperatures of 273 K, 283 K, 303 K, 323 K, and 343 K were fitted with excellent accuracy with the single-site Langmuir model

$$q = q_{sat}\frac{bp}{1+bp}; \quad b = b_0\exp\left(\frac{E}{RT}\right) \tag{S27}$$

The fitted parameter values are presented in Table S3.

The dual-site Langmuir parameter fits for H_2 and CO in LTA-5A zeolite are provided in Table S4; these parameters are those reported in Table 3 of Jamali et al.[22]

In the breakthrough simulations, the isotherm fits for N_2 in LTA-5A zeolite were assumed to also hold for Ar.

6.1 List of Tables for Fitting of unary isotherm data from literature sources

Table S1. Dual-site Langmuir parameter fits for C_2H_4 and C_2H_6 in LTA-5A zeolite. These parameters are based on the unary isotherm data reported in Table 2 and Table 3 of Mofarahi and Salehi[19] at temperatures of 283 K, 303 K, and 323 K.

	Site A			Site B		
	$q_{A,sat}$ mol kg^{-1}	b_{A0} Pa^{-1}	E_A kJ mol^{-1}	$q_{B,sat}$ mol kg^{-1}	b_{B0} Pa^{-1}	E_B kJ mol^{-1}
C_2H_4	2.5	6.98E-08	19	0.75	4.18E-18	67
C_2H_6	2.1	1.35E-08	20	0.33	4.22E-23	96

Table S2. Dual-site Langmuir parameter fits for CO_2 in LTA-5A zeolite. These parameters are based on the unary isotherm data reported in Table A1 of Mofarahi and Gholipour[20] at temperatures of 273 K, 283 K, 303 K, 323 K, and 343 K.

	Site A			Site B		
	$q_{A,sat}$ mol kg^{-1}	b_{A0} Pa^{-1}	E_A kJ mol^{-1}	$q_{B,sat}$ mol kg^{-1}	b_{B0} Pa^{-1}	E_B kJ mol^{-1}
CO_2	1.5	4.5E-10	23.5	2.5	2.99E-12	49

Fitting of unary isotherm data from literature sources

Table S3. Single-site Langmuir parameter fits for CH_4 and N_2 in LTA-5A zeolite. These parameters are based on the unary isotherm data reported in Table 3 and Table 4 of Bakhtyari and Mofarahi[21] at temperatures of 273 K, 283 K, 303 K, 323 K, and 343 K.

	q_{sat} mol kg^{-1}	b_0 Pa^{-1}	E kJ mol^{-1}
CH_4	3.1	9.43E-10	19
N_2	2.5	1.68E-09	16.6

Table S4. Dual-site Langmuir parameter fits for H_2 and CO in LTA-5A zeolite. These parameters are those reported in Table 3 of Jamali et al.[22]

	Site A			Site B		
	$q_{A,sat}$ mol kg^{-1}	b_{A0} Pa^{-1}	E_A kJ mol^{-1}	$q_{B,sat}$ mol kg^{-1}	b_{B0} Pa^{-1}	E_B kJ mol^{-1}
H_2	0.4965	1.65E-08	7.62	0.03725	5.59E-09	14.1
CO	2.502	6.56E-11	24.13	1.182	1.88E-11	34.48

7 Experimental transient breakthrough experiments vs simulations

7.1 The Flowrence set-up

A Flowrence set-up is modified for the transient breakthrough experiments (Figure S4) such that the feed selector valve selects one reactor (= fixed-bed adsorber) tube, which is fed with the adsorption gas mixture. Meanwhile, all other reactors are fed with nitrogen (the desorption gas). A selector valve in the effluent is used to lead the effluent gas from the selected reactor to the mass spectrometer (Hiden Analytical HPR-20 QIC) and compact GC (Interscience) with TCD detector. The selected reactor is fed with the mixed gas feed and continuously monitored by the MS (10 s interval) and GC (1 min interval) to record breakthrough curves. [23]

The Flowrence has four heated reactor blocks (40 - 300 °C), each containing four reactors of 560 mm height, 6 mm OD and 4 mm ID that can be pressurized (0-10 barg). The isothermal zone was determined to be 200 mm. During a run, one blank and 15 sorbent materials can be tested. At the bottom of the reactor a diluent gas (N2) can be mixed with the effluent, which be used to dilute the gas flow before analysis, increase the flow rate and prevent back mixing under the reactor. At the start of each run, the materials are dried in the reactor under 25 mL/min N2 per reactor at 473 K for 2 h. The same procedure is used to desorb the sorbents between adsorption cycles.

The sorbent bed is 4 mm in diameter, and 37 cm +/- 0.7cm height. The sorbent beds are packed with 8-12 mesh 5A mol sieves from Acros. A layer of zirblast (inert diluent, particle size of 250 μm) was loaded in the reactors first to make sure that the sorbent bed is located in the isothermal zone. Zirblast is also used to fill up the interstitial void space between adsorbent particles and top of the reactors up to a height of 55 cm.

Different gas mixtures were used for testing of C_2H_4 adsorption; see Table S11. CO_2, and H_2 are mixed with the gas feed via separate mass flow controllers, using a total feed flow of 25 mL/min per

reactor. Transient breakthrough experiments are performed for N_2/Ar/H_2/CH_4/C_2H_6/CO/CO_2/C_2H_4 mixtures in tubes packed with LTA-5A zeolite, operating at 313 K, and total pressures of 1 bar (10 campaigns), 6 bar (7 campaigns), and 11 bar (5 campaigns). The feed mixture compositions for each campaign are specified in Table S5, Table S6, and Table S7. The fixed-bed tube is first flushed with pure N_2 at the specified total pressure, before injection of the feed mixture, at time $t = 0$. Ar is used as an inert internal standard to monitor the start of the adsorption experiment.

In the MS, ions are produced by electron ionization (EI), separated by a quadrupole analyzer and detected by a secondary electron multiplier (SEM). The raw signal was monitored at the selected m/z values, corrected for spectral overlap by taking into account the relative abundancies of the different peaks. The data was subsequently normalized to the signal of N_2 (relative sensitivity = 1). The selected m/z values and their relative sensitivities (RS) were calibrated using known concentrations of the gases. The percentage of each component is calculated based on the total normalized response. It should be noted that the molecular ion peaks of N_2, ethylene and CO are all observed at m/z 28. To overcome this spectral overlap, the ethylene signal is monitored at m/z 27. The signal from CO can therefore not be deconvoluted from the MS signal. Therefore, CO is monitored by GC and subtracted from the signal obtained at m/z 28 after correction for C_2H_4. Ethane is monitored at m/z 30 and concentrations are calculated taking into account the relative abundancies of the fragments.

7.2 Comparison of experimental breakthroughs with simulations

For the 28 experimental campaigns, transient breakthrough simulations were carried out with the assumption the equilibrium between the bulk gas mixture and the adsorbed phase in 5A zeolite could be described by the IAST. For the simulations of transient breakthroughs, the unary isotherm data fits are provided in Table S1, Table S2, Table S3, and Table S4.

In all of the experiments using the Flowrence set-up, the transient breakthroughs do not have distended characteristics; this indicates that intra-crystalline diffusion influences may be considered to

be of negligible importance. Consequently, in the transient breakthrough simulations, the values of $\frac{Đ_i}{r_c^2}$ are chosen to be large enough to ensure that intra-crystalline gradients are absent and the entire crystallite particle can be considered to be in thermodynamic equilibrium. The adsorber dimensions, and interstitial gas velocities are chosen to match the experimental conditions in each case.

The comparisons of experimental and simulated breakthoughs are presented in Figure S5, Figure S6, Figure S7, Figure S8, Figure S9, Figure S10, Figure S11, Figure S12, Figure S13, Figure S14, Figure S15, Figure S16, Figure S17, Figure S18, Figure S19, Figure S20, Figure S21. Figure S22, Figure S23, Figure S24, Figure S25, Figure S26, Figure S27, Figure S28, Figure S29, Figure S30, Figure S31, and Figure S32. In each simulation the operating conditions corresponding to the experiments (mass of 5A zeolite, molar flow rate of gas mixture, temperature, pressure, gas compositions) were employed. The following general observations apply to each of the 28 experimental campaigns. The breakthrough times of Ar, C_2H_4, C_2H_6, H_2, CH_4, CO, and N_2 are simulated adequately . However, in all cases, the breakhthough times for CO_2 in the simulations were significantly higher, in the simulations than observed in the experiments. More importantly, the selectivity reversals in favor of C_2H_4 as observed in Figure S13, and Figure S14 are not anticipated by the simulations, based on IAST calculations. The reasons for such deviations is attributable to non-idealities in mixture adsorption thermodynamics.[24-26]

7.3 List of Tables for Experimental transient breakthrough experiments vs simulations

Table S5. Set of 13 experimental campaigns carried out at a total pressure of 1 bar.

Run	*P*/ bar	%Ar	%C_2H_4	%C_2H_6	%CO_2	%H_2	%H_2O	%CH_4	%CO	%N_2
1	1	4.37	23.09	0.00	0.00	0.00	0.00	0.00	0.00	72.55
2	1	3.05	16.44	0.00	16.83	0.00	0.00	0.00	0.00	63.68
3	1	2.63	14.10	0.00	19.98	0.00	0.00	0.00	0.00	63.29
4	1	2.95	17.81	0.00	10.20	0.00	0.00	0.00	0.00	69.05
5	1	3.59	19.14	0.00	6.06	0.00	0.00	0.00	0.00	71.21
6	1	3.93	23.24	0.00	0.00	0.00	0.00	0.00	0.00	72.83
7	1	3.15	19.01	0.00	8.25	0.00	0.00	0.00	0.00	69.59
8	1	1.93	11.81	0.00	8.56	13.17	0.00	0.00	7.75	56.78
9	1	3.39	6.97	6.76	7.24	0.00	0.00	6.37	0.00	69.28
10	1	1.98	4.06	3.98	8.51	13.74	0.00	3.82	0.00	63.91
11	1	2.77	15.91	0.00	6.64	6.64	0.11	0.00	6.45	61.47
12	1	3.10	15.89	0.00	6.61	6.61	0.11	0.00	6.45	61.22
13	1	3.08	15.76	0.00	6.58	6.60	0.11	0.00	6.49	61.38

Experimental transient breakthrough experiments vs simulations

Table S6. Set of 8 experimental campaigns carried out at a total pressure of 6 bar.

Run	*P*/ bar	%Ar	%C_2H_4	%C_2H_6	%CO_2	%H_2	%H_2O	%CH_4	%CO	%N_2
14	6	3.92	22.25	0.00	0.00	0.00	0.00	0.00	0.00	73.83
15	6	3.01	16.02	0.00	17.11	0.00	0.00	0.00	0.00	63.86
16	6	2.54	13.70	0.00	19.88	0.00	0.00	0.00	0.00	63.87
17	6	2.81	17.98	0.00	10.21	0.00	0.00	0.00	0.00	69.00
18	6	3.50	19.39	0.00	5.43	0.00	0.00	0.00	0.00	71.69
19	6	4.97	15.55	4.88	18.04	0.10	0.05	5.01	0.77	50.63
20	6	3.86	11.41	3.66	12.86	24.84	0.04	3.61	0.50	39.24
21	6	2.78	15.40	0.00	6.66	6.68	0.11	0.00	6.35	62.01

Experimental transient breakthrough experiments vs simulations

Table S7. Set of 7 experimental campaigns carried out at a total pressure of 11 bar.

Run	*P*/ bar	%Ar	%C_2H_4	%C_2H_6	%CO_2	%H_2	%H_2O	%CH_4	%CO	%N_2
22	11	3.66	20.82	0	0	0	0	0	0	75.53
23	11	2.7	14.5	0	17.44	0	0	0	0	65.35
24	11	2.47	14.46	0	19.37	0	0	0	0	63.69
25	11	2.74	17.57	0	9.98	0	0	0	0	69.71
26	11	3.28	19.29	0	5.12	0	0	0	0	72.31
27	11	3.04	14.97	0	6.98	6.51	0.13	0	6.7	61.67
28	11	2.68	15.72	0	7.39	6.25	0.13	0	0	67.83

Experimental transient breakthrough experiments vs simulations

Table S8. Set of 13 experimental campaigns carried out at a total pressure of 1 bar.

Run	P/ bar	t_1 min	t_2 min	y_1	y_2	x_1	x_2
1	1	15.14		1	0	1	0
2	1	15.14	15.14	0.494138864	0.505861136	0.494138864	0.505861136
3	1	14.87	14.6	0.413732394	0.586267606	0.413732394	0.586267606
4	1	16.22	19.47	0.635844341	0.364155659	0.635844341	0.364155659
5	1	16.22	26.77	0.75952381	0.24047619	0.75952381	0.24047619
6	1	14.9		1	0	1	0
7	1	17.24	21.97	0.697358767	0.302641233	0.697358767	0.302641233
8	1	21.3	23	0.579774178	0.420225822	0.579774178	0.420225822
9	1	30	28	0.490499648	0.509500352	0.490499648	0.509500352
10	1	37	28.5	0.322991249	0.677008751	0.322991249	0.677008751
11	1	21	31	0.705543237	0.294456763	0.705543237	0.294456763
12	1	7.6	11	0.706222222	0.293777778	0.706222222	0.293777778
13	1	14.36	21.46	0.705461056	0.294538944	0.705461056	0.294538944

Experimental transient breakthrough experiments vs simulations

Table S9. Set of 8 experimental campaigns carried out at a total pressure of 6 bar.

Run	P/ bar	t_1 min	t_2 min	y_1	y_2	x_1	x_2
14	6	20.55		1	0	1	0
15	6	19.18	19.45	0.483549653	0.516450347	0.483549653	0.516450347
16	6	18.39	18.39	0.407980941	0.592019059	0.407980941	0.592019059
17	6	20.28	26.5	0.637814828	0.362185172	0.637814828	0.362185172
18	6	20.82	37.85	0.781224819	0.218775181	0.781224819	0.218775181
19	6	11.8	12.1	0.462935397	0.537064603	0.462935397	0.537064603
20	6	10.65	11	0.47012773	0.52987227	0.47012773	0.52987227
21	6	17.9	28.05	0.698096102	0.301903898	0.698096102	0.301903898

Experimental transient breakthrough experiments vs simulations

Table S10. Set of 5 experimental campaigns carried out at a total pressure of 11 bar.

Run	P/ bar	t_1 min	t_2 min	y_1	y_2	x_1	x_2
22	11	24.34		1	0	1	0
23	11	22.17	22.98	0.453976205	0.546023795	0.453976205	0.546023795
24	11	21.09	21.09	0.427431274	0.572568726	0.427431274	0.572568726
25	11	23.52	30.28	0.637749546	0.362250454	0.637749546	0.362250454
26	11	23.79	42.72	0.790249898	0.209750102	0.790249898	0.209750102
27	11	22.98	34.34	0.682004556	0.317995444	0.682004556	0.317995444
28	11	23	34.34	0.680225011	0.319774989	0.680225011	0.319774989

Experimental transient breakthrough experiments vs simulations

Table S11. Gas mixtures available.

	Mixture 1 mol%	Mixture 2 mol %
C_2H_4	30	10
C_2H_6	0	10
CH_4	0	10
CO	0	0
Ar	5	5
N_2	65	65

7.4 List of Figures for Experimental transient breakthrough experiments vs simulations

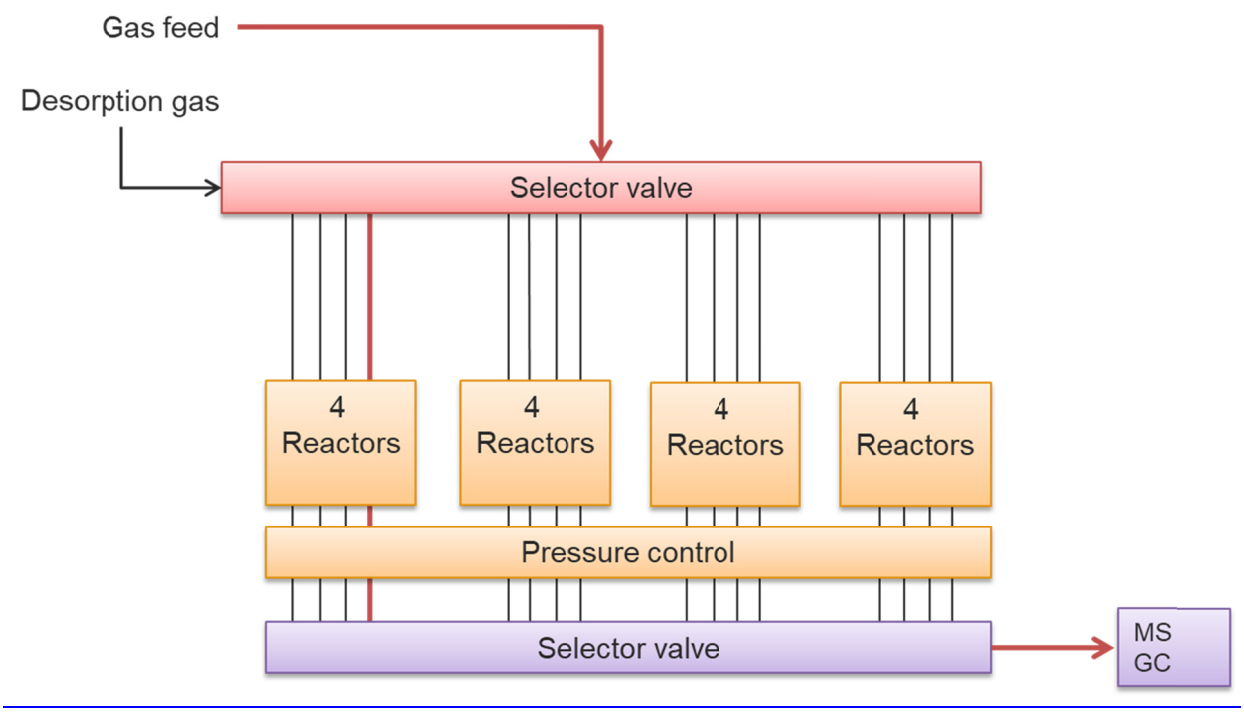

Figure S4. Schematic of experimental set up for transient breakthroughs.

Experimental transient breakthrough experiments vs simulations

T/ K	*P*/ bar	%Ar	%C_2H_4	%C_2H_6	%CO_2	%H_2	%H_2O	%CH_4	%CO	%N_2
313	1	4.37	23.09	0.00	0.00	0.00	0.00	0.00	0.00	72.55

(a) Breakthrough experiments

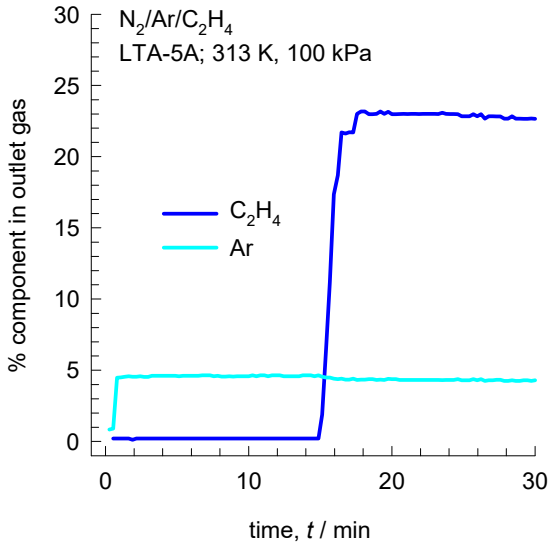

(b) Breakthrough simulations based on IAST

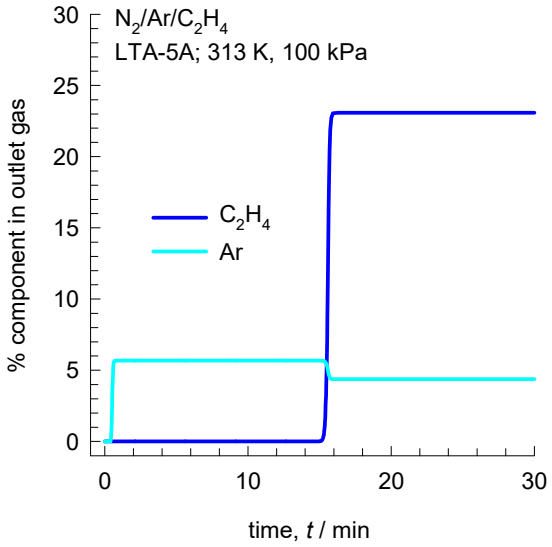

Figure S5. Run 1 at 1 bar.

Experimental transient breakthrough experiments vs simulations

T/ K	*P*/ bar	%Ar	%C_2H_4	%C_2H_6	%CO_2	%H_2	%H_2O	%CH_4	%CO	%N_2
313	1	3.05	16.44	0.00	16.83	0.00	0.00	0.00	0.00	63.68

(a) Breakthrough experiments

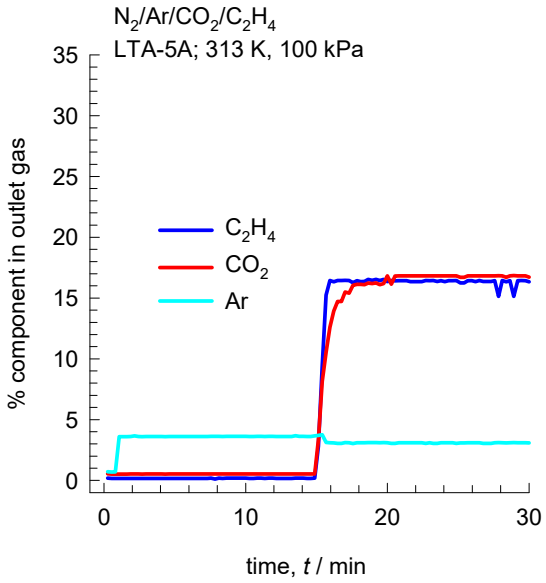

(b) Breakthrough simulations based on IAST

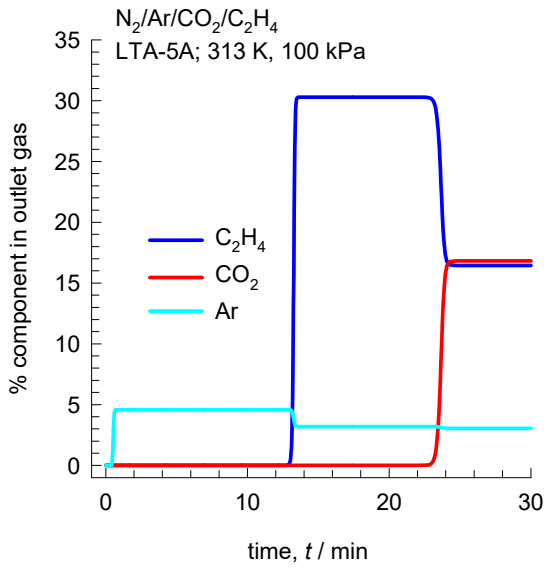

Figure S6. Run 2 at 1 bar.

Experimental transient breakthrough experiments vs simulations

T/ K	*P*/ bar	%Ar	%C_2H_4	%C_2H_6	%CO_2	%H_2	%H_2O	%CH_4	%CO	%N_2
313	1	2.63	14.10	0.00	19.98	0.00	0.00	0.00	0.00	63.29

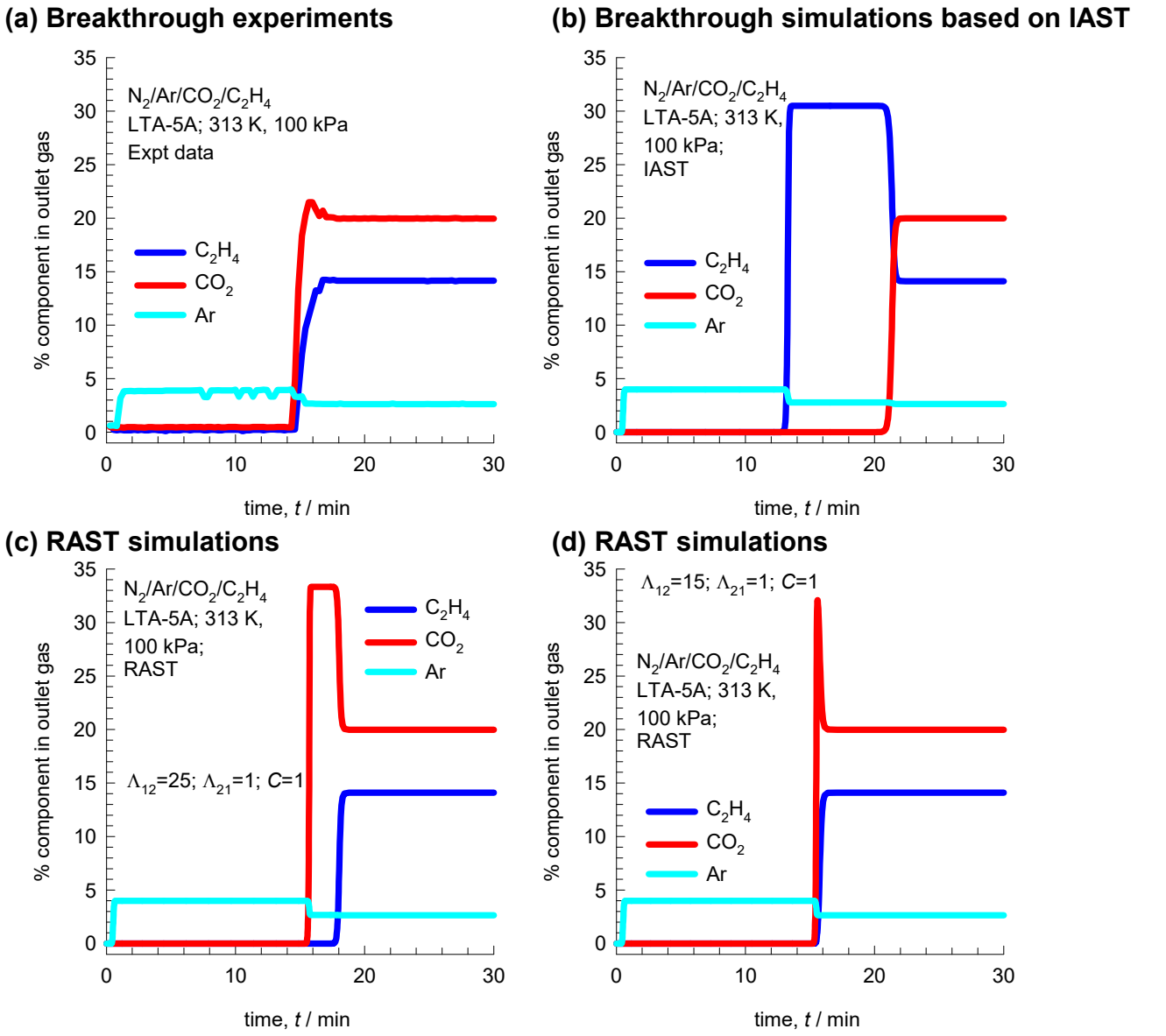

Figure S7. Run 3 at 1 bar.

T/ K	*P*/ bar	%Ar	%C_2H_4	%C_2H_6	%CO_2	%H_2	%H_2O	%CH_4	%CO	%N_2
313	1	2.95	17.81	0.00	10.20	0.00	0.00	0.00	0.00	69.05

(a) Breakthrough experiments

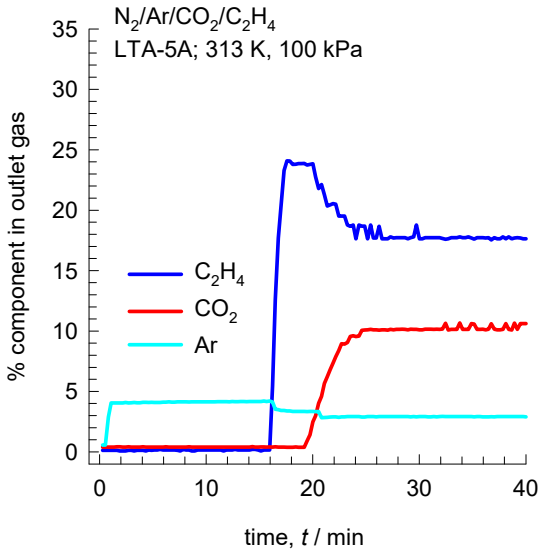

(b) Breakthrough simulations based on IAST

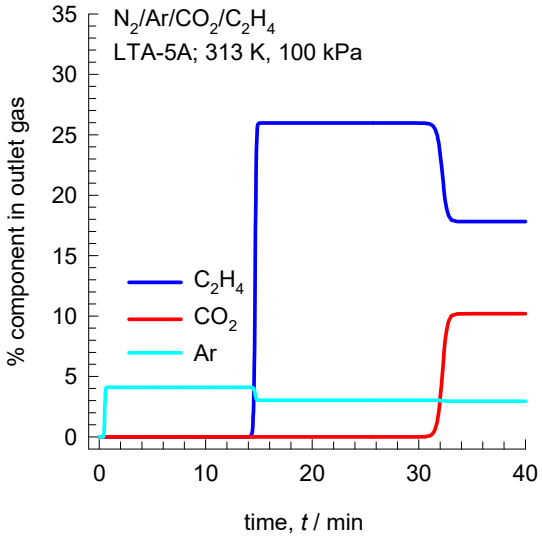

Figure S8. Run 4 at 1 bar.

Experimental transient breakthrough experiments vs simulations

T/ K	*P*/ bar	%Ar	%C_2H_4	%C_2H_6	%CO_2	%H_2	%H_2O	%CH_4	%CO	%N_2
313	1	3.59	19.14	0.00	6.06	0.00	0.00	0.00	0.00	71.21

(a) Breakthrough experiments

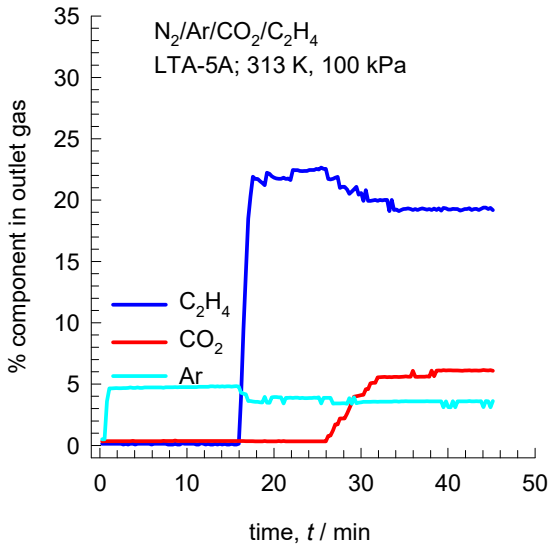

(b) Breakthrough simulations based on IAST

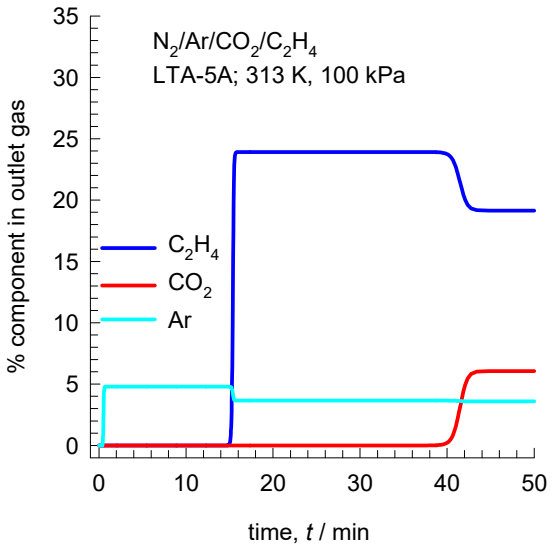

Figure S9. Run 5 at 1 bar.

Feed mixture composition

T/ K	*P*/ bar	%Ar	%C_2H_4	%C_2H_6	%CO_2	%H_2	%H_2O	%CH_4	%CO	%N_2
313	1	3.93	23.24	0	0	0	0	0	0	72.83

(a) Breakthrough experiments

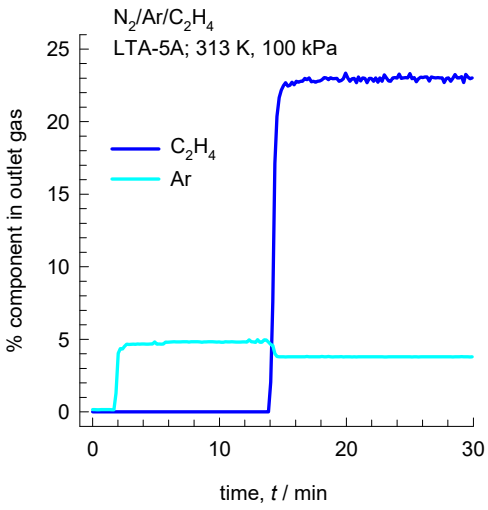

(b) Breakthrough simulations based on IAST

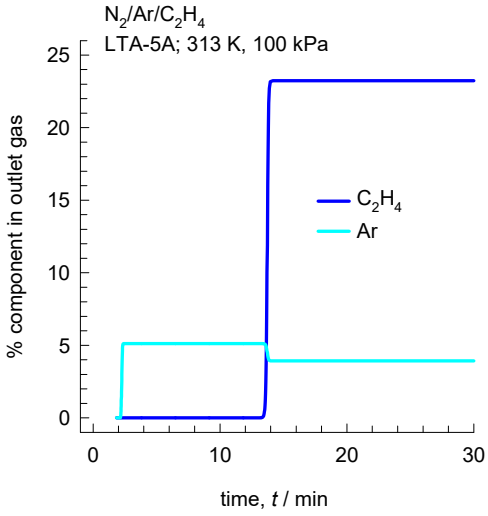

Figure S10. Run 6 at 1 bar.

Experimental transient breakthrough experiments vs simulations

T/ K	*P*/ bar	%Ar	%C_2H_4	%C_2H_6	%CO_2	%H_2	%H_2O	%CH_4	%CO	%N_2
313	1	3.15	19.01	0	8.25	0	0	0	0	69.59

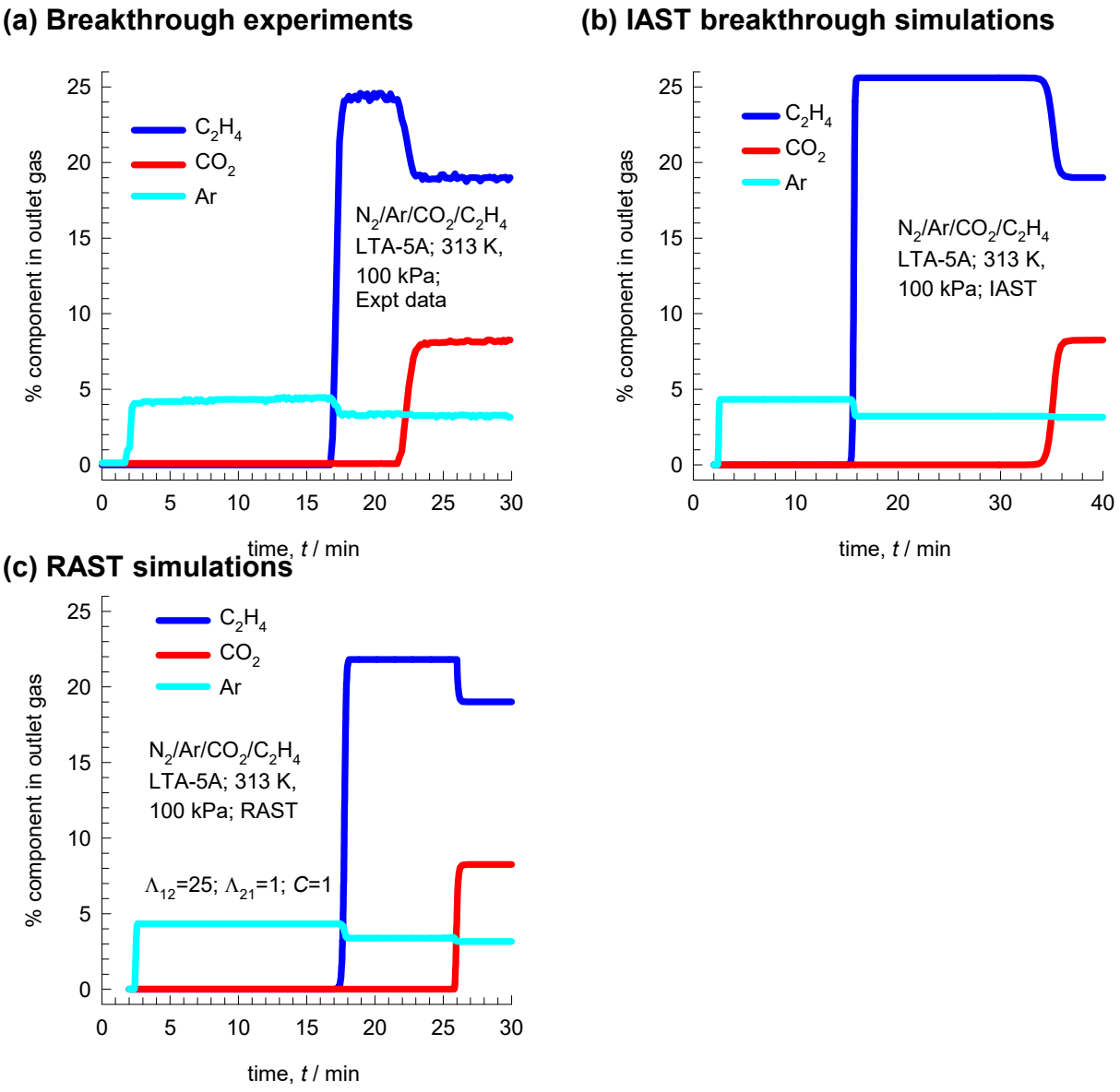

Figure S11. Run 7 at 1 bar.

T/ K	*P*/ bar	%Ar	%C_2H_4	%C_2H_6	%CO_2	%H_2	%H_2O	%CH_4	%CO	%N_2
313	1	1.93	11.81	0	8.56	13.17	0	0	7.75	56.78

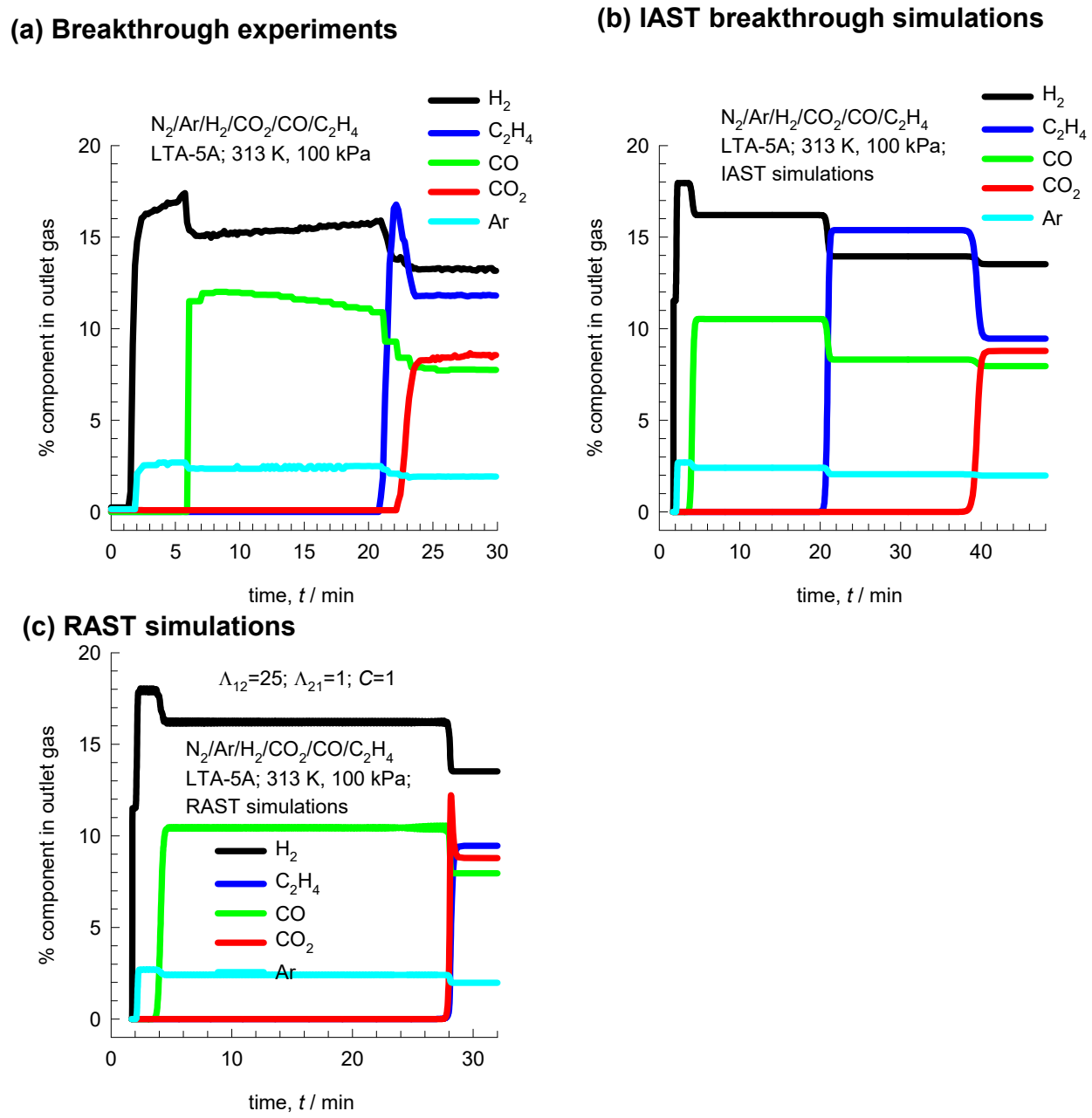

Figure S12. Run 8 at 1 bar.

Experimental transient breakthrough experiments vs simulations

T/ K	*P*/ bar	%Ar	%C_2H_4	%C_2H_6	%CO_2	%H_2	%H_2O	%CH_4	%CO	%N_2
313	1	3.39	6.97	6.76	7.24	0	0	6.37	0	69.28

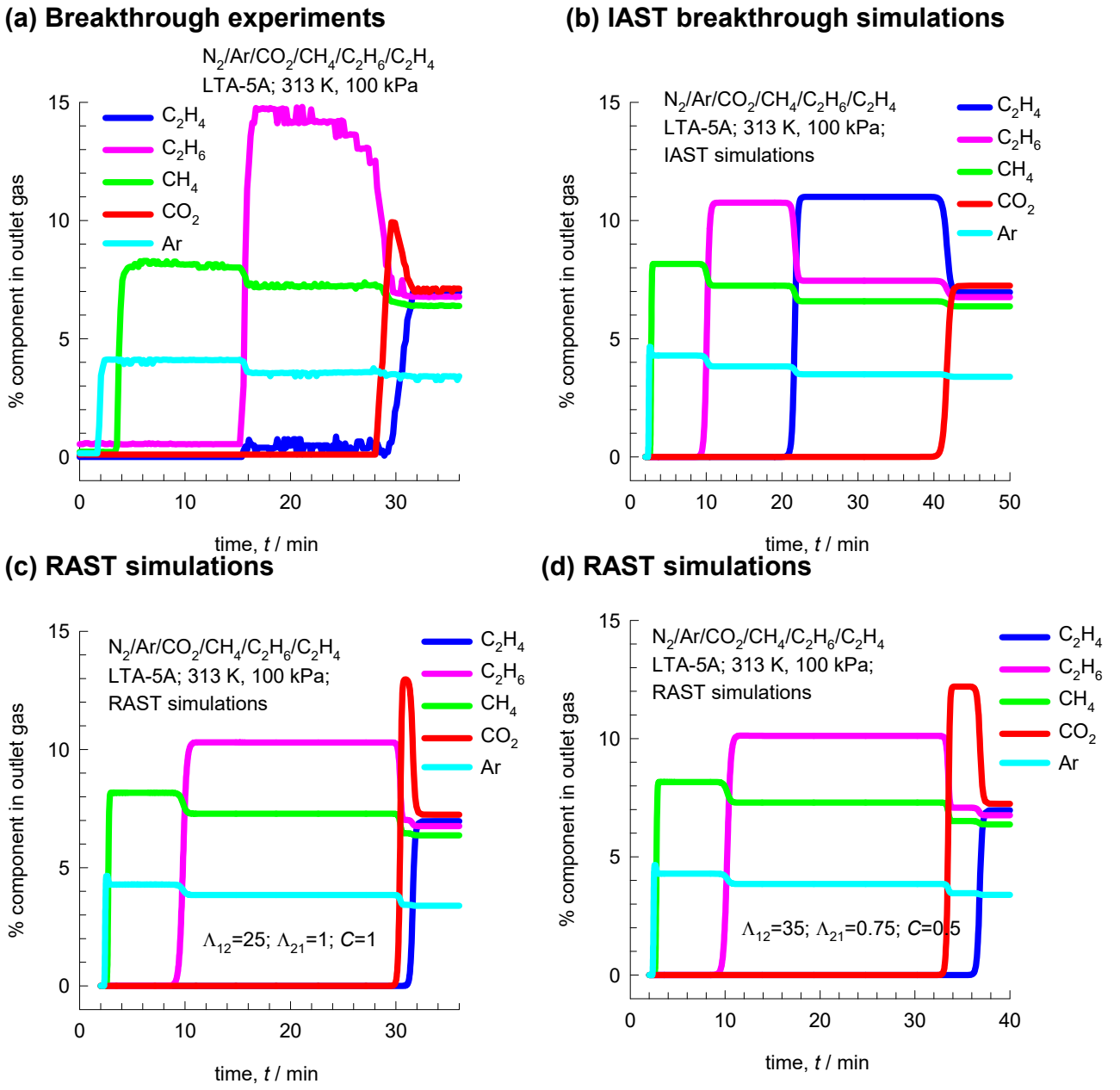

Figure S13. Run 9 at 1 bar.

T/ K	*P*/ bar	%Ar	%C_2H_4	%C_2H_6	%CO_2	%H_2	%H_2O	%CH_4	%CO	%N_2
313	1	1.98	4.06	3.98	8.51	13.74	0	3.82	0	63.91

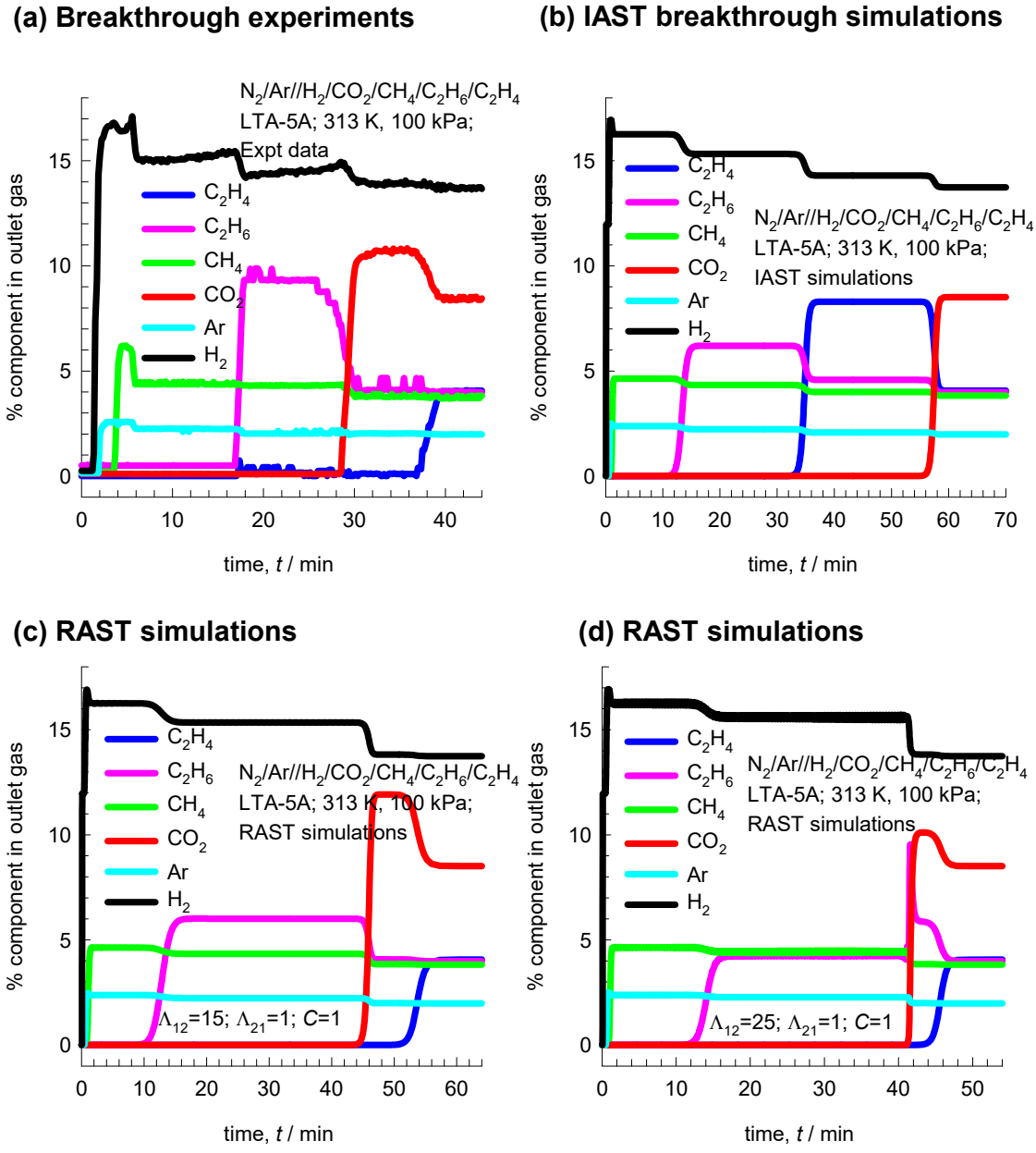

Figure S14. Run 10 at 1 bar.

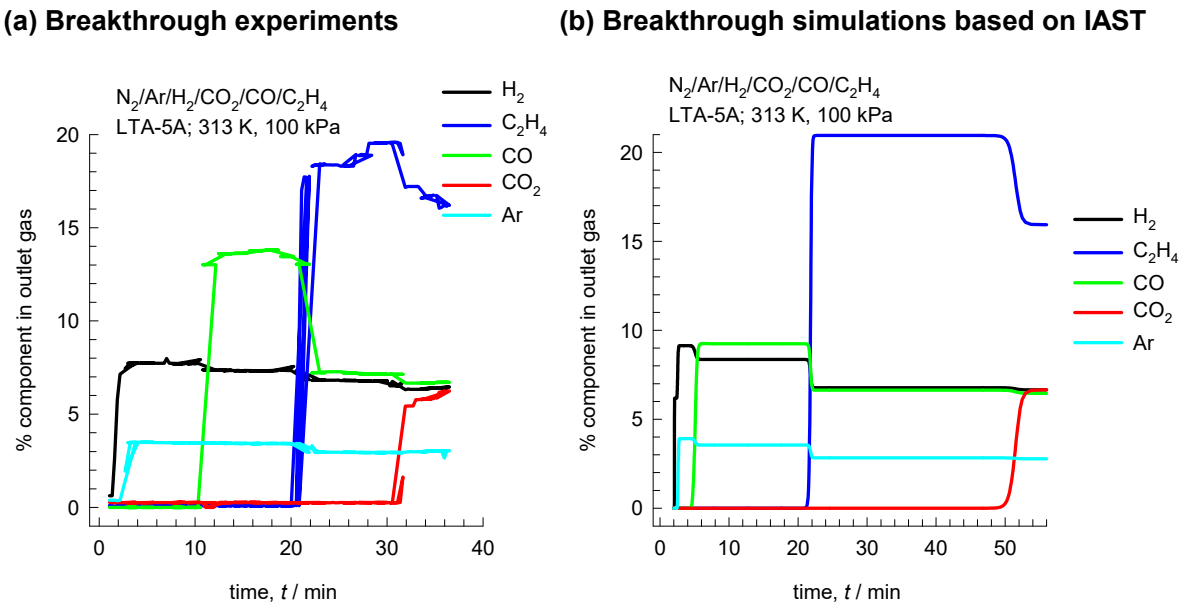

Figure S15. Run 11 at 1 bar.

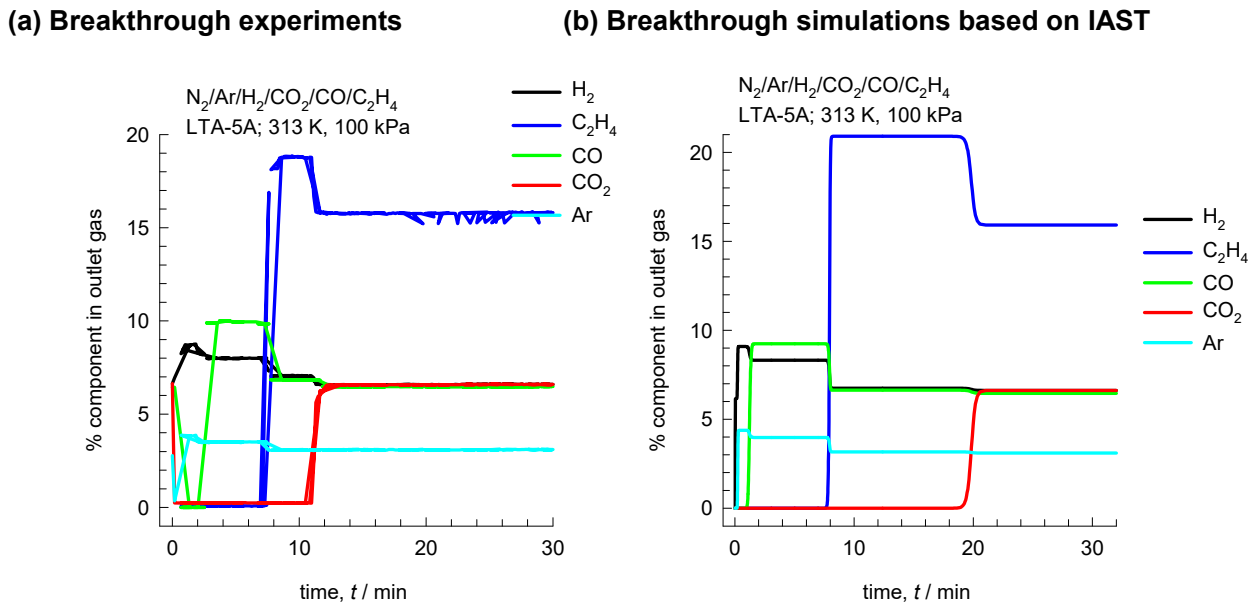

Figure S16. Run 12 at 1 bar.

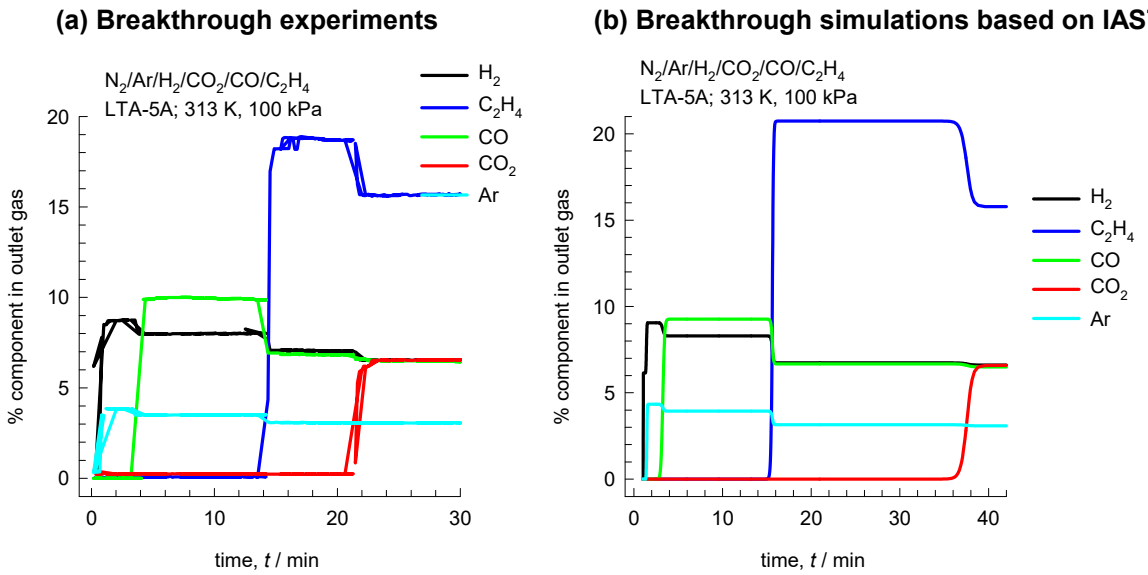

Figure S17. Run 13 at 1 bar.

T/ K	*P*/ bar	%Ar	%C_2H_4	%C_2H_6	%CO_2	%H_2	%H_2O	%CH_4	%CO	%N_2
313	6	3.92	22.25	0.00	0.00	0.00	0.00	0.00	0.00	73.83

(a) Breakthrough experiments

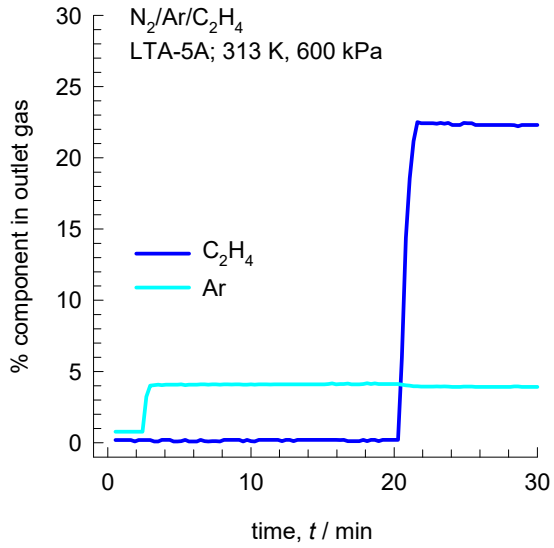

(b) Breakthrough simulations based on IAST

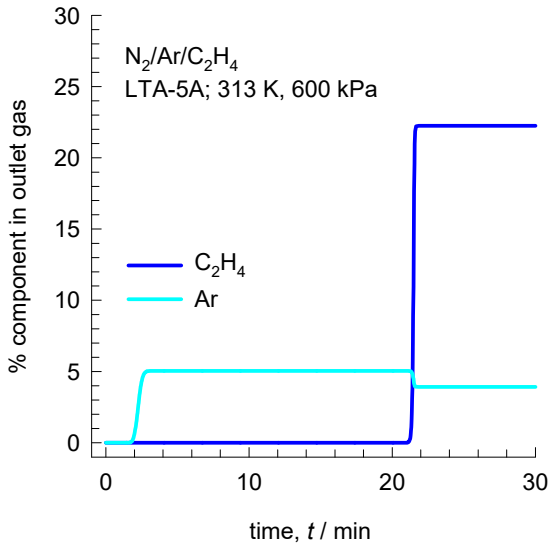

Figure S18. Run 14 at 6 bar.

Experimental transient breakthrough experiments vs simulations

T/ K	*P*/ bar	%Ar	%C_2H_4	%C_2H_6	%CO_2	%H_2	%H_2O	%CH_4	%CO	%N_2
313	6	3.01	16.02	0.00	17.11	0.00	0.00	0.00	0.00	63.86

(a) Breakthrough experiments **(b) Breakthrough simulations based on IAST**

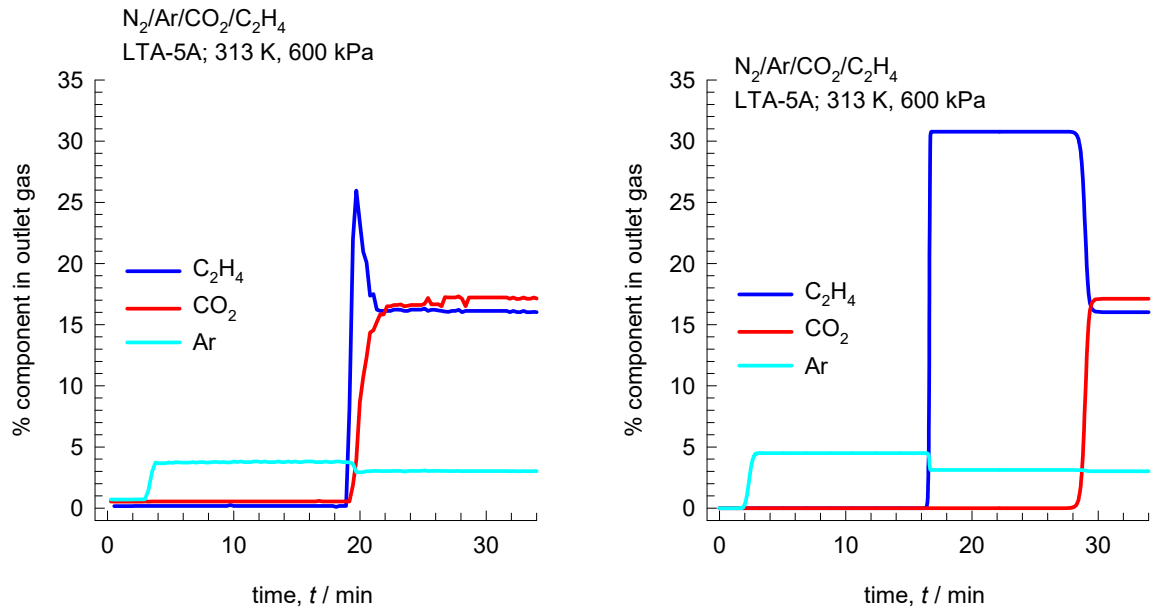

Figure S19. Run 15 at 6 bar.

Experimental transient breakthrough experiments vs simulations

T/ K	*P*/ bar	%Ar	%C_2H_4	%C_2H_6	%CO_2	%H_2	%H_2O	%CH_4	%CO	%N_2
313	6	2.54	13.70	0.00	19.88	0.00	0.00	0.00	0.00	63.87

(a) Breakthrough experiments

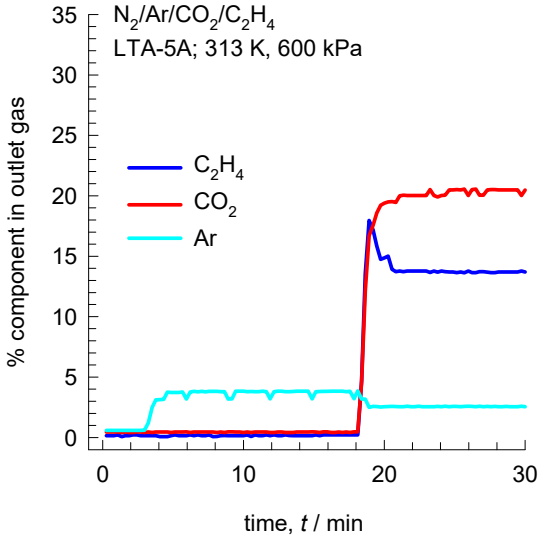

(b) Breakthrough simulations based on IAST

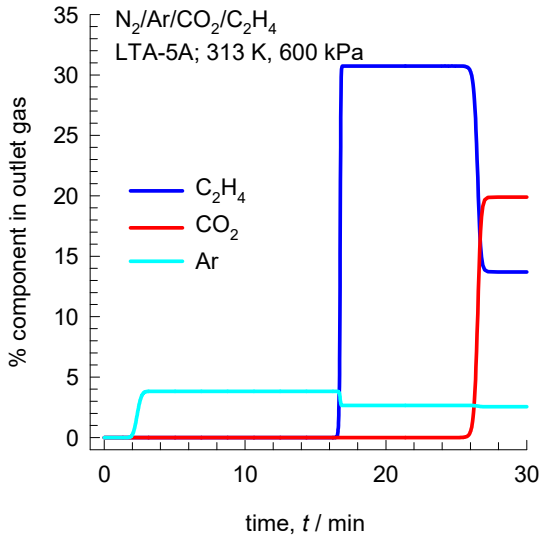

Figure S20. Run 16 at 6 bar.

Experimental transient breakthrough experiments vs simulations

T/ K	*P*/ bar	%Ar	%C_2H_4	%C_2H_6	%CO_2	%H_2	%H_2O	%CH_4	%CO	%N_2
313	6	2.81	17.98	0.00	10.21	0.00	0.00	0.00	0.00	69.00

(a) Breakthrough experiments

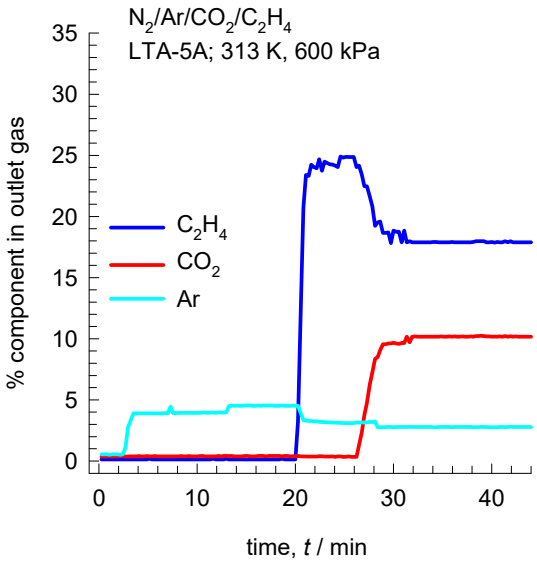

(b) Breakthrough simulations based on IAST

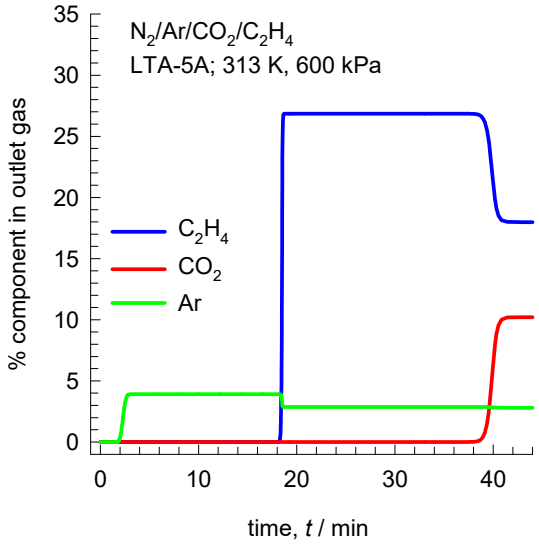

Figure S21. Run 17 at 6 bar.

T/ K	*P*/ bar	%Ar	%C_2H_4	%C_2H_6	%CO_2	%H_2	%H_2O	%CH_4	%CO	%N_2
313	6	3.50	19.39	0.00	5.43	0.00	0.00	0.00	0.00	71.69

(a) Breakthrough experiments

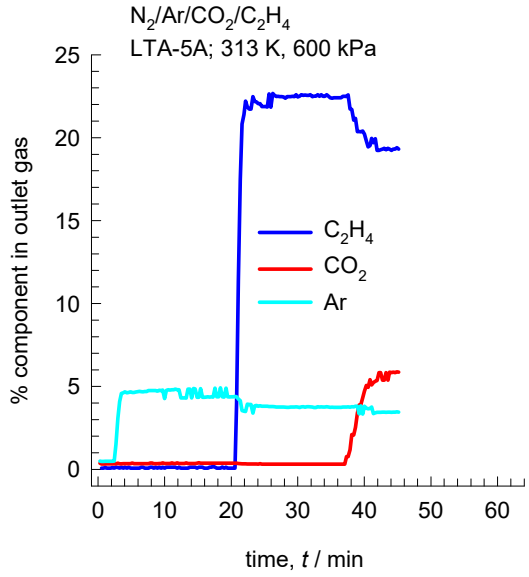

(b) Breakthrough simulations based on IAST

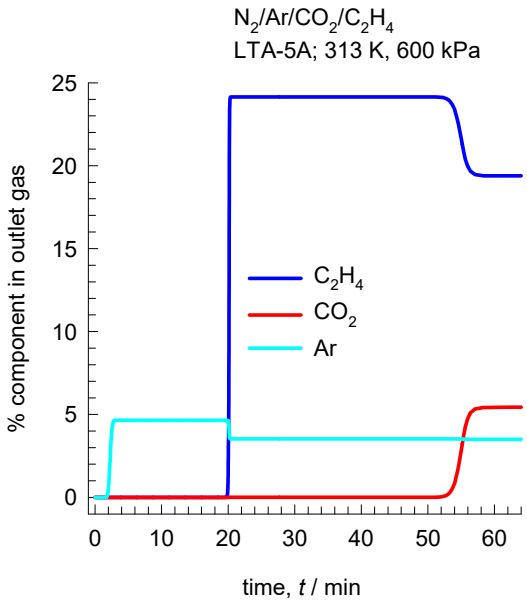

Figure S22. Run 18 at 6 bar.

Experimental transient breakthrough experiments vs simulations

T/ K	*P*/ bar	%Ar	%C_2H_4	%C_2H_6	%CO_2	%H_2	%H_2O	%CH_4	%CO	%N_2
313	6	4.97	15.55	4.88	18.04	0.1	0.05	5.01	4543	50.63

(a) Breakthrough experiments

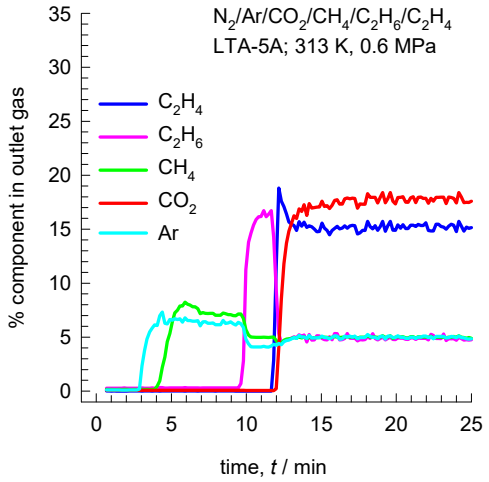

(b) Breakthrough simulations based on IAST

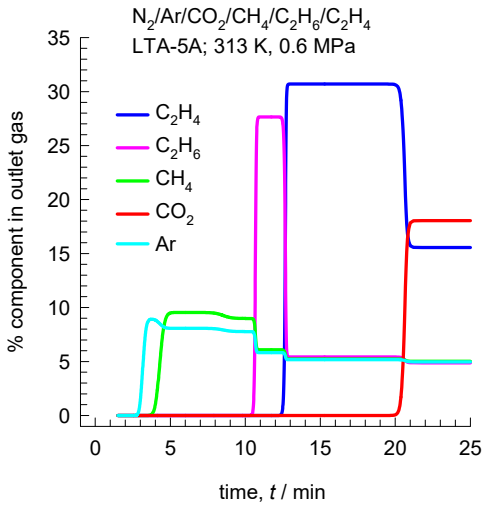

Figure S23. Run 19 at 6 bar.

Experimental transient breakthrough experiments vs simulations

T/ K	*P*/ bar	%Ar	%C_2H_4	%C_2H_6	%CO_2	%H_2	%H_2O	%CH_4	%CO	%N_2
313	6	3.86	11.41	3.66	12.86	24.84	0.04	3.61	0.5	39.24

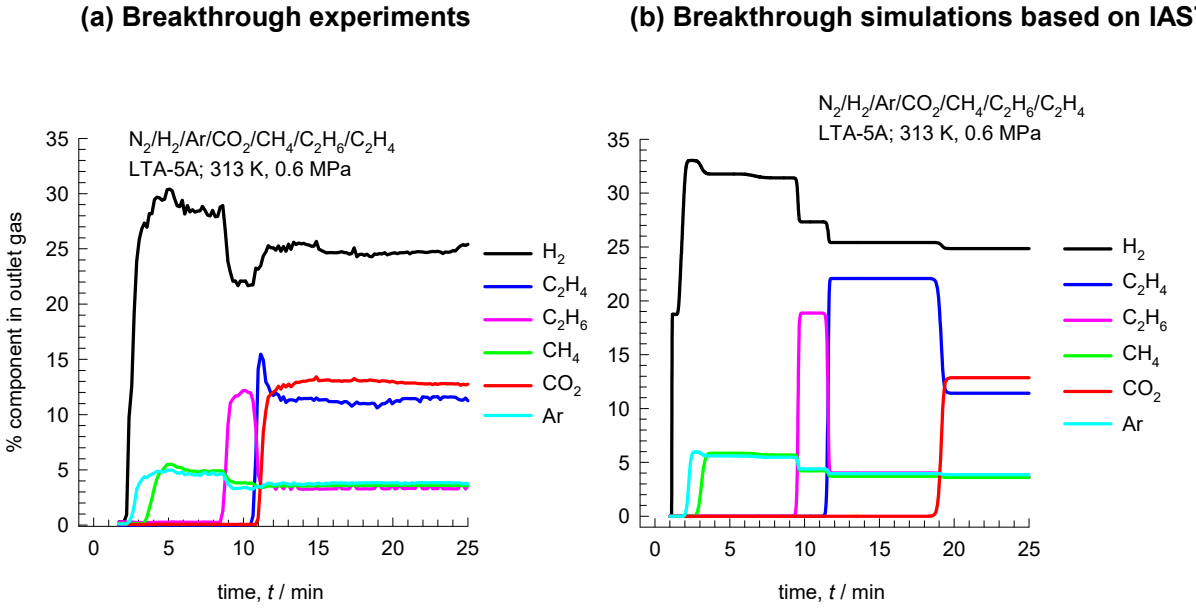

Figure S24. Run 20 at 6 bar.

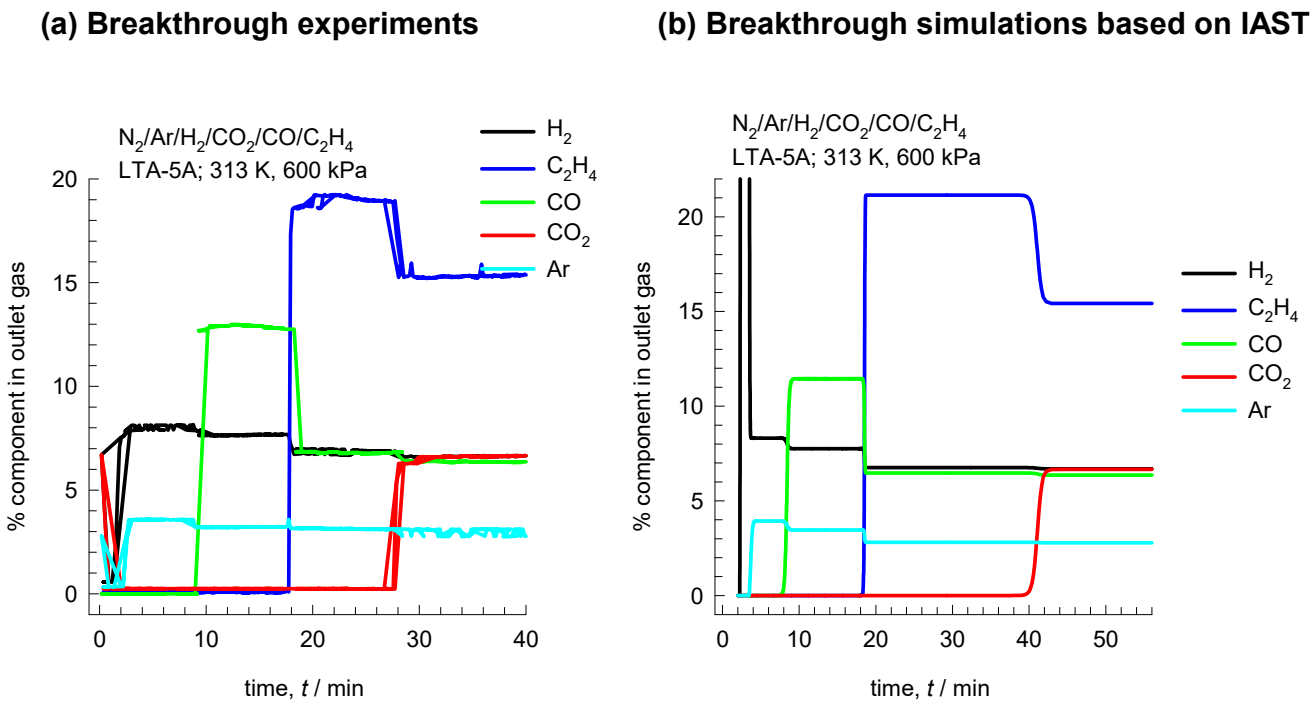

Figure S25. Run 21 at 6 bar.

Experimental transient breakthrough experiments vs simulations

T/ K	*P*/ bar	%Ar	%C_2H_4	%C_2H_6	%CO_2	%H_2	%H_2O	%CH_4	%CO	%N_2
313	11	3.66	20.82	0.00	0.00	0.00	0.00	0.00	0.00	75.53

(a) Breakthrough experiments **(b) Breakthrough simulations based on IAST**

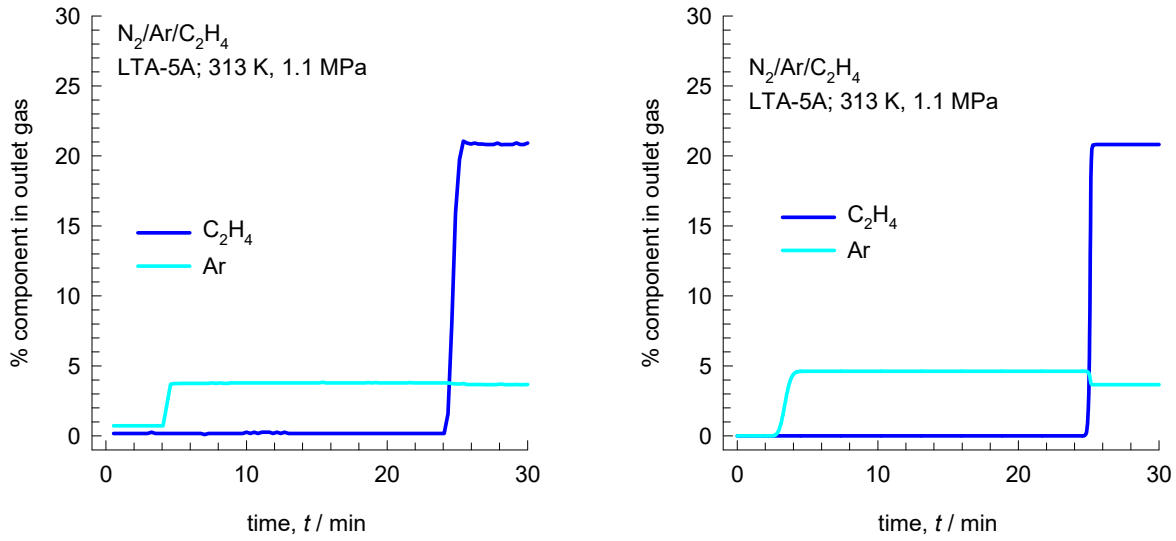

Figure S26. Run 22 at 11 bar.

Experimental transient breakthrough experiments vs simulations

T/ K	*P*/ bar	%Ar	%C_2H_4	%C_2H_6	%CO_2	%H_2	%H_2O	%CH_4	%CO	%N_2
313	11	2.70	14.50	0.00	17.44	0.00	0.00	0.00	0.00	65.35

(a) Breakthrough experiments

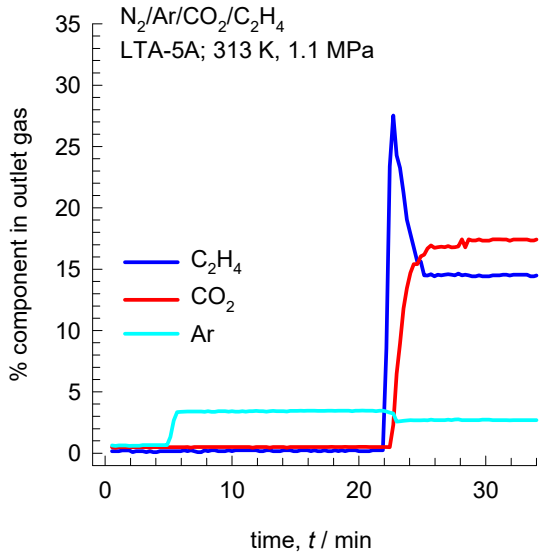

(b) Breakthrough simulations based on IAST

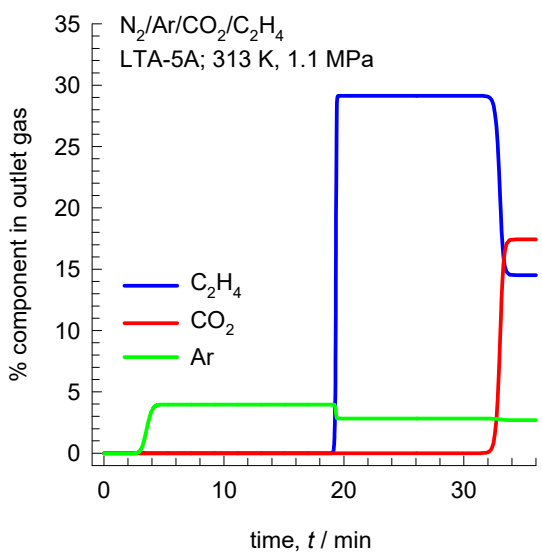

Figure S27. Run 23 at 11 bar.

Experimental transient breakthrough experiments vs simulations

T/ K	*P*/ bar	%Ar	%C_2H_4	%C_2H_6	%CO_2	%H_2	%H_2O	%CH_4	%CO	%N_2
313	11	2.47	14.46	0.00	19.37	0.00	0.00	0.00	0.00	63.69

(a) Breakthrough experiments

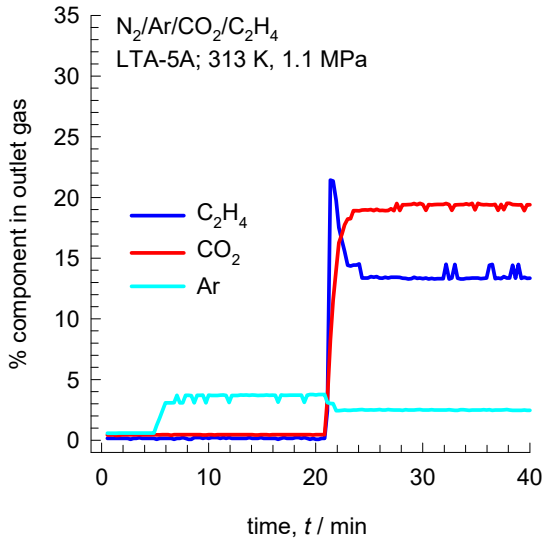

(b) Breakthrough simulations based on IAST

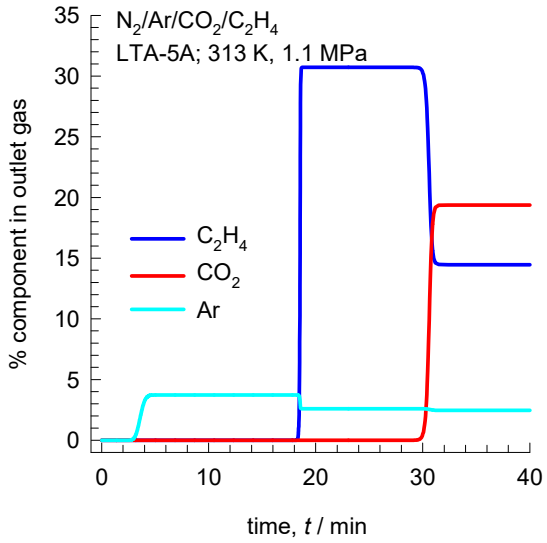

Figure S28. Run 24 at 11 bar.

T/ K	*P*/ bar	%Ar	%C_2H_4	%C_2H_6	%CO_2	%H_2	%H_2O	%CH_4	%CO	%N_2
313	11	2.74	17.57	0.00	9.98	0.00	0.00	0.00	0.00	69.71

(a) Breakthrough experiments

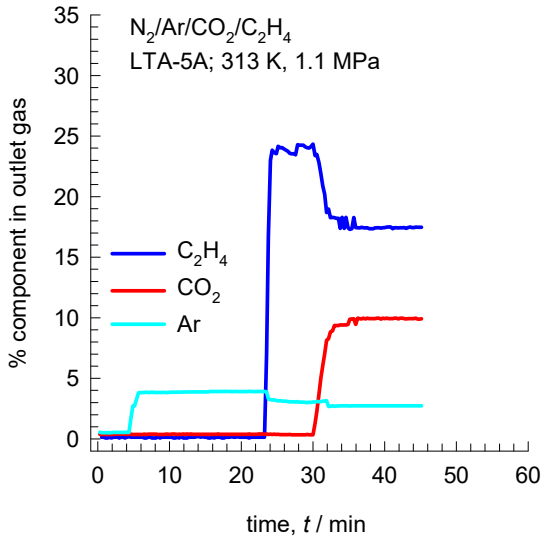

(b) Breakthrough simulations based on IAST

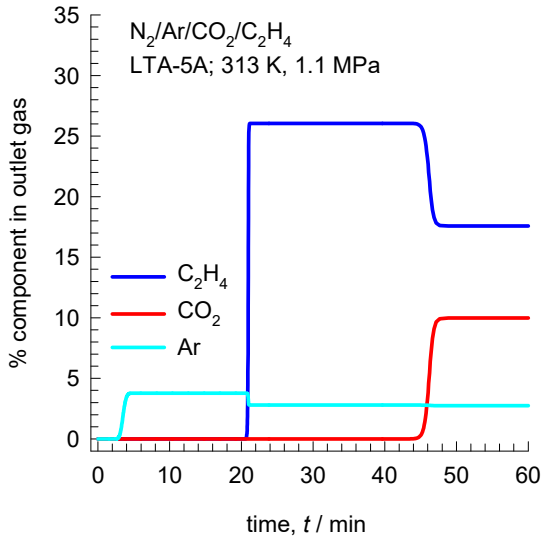

Figure S29. Run 25 at 11 bar.

Experimental transient breakthrough experiments vs simulations

T/ K	*P*/ bar	%Ar	%C_2H_4	%C_2H_6	%CO_2	%H_2	%H_2O	%CH_4	%CO	%N_2
313	11	3.28	19.29	0.00	5.12	0.00	0.00	0.00	0.00	72.31

(a) Breakthrough experiments

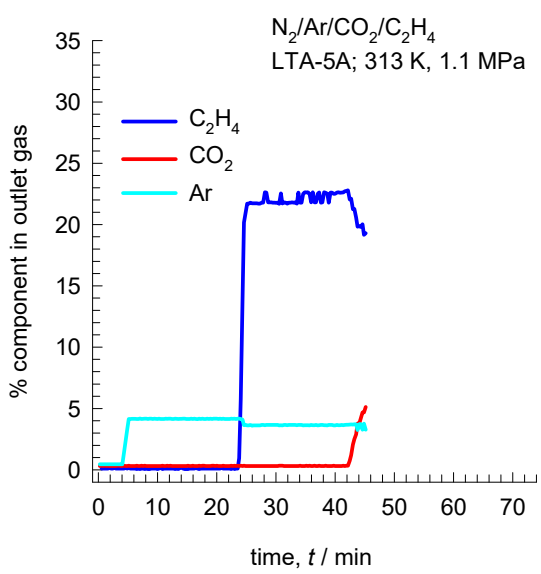

(b) Breakthrough simulations based on IAST

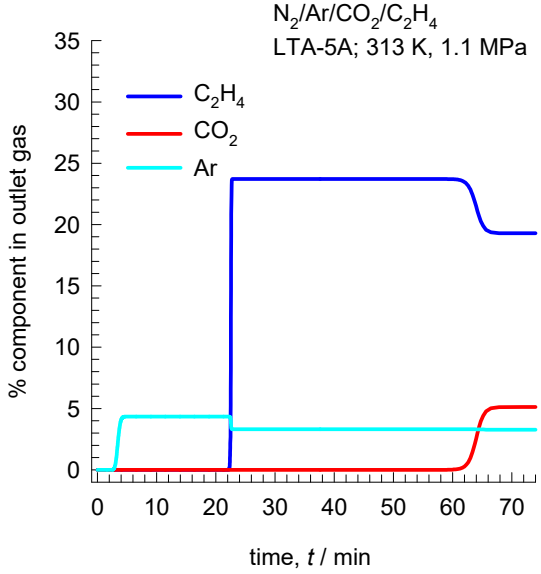

Figure S30. Run 26 at 11 bar.

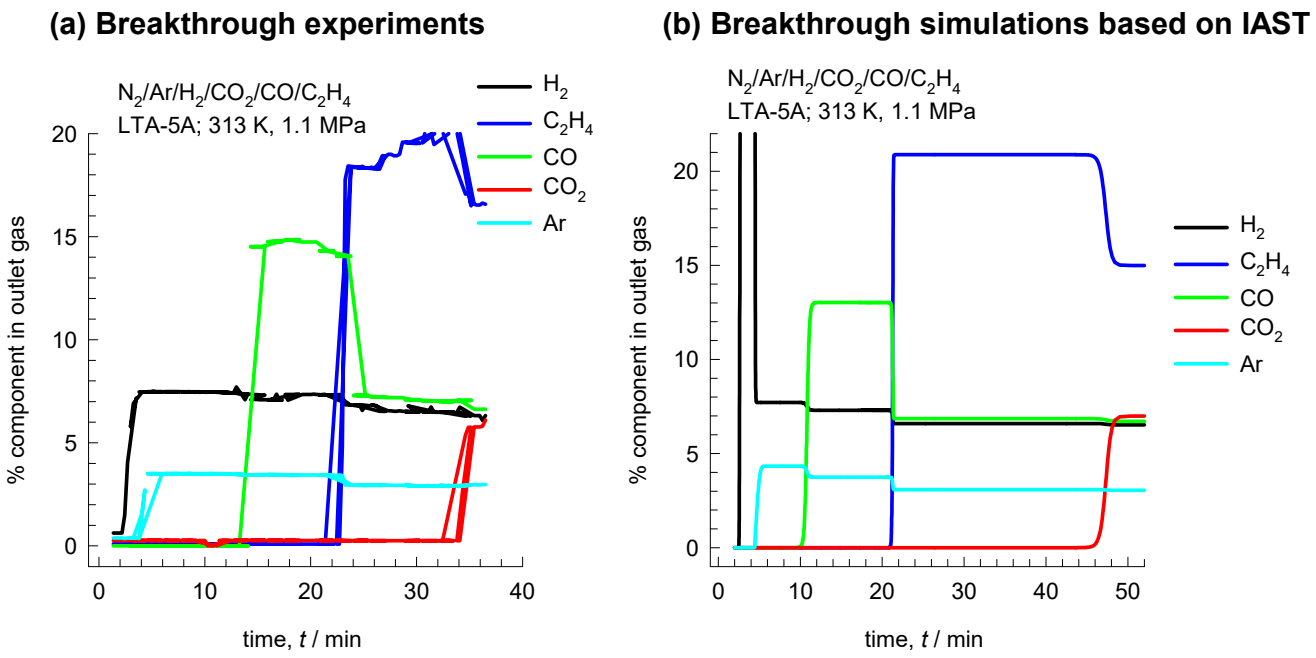

Figure S31. Run 27 at 11 bar.

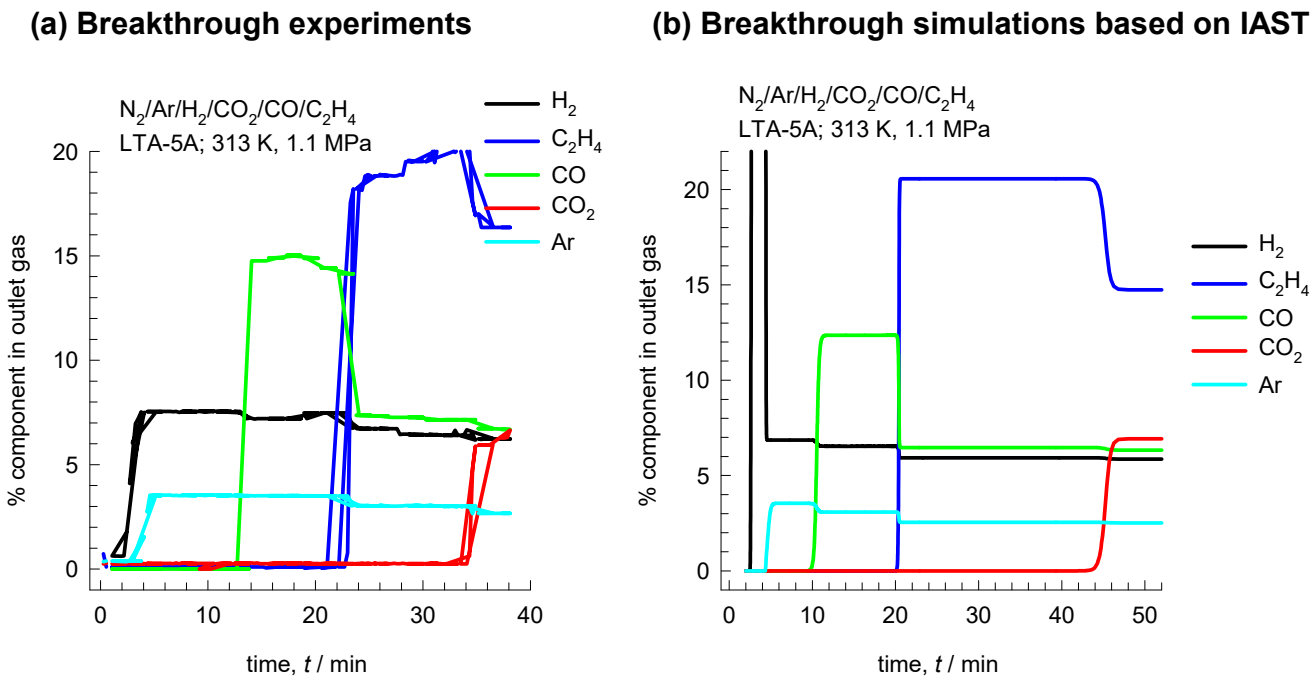

Figure S32. Run 28 at 11 bar.

8 Non-idealities in C_2H_4/CO_2 mixture adsorption

8.1 Analysis of Calleja data for C_2H_4/CO_2 mixture adsorption in 5A zeolite

The paper by Calleja et al.[26] presents convincing evidence of strong non-idealities for adsorption of $C_2H_4(1)/CO_2(2)$ mixtures in LTA-5A zeolite. Their experimental data, obtained at 293 K and total pressure of 10 bar as presented in Figure 3 of their paper has been redrawn for further analysis and discussion in Figure S33.

The Calleja et al.[26] data clearly demonstrate the phenomenon of azeotropic adsorption, $y_1 = x_1;\quad y_2 = x_2$, and selectivity reversals at $y_1 < 0.4$. The experimental data are well represented by the Real Adsorbed Solution Theory (RAST) with the choice of the Wilson parameters $\Lambda_{12} = 35;\quad \Lambda_{21} = 0.75;\quad C = 0.5$.

8.2 Analysis of non-idealities in the transient breakthrough experiments

We now analyze the transient breakthrough experiments to demonstrate remarkable similarities with the Calleja et al.[26] data. Using the shock-wave model for fixed-bed adsorbers,[10] we can determine the adsorbed phase loadings of $C_2H_4(1)$, and $CO_2(2)$ for each of the experimental campaigns.

We illustrate the application of the shock-wave model for Run 4 at 1 bar total pressure; see Figure S8, The mole fractions of the four components in the feed gas mixture are

C_2H_4: $y_{f1} = 0.178$; CO_2: $y_{f2} = 0.102$; Ar: $y_{f3} = 0.0295$; N_2: $y_{f4} = 0.6905$

The breakthrough times for $C_2H_4(1)$, and $CO_2(2)$ are $t_1 = 16.22$ min; and $t_2 = 19.47$ min

If the total molar flow rate of the gas mixture is Q mol min^{-1}, and the mass of adsorbent 5A is m_{ads} kg, we can calculate the molar loading of $CO_2(2)$ in the adsorbed phase at final equilibrium:

$$q_2 = \frac{Q}{m_{ads}} y_{f2} t_2 \tag{S28}$$

The molar loading of $C_2H_4(1)$ in the adsorbed phase at final equilibrium is

$$q_1 = \frac{Q}{m_{ads}}\left[y_{f1} t_2 - \left(1 - y_{f3} - y_{f4}\right)\left(t_2 - t_1\right)\right] \tag{S29}$$

The second term on the right member of equation (S29) is the amount of $C_2H_4(1)$, of composition $\left(1 - y_{f3} - y_{f4}\right)$ that is purged during the time interval $\left(t_2 - t_1\right)$.

For comparison with the data in Figure S33 we determine the adsorbed phase mole fractions of $C_2H_4(1)$, and $CO_2(2)$ for a pseudo-binary adsorbed phase mixture; the adsorbed phase mole fractions are

$$x_1 = \frac{q_1}{q_1 + q_2}; \quad x_2 = \frac{q_2}{q_1 + q_2} \tag{S30}$$

The corresponding mole fractions of $C_2H_4(1)$, and $CO_2(2)$ in the pseudo-binary bulk feed mixture are

$$y_1 = \frac{y_{f1}}{1 - y_{f3} - y_{f4}}; \quad y_2 = \frac{y_{f2}}{1 - y_{f3} - y_{f4}} \tag{S31}$$

For the transient breakthrough experiments in Run 10 at 1 bar total pressure (see Figure S14), the component to breakthrough last is C_2H_4. The mole fractions of the components in the feed mixture are

C_2H_4: $y_{f1} = 0.0406$; CO_2: $y_{f2} = 0.0851$; Ar: $y_{f3} = 0.0198$; N_2: $y_{f4} = 0.6391$; CH_4: $y_{f5} = 0.0382$;

C_2H_6: $y_{f6} = 0.0398$; H_2: $y_{f7} = 0.1374$;

The breakthrough times for $C_2H_4(1)$, and $CO_2(2)$ are $t_1 = 37$ min; and $t_2 = 28.5$ min

If the total molar flow rate of the gas mixture is Q mol min^{-1}, and the mass of adsorbent 5A is m_{ads} kg, we can calculate the molar loading of $C_2H_4(1)$ in the adsorbed phase at final equilibrium:

$$q_1 = \frac{Q}{m_{ads}} y_{f1} t_1 \tag{S32}$$

The molar loading of $CO_2(2)$ in the adsorbed phase at final equilibrium is

$$q_2 = \frac{Q}{m_{ads}}\left[y_{f2} t_2 - \left(1 - y_{f3} - y_{f4} - y_{f5} - y_{f6} - y_{f7}\right)\left(t_2 - t_1\right)\right] \tag{S33}$$

The second term on the right member of equation (S33) is the amount of $CO_2(1)$, of composition $\left(1 - y_{f3} - y_{f4} - y_{f5} - y_{f6} - y_{f7}\right)$ that is purged during the time interval $\left(t_2 - t_1\right)$.

For comparison with the data in Figure S33 we determine the adsorbed phase mole fractions of C_2H_4(1), and CO_2(2) for a pseudo-binary adsorbed phase mixture; the adsorbed phase mole fractions are

$$x_1 = \frac{q_1}{q_1 + q_2}; \quad x_2 = \frac{q_2}{q_1 + q_2} \tag{S34}$$

The corresponding mole fractions of C_2H_4(1), and CO_2(2) in the pseudo-binary bulk feed mixture are

$$y_1 = \frac{y_{f1}}{\left(1 - y_{f3} - y_{f4} - y_{f5} - y_{f6} - y_{f7}\right)}; \quad y_2 = \frac{y_{f2}}{\left(1 - y_{f3} - y_{f4} - y_{f5} - y_{f6} - y_{f7}\right)} \tag{S35}$$

All of the 28 experimental breakthrough experiments were analyzed using the shock-wave model, using the foregoing set of equations. The calculated data are summarized in Table S8, Table S9, and Table S10 The plots of the adsorbed phase mole of C_2H_4(1), x_1, in the adsorbed phase vs the bulk gas phase mole fraction of C_2H_4(1), y_1 are shown in Figure S34a. The strong deviations of the experimental x_1 vs y_1 data from the IAST can be adequately captured by the RAST model with the Wilson parameters: $\Lambda_{12} = 25; \quad \Lambda_{21} = 1; \quad C = 1$. The departures of the experimental data from the IAST predictions are the highest for any data on binary mixture adsorption.[24, 25] Figure S34b compares the RAST calculations for two sets of Wilson parameters: $\Lambda_{12} = 25; \quad \Lambda_{21} = 1; \quad C = 1$, and $\Lambda_{12} = 15; \quad \Lambda_{21} = 1; \quad C = 1$. The entire set of experimental data lie within the bounds of these two parameters

For $y_1 < 0.5$, the selectivity is in favor of C_2H_4. This implies that for selective adsorption of ethylene from CO_2-bearing mixtures is feasible provided the C_2H_4/CO_2 ratio in the feed mixture is lower than unity.

Transient breakthrough simulations using the RAST description of mixture adsorption captures the selectivity reversal adequately for Run 3, Run 9, and Run 10; see Figure S7(c,d), Figure S13(c,d), and Figure S14(c,d)

8.3 List of Figures for Non-idealities in C2H4/CO2 mixture adsorption

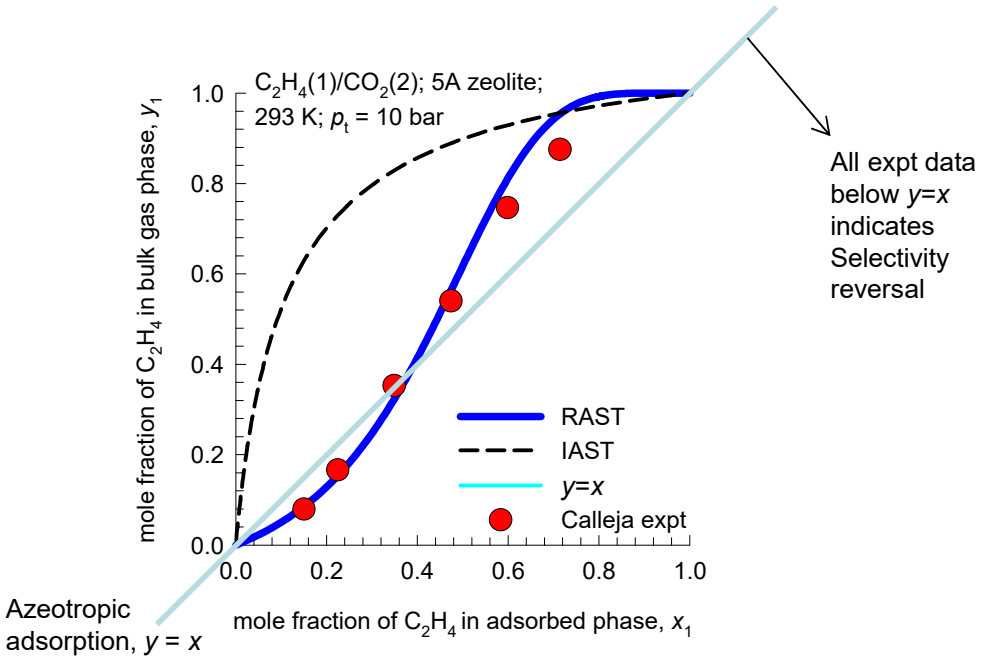

Figure S33. Experimental data, obtained at 293 K and total pressure of 10 bar, for adsorption of $C_2H_4(1)/CO_2(2)$ mixtures in LTA-5A zeolite; the mole fraction of C_2H_4 in the bulk gas phase mixture, y_1, is plotted as a function of the adsorbed phase mole fraction of C_2H_4, x_1.. The data are redrawn from Figure 3 of Calleja et al.[26] Also indicated at the IAST and RAST calculations of mixture adsorption equilibrium.

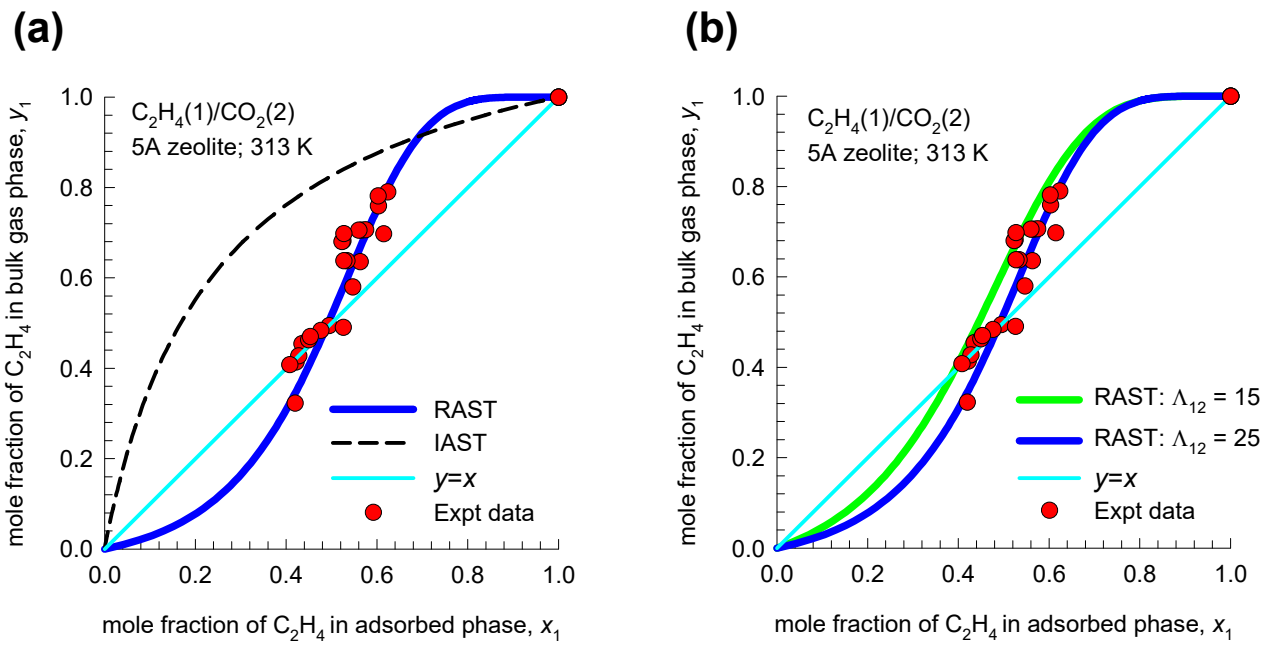

Figure S34. Experimental data for adsorption of pseudo-binary $C_2H_4(1)/CO_2(2)$ mixtures in LTA-5A zeolite at 313 K; the mole fraction of C_2H_4 in the bulk gas phase mixture, y_1, is plotted as a function of the adsorbed phase mole fraction of C_2H_4, x_1. The plotted data are based on the 28 experimental campaigns on transient experimental breakthrough, and use of the shock-wave model. The IAST and RAST model calculations are for p_t = 2 bar which is the average of the total of partial pressures of $C_2H_4(1)$ and $CO_2(2)$ in all of the 28 experimental campaigns. Two different sets of Wilson parameters are in the RAST calculations in (b).

9 Analysis of the experimental data of García et al.

Further experimental evidence of selectivity reversals in favor of C_2H_4 for feed mixtures with C_2H_4/CO_2 lower than unity are provided in the experiments reported by García et al.[27]

Figure S35(a,b,c,d) show experimental data for transient breakthroughs of CH_4/N_2, C_2H_6/N_2, C_2H_4/N_2, and CO_2/N_2 mixtures in a fixed bed packed with LTA-5A zeolite at four different operating conditions, as reported in Figure 3 of García et al.[27] For all these mixtures, thermodynamic non-idealities are not important and the hierarchy of breakthrough times are $CH_4 < C_2H_6 < C_2H_4 < CO_2$, reflecting the stronger adsorption strength of CO_2 compared to C_2H_4 for unary adsorption.

Figure S36(a,b) show experimental data for transient breakthroughs of 20/80 C_2H_4/CO_2 mixtures at 303 K and 363 K, as reported in Figure 5 of García et al.[27] The data indicate selectivity reversal in favor of C_2H_4, contrary to the expectations that are raised by the data in Figure S35(a,b,c,d).

Figure S37(a,b,c,d) show experimental data for breakthroughs 40/4/49/7 $CH_4/C_2H_6/CO_2/C_2H_4$ mixtures at four different operating conditions, as reported in Figure 7 of García et al.[27] In all cases, the breakthrough of C_2H_4 at a later time than that of CO_2, signifying selectivity reversals in favor of the unsaturated alkene.

In order to quantify the non-idealities in Figure S36, and Figure S37, all of the 6 experimental breakthrough experiments were analyzed using the shock-wave model. The unary isotherm data fits are provided in Table S1, Table S2, Table S3, and Table S4.The plots of the adsorbed phase mole of $C_2H_4(1)$, x_1, in the adsorbed phase vs the bulk gas phase mole fraction of $C_2H_4(1)$, y_1 are shown in Figure S38(a,b) for the pseudo-binary $C_2H_4(1)/CO_2(2)$ mixture. The deviations from the IAST can be adequately captured by the RAST model with the Wilson parameters: $\Lambda_{12} = 15; \quad \Lambda_{21} = 1; \quad C = 1$ for operation at 303 K. The non-ideality effects at 363 K are significantly lower, and can be captured using the Wilson parameters: $\Lambda_{12} = 2; \quad \Lambda_{21} = 1; \quad C = 1$.

We now compare the experimental breakthroughs, as reported in Figures 3, 5, 6, and 7 of García et al.[27] with transient breakthrough simulations using the methodology described in Chapter 5. In the

breakthrough simulations, non-ideality effects are applied only for the binary C_2H_4/CO_2 pair in the mixture; all other binary pairs are assumed to be ideal. In all of the transient breakthrough experiments reported by García et al.,[27] the transient breakthroughs have distended characteristics; this indicates that intra-crystalline diffusion influences are not entirely negligible. Consequently, in the transient breakthrough simulations reported here-under, we take $\frac{Đ_i}{r_c^2} = 0.001$ for each individual guest molecule, for operations at both 303 K and 363 K. The adsorber dimensions, and interstitial gas velocities are chosen to match the experimental conditions in each case. For the simulations of transient breakthroughs, the unary isotherm data fits are provided in Table S1, Table S2, Table S3, and Table S4.

Indeed, transient breakthrough simulations invoking the IAST or RAST, as appropriate, for calculation of mixture adsorption equilibrium are able to match the experimentally observed breakthroughs for all of the experiments as reported in Figures 3, 5, 6, and 7 of García et al.[27]

Figure S39(a,b) compare experimental data on transient breakthroughs with breakthrough simulations of 20/80 mixtures: CH_4/N_2, C_2H_6/N_2, C_2H_4/N_2, and CO_2/N_2 mixtures. The experimental breakthroughs are well matched by simulations for these mixtures, for which the IAST is used for describing mixture adsorption equilibrium.

Figure S40 compares experimental data for breakthroughs of (a) 20/80 C_2H_6/CO_2, (b) 20/80 CH_4/CO_2, (c) 20/80 C_2H_6/C_2H_4, (d) 20/80 C_2H_4/CH_4, (e) 20/80 C_2H_6/CH_4, and (f) 20/80 C_2H_4/CO_2 mixtures in a fixed bed packed with LTA-5A zeolite operating at 303 K and p_t = 6 bar. The breakthrough simulations using the IAST are of good accuracy in (a), (b), (c), (d), and (e). The use of IAST is unable to anticipate the selectivity reversal for 20/80 C_2H_4/CO_2 mixtures.

Use of the RAST for describing mixture adsorption equilibrium provides a very good match with experimental breakthroughs for 20/80 C_2H_4/CO_2 mixtures, at both 303 K, and 363 K; see Figure S41(b,d). The selectivity reversal phenomena are well described by the RAST model. For the breakthrough simulations at 303 K, the RAST model uses the Wilson parameters: $\Lambda_{12} = 15; \quad \Lambda_{21} = 1; \quad C = 1$. For describing the non-ideality effects at 363 K we use the Wilson

parameters: $\Lambda_{12} = 2; \quad \Lambda_{21} \equiv 1; \quad C = 1$. The choice of the Wilson parameters are based on the analysis presented in Figure S38

Figure S42 compares the experimental data for breakthroughs of 56/7/23/14 $CH_4/C_2H_6/N_2/C_2H_4$ mixtures with breakthrough simulations using IAST for mixture adsorption equilibrium. The breakthrough simulations are in good agreement with experimental data for this mixture that does not display non-idealities in view of the absence of CO_2.

Figure S43 compares the experimental breakthroughs with simulations of 40/4/49/7 $CH_4/C_2H_6/CO_2/C_2H_4$ mixtures operating at 303 K. Use of the IAST fails to anticipate the CO_2/C_2H_4 selectivity reversals; see Figure S43(a, b). Use of the RAST with Wilson parameters $\Lambda_{11} = 15; \quad \Lambda_{22} = 1; \quad C = 1$ is able to match the experimental breakthroughs nearly quantitatively; see Figure S43(c, d).

Figure S44 compares the experimental breakthroughs with simulations of 40/4/49/7 $CH_4/C_2H_6/CO_2/C_2H_4$ mixtures operating at 363 K. Use of the IAST fails to anticipate the CO_2/C_2H_4 selectivity reversals; see Figure S44(a, b). Use of the RAST with Wilson parameters $\Lambda_{11} = 2; \quad \Lambda_{22} = 1; \quad C = 1$ is able to match the experimental breakthroughs nearly quantitatively; see Figure S44(c, d).

9.1 List of Figures for Analysis of the experimental data of García et al.

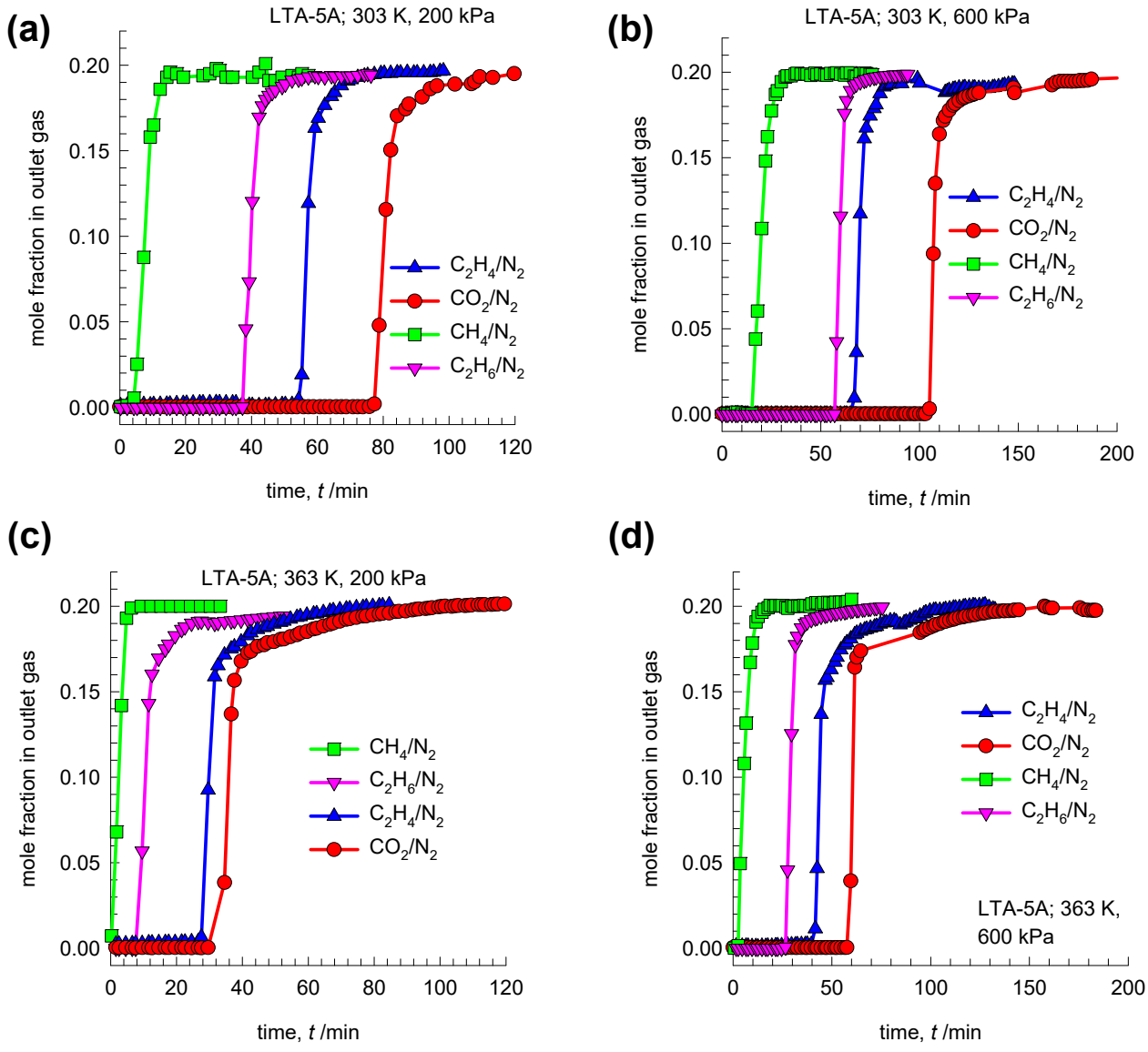

Figure S35. (a, b, c, d) Experimental data for breakthroughs of 20/80 mixtures: CH_4/N_2, C_2H_6/N_2, C_2H_4/N_2, and CO_2/N_2 mixtures in a fixed bed packed with LTA-5A zeolite operating at (a) 303 K, and p_t = 2 bar, (b) 303 K, and p_t = 6 bar, (c) 363 K, and p_t = 2 bar, and (d) 363 K, and p_t = 6 bar. The experimental data are re-drawn from the information in Figure 3 of García et al.[27]

Analysis of the experimental data of García et al.

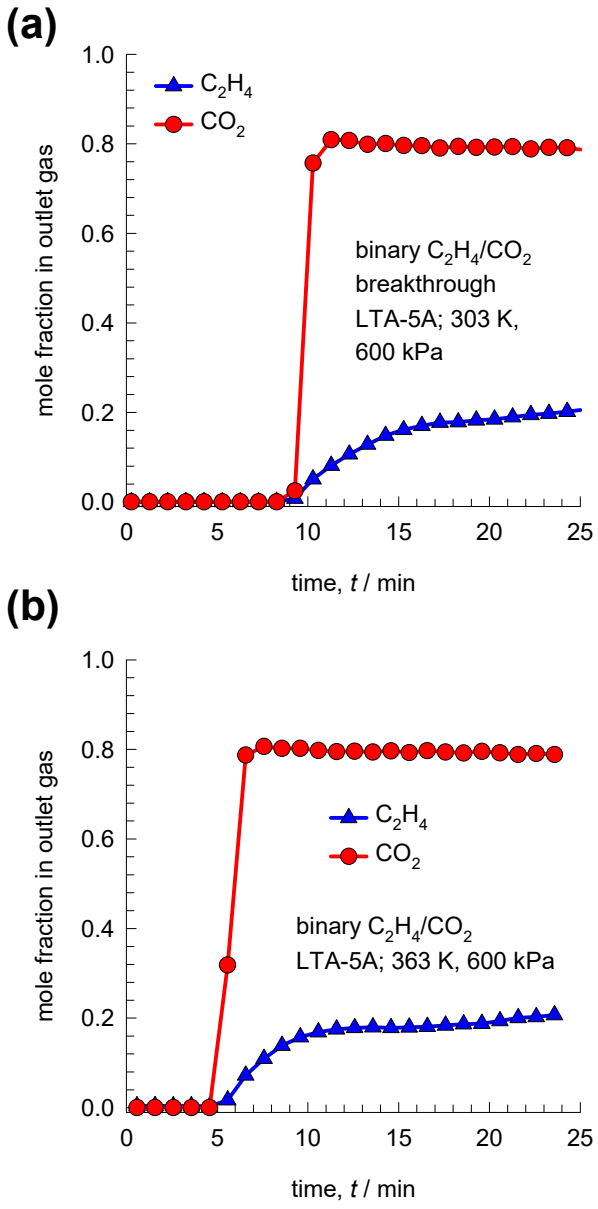

Figure S36. (a, b) Experimental data for breakthroughs of 20/80 C_2H_4/CO_2 mixtures in a fixed bed packed with LTA-5A zeolite operating at 6 bar and (a) 303 K, and (b) 363 K. The experimental data are re-drawn from the information in Figure 5 of García et al.[27]

Analysis of the experimental data of García et al.

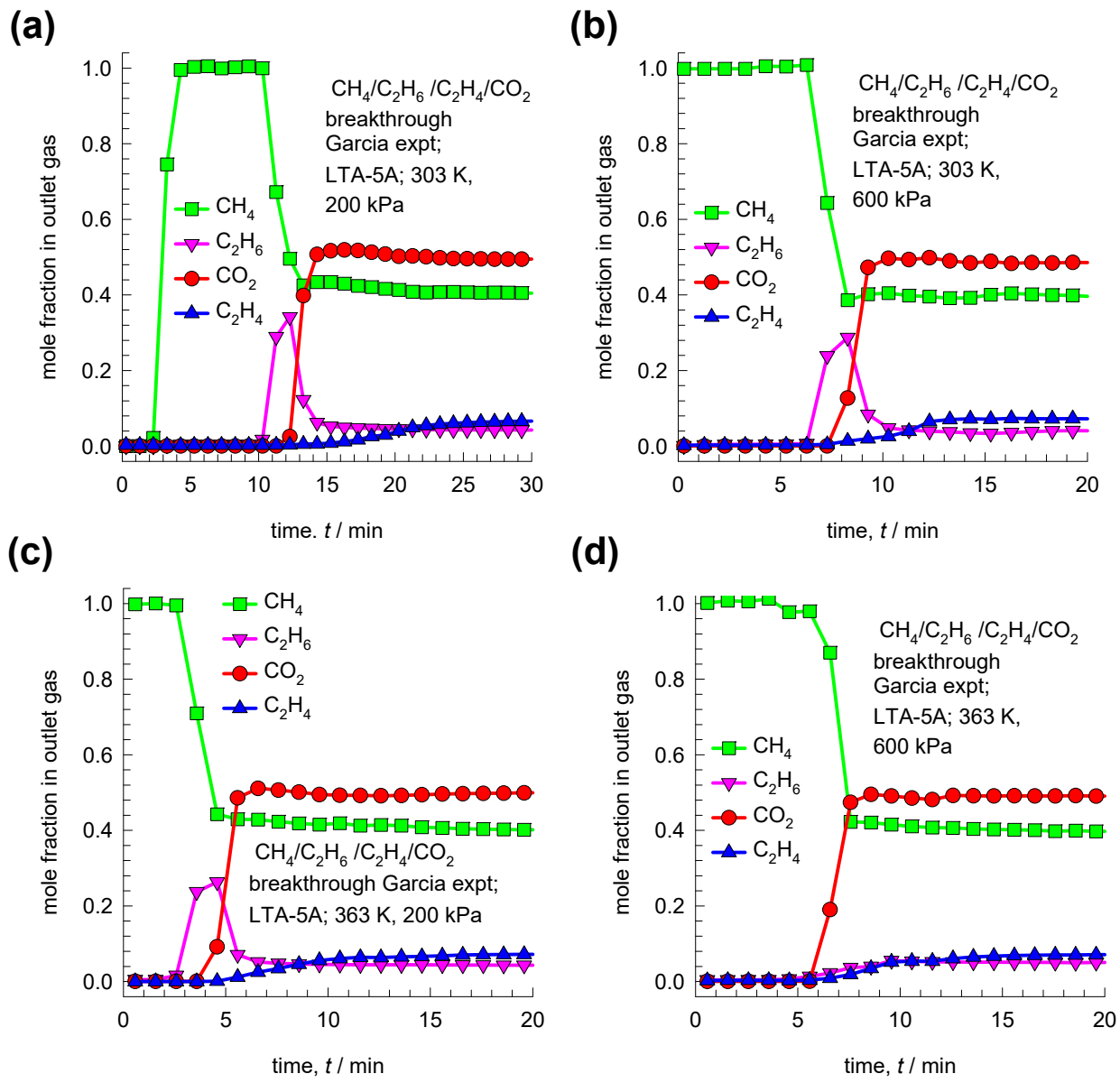

Figure S37. (a, b, c, d) Experimental data for breakthroughs of 40/4/49/7 $CH_4/C_2H_6/CO_2/C_2H_4$ mixtures in a fixed bed packed with LTA-5A zeolite operating at (a) 303 K, and p_t = 2 bar, (b) 303 K, and p_t = 6 bar, (c) 363 K, and p_t = 2 bar, and (d) 363 K, and p_t = 6 bar. The experimental data are re-drawn from the information in Figure 7 of García et al.[27] The continuous solid lines are breakthrough simulations in which the (a, b) IAST, and (c, d) RAST is used to calculate mixture adsorption equilibrium.

Analysis of the experimental data of García et al.

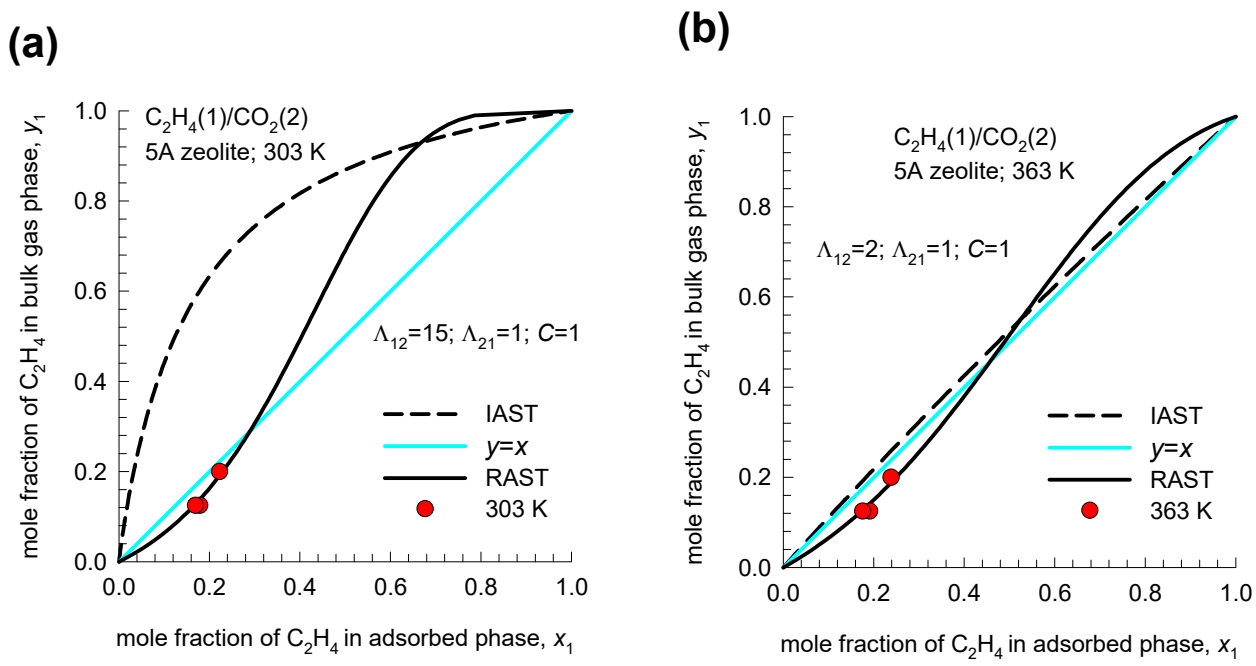

Figure S38. Experimental data for adsorption of (pseudo)-binary $C_2H_4(1)/CO_2(2)$ mixtures in LTA-5A zeolite at (a) 303 K, and (b) 363 K; the mole fraction of C_2H_4 in the bulk gas phase mixture, y_1, is plotted as a function of the adsorbed phase mole fraction of C_2H_4, x_1. The plotted data are based on the 6 experimental campaigns (3 campaigns at 303 K and 3 campaigns at 363 K) on transient experimental breakthroughs shown in Figure S36, and Figure S37, along with the use of the shock-wave model.

Analysis of the experimental data of García et al.

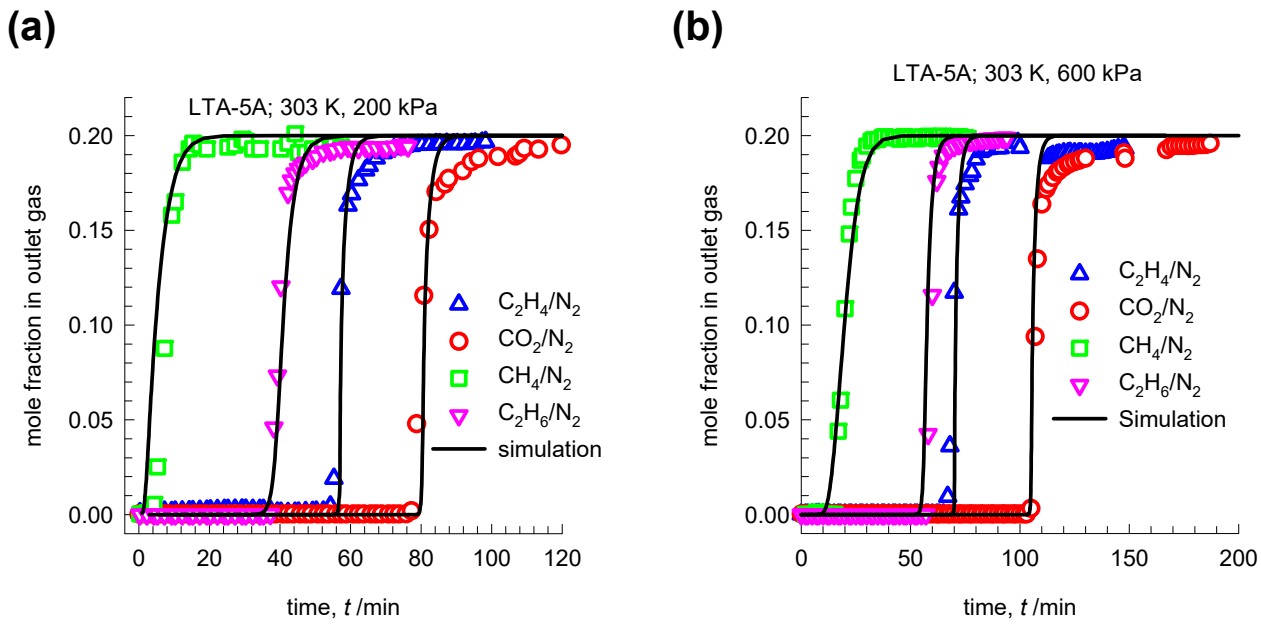

Figure S39. (a, b) Comparison of experimental data on transient breakthroughs with breakthrough simulations of 20/80 mixtures: CH_4/N_2, C_2H_6/N_2, C_2H_4/N_2, and CO_2/N_2 mixtures in a fixed bed packed with LTA-5A zeolite operating at (a) 303 K, and p_t = 2 bar, and (b) 303 K, and p_t = 6 bar. In these simulations, the IAST is used to calculate mixture adsorption equilibrium.

Analysis of the experimental data of García et al.

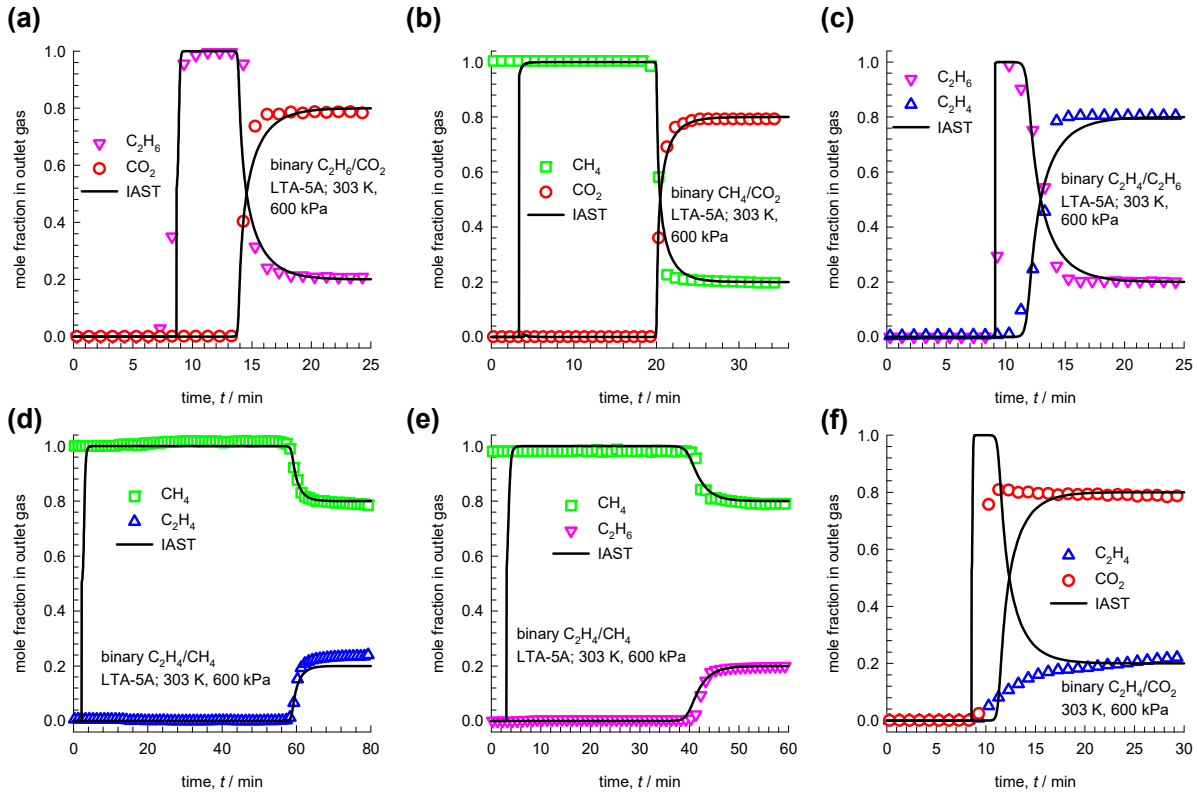

Figure S40. (a, b) Experimental data for breakthroughs of (a) 20/80 C_2H_6/CO_2, (b) 20/80 CH_4/CO_2, (c) 20/80 C_2H_6/C_2H_4, (d) 20/80 C_2H_4/CH_4, (e) 20/80 C_2H_6/CH_4, and (f) 20/80 C_2H_6/CO_2 mixtures in a fixed bed packed with LTA-5A zeolite operating at 303 K and p_t = 6 bar. The experimental data are re-drawn from the information in Figure 5 of García et al.[27] The continuous solid lines are breakthrough simulations in which the IAST is used to calculate mixture adsorption equilibrium.

Analysis of the experimental data of García et al.

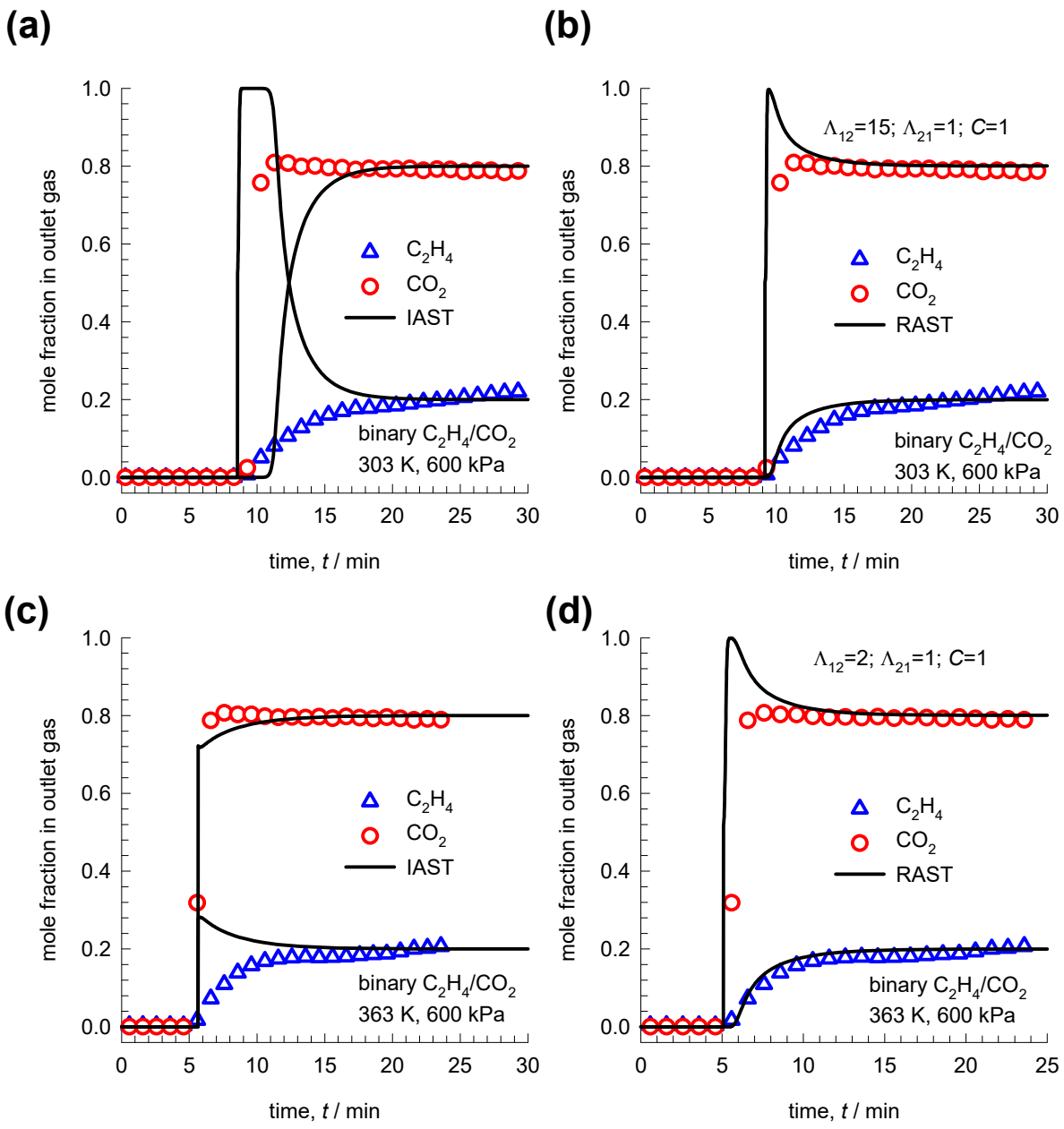

Figure S41. (a, b, c, d) Experimental data for breakthroughs of 20/80 C_2H_4/CO_2 mixtures in a fixed bed packed with LTA-5A zeolite operating at 6 bar and (a, b) 303 K, and (c, d) 363 K. The experimental data are re-drawn from the information in Figure 5 of García et al.[27] The continuous solid lines are breakthrough simulations in which the (a, c) IAST, and (b, d) RAST is used to calculate mixture adsorption equilibrium.

Analysis of the experimental data of García et al.

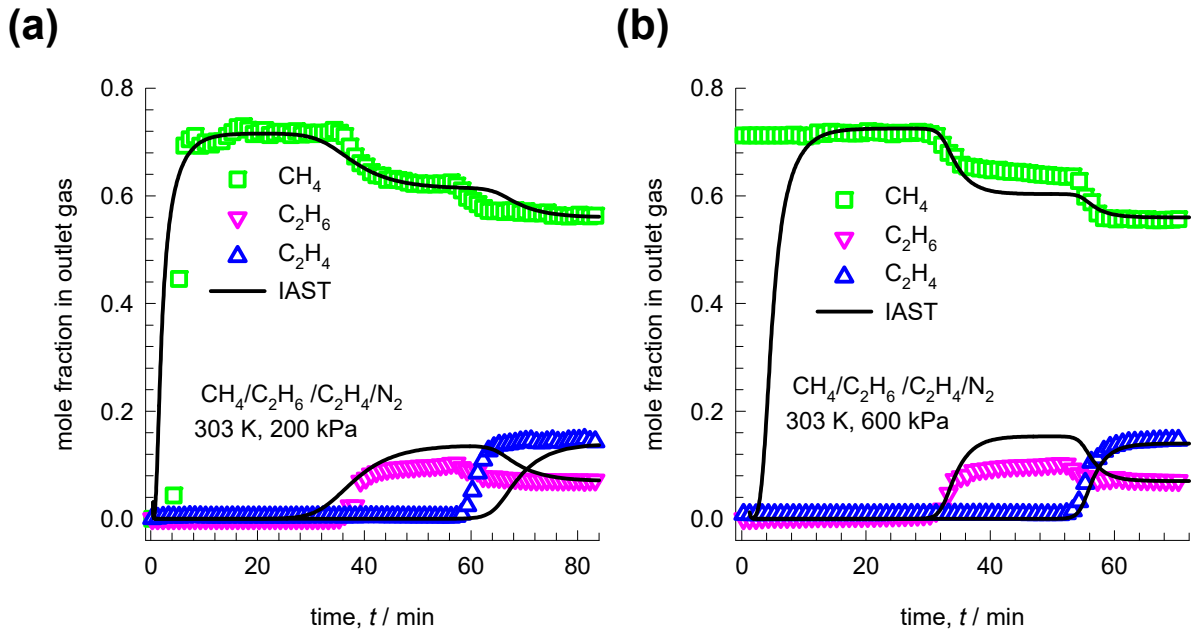

Figure S42. (a, b) Experimental data for breakthroughs of 56/7/23/14 $CH_4/C_2H_6/N_2/C_2H_4$ mixtures in a fixed bed packed with LTA-5A zeolite operating at (a) 303 K, p_t = 2 bar, and (b) 303 K, p_t = 6 bar. The experimental data are re-drawn from the information in Figure 6 of García et al.[27] The continuous solid lines are breakthrough simulations in which the IAST is used to calculate mixture adsorption equilibrium.

Analysis of the experimental data of García et al.

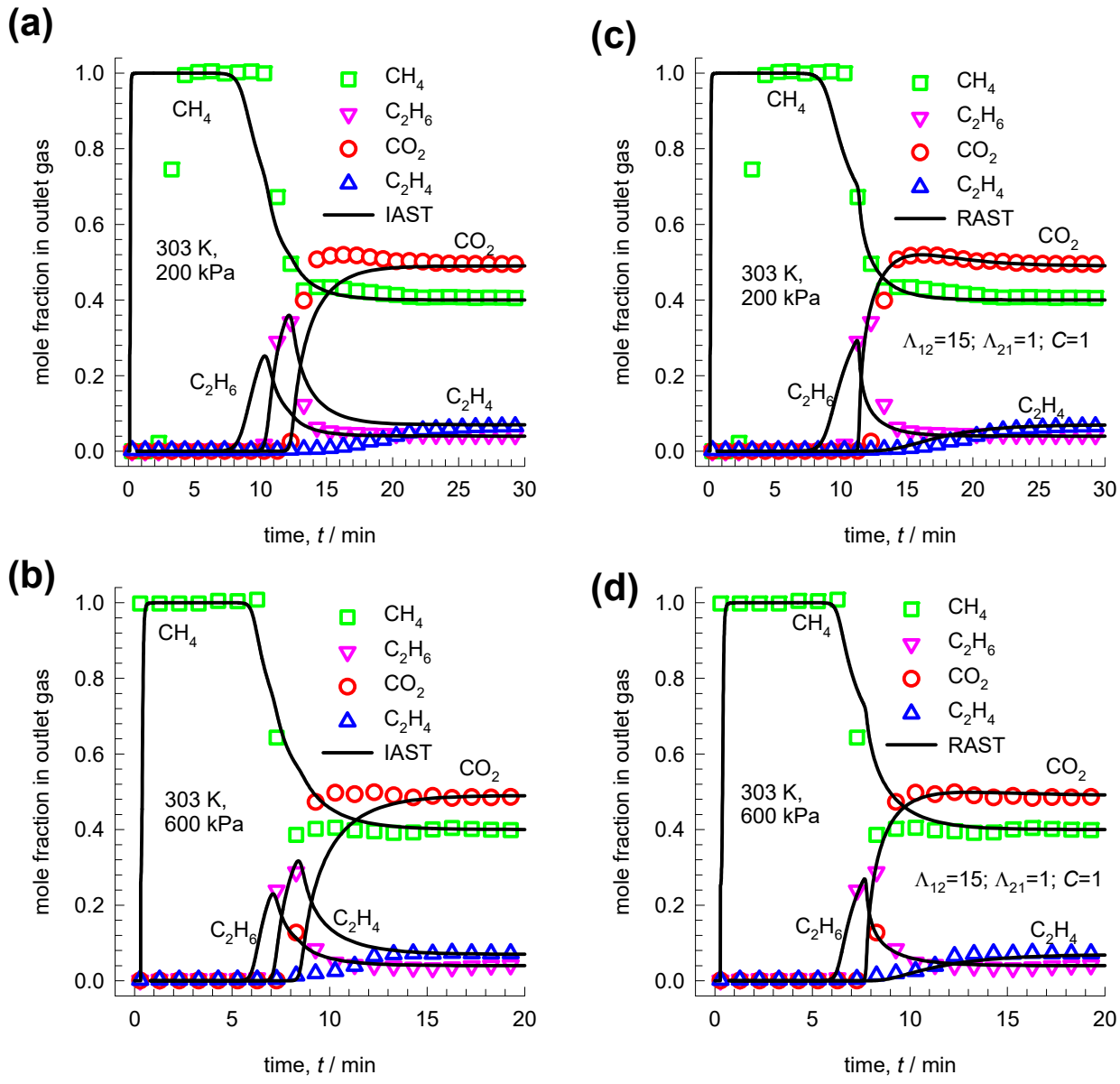

Figure S43. (a, b, c, d) Comparison of experimental breakthroughs with simulations of 40/4/49/7 $CH_4/C_2H_6/CO_2/C_2H_4$ mixtures in a fixed bed packed with LTA-5A zeolite operating at 303 K and (a, c) p_t = 2 bar, and (b, d) p_t = 6 bar. In (a, b), the IAST is used to calculate mixture adsorption equilibrium. In (c, d), the mixture adsorption equilibrium is calculated using the RAST. For the simulations of transient breakthroughs, the unary isotherm data fits are provided in Table S1, Table S2, Table S3, and Table S4.

Analysis of the experimental data of García et al.

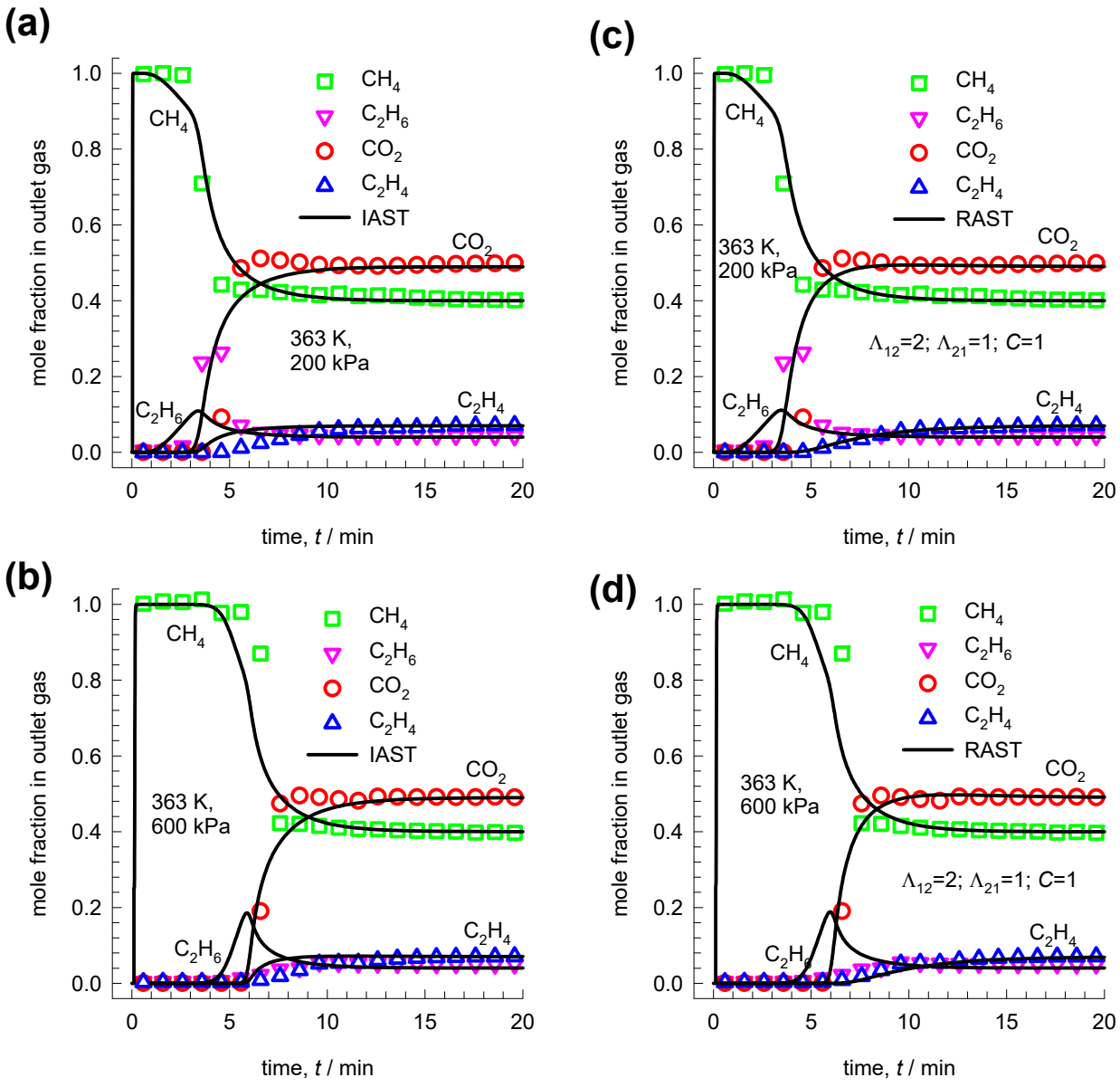

Figure S44. (a, b, c, d) Comparison of experimental breakthroughs with simulations of 40/4/49/7 $CH_4/C_2H_6/CO_2/C_2H_4$ mixtures in a fixed bed packed with LTA-5A zeolite operating at 363 K and (a, c) p_t = 2 bar, and (b, d) p_t = 6 bar. In (a, b), the IAST is used to calculate mixture adsorption equilibrium. In (c, d), the mixture adsorption equilibrium is calculated using the RAST. For the simulations of transient breakthroughs, the unary isotherm data fits are provided in Table S1, Table S2, Table S3, and Table S4.

10 Nomenclature

Latin alphabet

A	surface area per kg of framework, $m^2\ kg^{-1}$
b_i	Langmuir parameter, Pa^{-1}
c_i	molar concentration of species *i*, mol m^{-3}
c_t	total molar concentration in mixture, mol m^{-3}
c_{i0}	molar concentration of species *i* in fluid mixture at inlet to adsorber, mol m^{-3}
C	constant used in Equation (S13), kg mol^{-1}
$Đ_i$	M-S diffusivity of component *i* for molecule-pore interactions, $m^2\ s^{-1}$
E	energy parameter, J mol^{-1}
L	length of packed bed adsorber, m
n	number of species in the mixture, dimensionless
p_i	partial pressure of species *i*, Pa
p_t	total system pressure, Pa
P_i^0	sorption pressure, Pa
q_A	molar loading species A, mol kg^{-1}
$q_{i,sat}$	molar loading of species *i* at saturation, mol kg^{-1}
q_t	total molar loading of mixture, mol kg^{-1}
r	radial coordinate, m
r_c	radius of crystallite, m
R	gas constant, 8.314 J $mol^{-1}\ K^{-1}$
S_{ads}	adsorption selectivity, dimensionless
t	time, s
T	absolute temperature, K
u	superficial gas velocity in packed bed, m s^{-1}

Nomenclature

v	interstitial gas velocity in packed bed, m s^{-1}
V_p	pore volume, m^3 kg^{-1}
x_i	mole fraction of species *i* in adsorbed phase, dimensionless
y_i	mole fraction of species *i* in bulk fluid mixture, dimensionless
z	distance along the adsorber, and along membrane layer, m

Greek letters

γ_i	activity coefficient of component *i* in adsorbed phase, dimensionless
ε	voidage of packed bed, dimensionless
Λ_{ij}	Wilson parameters, dimensionless
μ_i	molar chemical potential, J mol^{-1}
π	spreading pressure, N m^{-1}
ρ	framework density, kg m^{-3}
τ	time, dimensionless

Subscripts

i,j	components in mixture
i	referring to component *i*
t	referring to total mixture
sat	referring to saturation conditions

Superscripts

0	referring to pure component loading

Nomenclature

excess referring to excess parameter

11 References

(1) Baerlocher, C.; Meier, W. M.; Olson, D. H. *Atlas of Zeolite Framework Types*. 5th Edition, Elsevier: Amsterdam, 2002.

(2) Baerlocher, C.; McCusker, L. B. Database of Zeolite Structures. http://www.iza-structure.org/databases/, International Zeolite Association, 10 January 2002.

(3) Ruthven, D. M. *Principles of Adsorption and Adsorption Processes*. John Wiley: New York, 1984.

(4) Myers, A. L.; Prausnitz, J. M. Thermodynamics of Mixed Gas Adsorption. *A.I.Ch.E.J.* **1965**, *11*, 121-130.

(5) Siperstein, F. R.; Myers, A. L. Mixed-Gas Adsorption. *A.I.Ch.E.J.* **2001**, *47*, 1141-1159.

(6) Talu, O.; Myers, A. L. Rigorous Thermodynamic Treatment of Gas-Adsorption. *A.I.Ch.E.J.* **1988**, *34*, 1887-1893.

(7) Talu, O.; Zwiebel, I. Multicomponent Adsorption Equilibria of Nonideal Mixtures. *A.I.Ch.E.J.* **1986**, *32*, 1263-1276.

(8) Krishna, R. The Maxwell-Stefan Description of Mixture Diffusion in Nanoporous Crystalline Materials. *Microporous Mesoporous Mater.* **2014**, *185*, 30-50.

(9) Krishna, R. Methodologies for Evaluation of Metal-Organic Frameworks in Separation Applications. *RSC Adv.* **2015**, *5*, 52269-52295.

(10) Krishna, R. Screening Metal-Organic Frameworks for Mixture Separations in Fixed-Bed Adsorbers using a Combined Selectivity/Capacity Metric. *RSC Adv.* **2017**, *7*, 35724-35737. https://doi.org/10.1039/C7RA07363A.

(11) Krishna, R. Methodologies for Screening and Selection of Crystalline Microporous Materials in Mixture Separations. *Sep. Purif. Technol.* **2018**, *194*, 281-300. https://doi.org/10.1016/j.seppur.2017.11.056.

(12) Krishna, R.; Baur, R. Modelling Issues in Zeolite Based Separation Processes. *Sep. Purif. Technol.* **2003**, *33*, 213-254.

(13) Kooijman, H. A.; Taylor, R. A dynamic nonequilibrium model of tray distillation columns. *A.I.Ch.E.J.* **1995**, *41*, 1852-1863.

(14) Michelsen, M. An efficient general purpose method of integration of stiff ordinary differential equations. *A.I.Ch.E.J.* **1976**, *22*, 594-597.

(15) Bulirsch, R.; Stoer, J. Numerical treatment of ordinary differential equations by extrapolation methods. *Numer. Math.* **1966**, *8*, 1-14.

(16) Krishna, R.; Baur, R. Diffusion, Adsorption and Reaction in Zeolites: Modelling and Numerical Issues. http://krishna.amsterchem.com/zeolite/, University of Amsterdam, Amsterdam, 1 January 2015.

(17) Krishna, R.; van Baten, J. M. Investigating the potential of MgMOF-74 membranes for CO_2 capture. *J. Membr. Sci.* **2011**, *377*, 249-260.

(18) He, Y.; Krishna, R.; Chen, B. Metal-Organic Frameworks with Potential for Energy-Efficient Adsorptive Separation of Light Hydrocarbons. *Energy Environ. Sci.* **2012**, *5*, 9107-9120.

(19) Mofarahi, M.; Salehi, S. M. Pure and Binary Adsorption Isotherms of Ethylene and Ethane on Zeolite 5A. *Adsorption* **2013**, *19*, 101-110.

References

(20) Mofarahi, M.; Gholipour, F. Gas Adsorption Separation of CO_2/CH_4 System using Zeolite 5A. *Microporous Mesoporous Mater.* **2014**, *200*, 47-54.

(21) Bakhtyari, A.; Mofarahi, M. Pure and Binary Adsorption Equilibria of Methane and Nitrogen on Zeolite 5A. *J. Chem. Eng. Data* **2014**, *59*, 626-639.

(22) Jamali, S.; Mofarahi, M.; Rodrigues, A. E. Investigation of a novel combination of adsorbents for hydrogen purification using Cu-BTC and conventional adsorbents in pressure swing adsorption. *Adsorption* **2018**, *24*, 481-498. https://doi.org/10.1007/s10450-018-9955-0.

(23) van Zandvoort, I.; van Klink, G. P. M.; de Jong, E.; van der Waal, J. C. Selectivity and Stability of Zeolites [Ca]A and [Ag]A towards Ethylene Adsorption and Desorption from Complex Gas Mixtures. *Microporous Mesoporous Mat.* **2018**, *263*, 142-149.

(24) Krishna, R.; van Baten, J. M.; Baur, R. Highlighting the Origins and Consequences of Thermodynamic Nonidealities in Mixture Separations using Zeolites and Metal-Organic Frameworks. *Microporous Mesoporous Mater.* **2018**, *267*, 274-292. http://dx.doi.org/10.1016/j.micromeso.2018.03.013.

(25) Krishna, R.; Van Baten, J. M. Investigating the Non-idealities in Adsorption of CO_2-bearing Mixtures in Cation-exchanged Zeolites. *Sep. Purif. Technol.* **2018**, *206*, 208-217. https://doi.org/10.1016/j.seppur.2018.06.009.

(26) Calleja G.; Pau J.; Perez P.; J.A., C. *Binary and Ternary Adsorption Equilibria at High Pressure on Molecular Sieves*. Fundamentls of Adsorption FOA 1996; Edited by L. M.D., The Kluwer International Series in Engineering and Computer Science: Boston, Massachusetts, 1996.(https://doi.org/10.1007/978-1-4613-1375-5_17)

(27) García, L.; Poveda, Y. A.; Rodríguez, G.; Esche, E.; Godini, H. R.; Wozny, G.; Repke, J.-U.; Orjuela, A. Adsorption Separation of Oxidative Coupling of Methane Effluent Gases. Miniplant Scale Experiments and Modeling. *J. Nat. Gas Sci. Eng.* **2019**, *61*, 106-118. https://doi.org/10.1016/j.jngse.2018.11.007.